

Contents

1	Introduction	1
2	Electric-field noise in ion traps	3
2.1	Surface electric-field noise	3
2.2	Trapped ions	4
2.3	Quantum information processing	4
2.4	Current progress	5
3	Micro-fabricated surface trap	7
3.1	RF quadrupole traps	7
3.2	Chip design	9
3.3	Fabrication process	11
3.4	Properties of the trap surface	13
4	Noise measurement methods	15
4.1	Optical control of calcium ions	15
4.2	Ion heating rate measurements	17
4.3	Calculation of electric-field noise	20
4.4	Frequency scaling of ion heating rates	21
4.5	Experimental setup	22
5	Surface treatment & characterization techniques	26
5.1	Trap substrate heating	27
5.2	Auger spectroscopy & electron bombardment	30
5.3	Argon ion milling	36
5.4	Ion-trapping side effects	37
6	Thermally activated fluctuators	38
6.1	Mathematical framework	38
6.2	Fit to ion-heating-rate data	40
6.3	The physical embodiment of TAFs	44
6.4	Summary	45
7	Timeline of data and surface treatments	46

8 Heating rates in different aluminum-copper traps	64
8.1 Background on 4 Al/Cu traps	64
8.2 Linking fabrication process variations & heating-rate magnitudes	65
8.3 Material removal & heating-rate reductions	68
8.4 Summary	72
9 Heat treatment experiments	74
9.1 Thermal transformation of noise sources	74
9.2 Intermittent transformations	77
9.3 Investigation of contaminant deposition	80
9.4 Investigation of chemical changes	82
9.5 Investigation of atomic restructuring	84
9.5.1 Recrystallization temperatures	84
9.5.2 Morphological changes: annealing	85
9.5.3 Morphological changes: milling	87
9.5.4 Correlated and uncorrelated noise sources	89
9.5.5 TAF distributions and surface binding energies	90
9.5.6 Ex-situ surface treatment and characterization experiments	91
9.6 Summary	95
10 Electron bombardment experiments	97
10.1 Overview of experimental results	97
10.1.1 Treatment parameters	98
10.1.2 Substrate properties	99
10.1.3 Heating rate measurements	102
10.2 Materials interacting with energetic electrons	104
10.2.1 Conductors	104
10.2.2 Insulators	104
10.2.3 Organic contaminants	105
10.2.4 Electron beam induced deposition	106
10.3 The underlying physics of five electron treatments	106
10.3.1 Electron 1	107
10.3.2 Electron 2	108
10.3.3 Electron 3	111
10.3.4 Electron 4	112
10.3.5 Electron 5	113
10.4 Summary and plans for future work	114
11 High-temperature shoot off	116
12 Conclusion	117
Bibliography	118

Chapter 1

Introduction

All surfaces generate electric-field noise, and yet the physical origins of this noise are not well understood. This has been an active area of research in the ion-trapping community for the past two decades, as ions are highly sensitive to electric-field fluctuations. A trapped atomic ion can operate as an ultra-sensitive narrow-band electric-field-noise detector. Because of these detection capabilities, a trapped ion is a powerful tool in the study of microscopic surface charge dynamics. An understanding of these dynamics would enable the engineering of ultra-low-noise ion trap chips, which would enhance the ability of trapped ions to serve as vehicles for quantum information processing and tests of fundamental physics.

We aim to illuminate the physics of these dynamic processes by observing how the electric-field noise from a metal surface changes in response to surface treatments. The data-taking stage of this project began in 2017, when we took the first-ever measurements of electric-field noise in a  ion trap. After completing these initial measurements, we planned an experiment that involved a series of small-dose surface sputter treatments, interspersed with Auger spectroscopy and noise measurements at multiple temperatures and frequencies.

What was expected to be a simple, month-long experiment became a highly-involved project that continued over a period of almost two years. First, we observed that the electron beam from the Auger spectrometer  have a significant impact on surface noise, and must be considered as a surface treatment in its own right. When we began the sputter treatments, the noise in this trap responded differently to sputtering than similarly-fabricated traps had in the past. Our first round of noise measurements in a hot trap were stable and repeatable, but after a few rounds of sputtering, the heat began to induce persistence changes in the surface noise magnitude.

Piecing together our complicated array of measurement results, and the vast literature on surface treatments performed in different contexts, we have been able to uncover many new insights about the noise in our trap. This project was highly exploratory, and leaves many questions unanswered, but can provide a strong jumping-off point for future experiments in ion trap surface science.

This dissertation is organized as follows. In Chapter 2, we provide an overview of previous experimental and theoretical studies of ion-trap surface noise. In Chapter 3, we present the details of our ion trap. Details include the principles of its operation as an electronic device, the fabrication process through which it was made, and the physical properties of the metal film that coats its surface. In Chapter 4, we introduce standard optical control methods

for calcium ions, and explain how we use these methods to measure the power-spectral-density of the electric-field noise at the ion. In Chapter 5 we introduce our other surface characterization and treatment tools, including Auger spectroscopy, trap heating, and argon ion milling.

In Chapter 6, we introduce the thermally-activated-fluctuator model, and do a meta-analysis of all of our data in the context of this model. In Chapter 7, we show a timeline of all of the noise measurements, Auger spectra and surface treatments that took place during this experiment. This timeline establishes a naming convention so that datasets can be referred to consistently throughout the remaining chapters of this dissertation. In Chapter 8, we compare the noise measured in our trap to noise in other similarly fabricated ion traps, both treated and untreated. In Chapter 9, we discuss how surface roughness affects electric-field noise, and we present data from milling, heating and select electron-bombardment experiments. In Chapter 10 we focus exclusively on electron-bombardment experiments, and explore how these experiments can inform our understanding of how carbon compounds generate electric-field noise. Finally, in Chapter 11, we discuss the phenomenon in which the noise magnitude shoots up around 600 K, and speculate about possible underlying causes.

Chapter 2

Electric-field noise in ion traps

2.1 Surface electric-field noise

Surface electric-field noise is the fluctuation of an electric field due to charge movement at the surface of a material. Noise from metal surfaces is of particular interest to the ion trapping community, as these surfaces play a key role in trapped-ion quantum information processing. While it is generally understood that dynamic processes such as defect hopping and contaminant diffusion take place at metal surfaces, it is not known which microscopic processes specifically dominate charge dynamics.

Measurements of electric-field noise in ion traps have varied widely between different ~~traps~~ and different traps [1], including variations in noise magnitudes, frequency and distance dependencies, and treatment responses. This is an indication that no single process is responsible for all surface noise. Most likely, in any given system there are multiple competing mechanisms at play. To understand electric-field noise from metal surfaces in general, we must first disentangle these mechanisms through in-depth studies of individual surfaces.

In order to investigate the underlying microscopic processes that take place in our specific physical system, an Al/Cu surface ion trap, we combine electric-field noise measurements with surface treatments. Electric-field noise is characterized by its power spectral density, which can be measured with great precision using a trapped ion as a detector. As the physical properties of the surface change in response to treatments, the power spectral density of the electric-field noise changes as well. By alternating between different types of surface treatments, while tracking the state of the surface and its electric-field noise, we can begin to pin down properties of the underlying noise sources.

The advancement ~~of~~ our understanding of surface charge dynamics would open new avenues for ion trap engineering. It could also benefit other technologies which suffer from surface noise of various kinds, both inside and outside of the field of quantum information processing. Charge states are tied to crystal lattice configurations, chemical bond structures, and likely other phenomena of interest to scientists and engineers in a diverse range of disciplines. As a result, the development of trapped ions as a tool to investigate surface charge dynamics could have far reaching applications.

2.2 Trapped ions

A trapped ion is a single charged particle, levitated in vacuum by an electromagnetic field. For the purpose of measuring electric-field noise, the ideal ion has a simple energy structure with transitions that are accessible with existing laser technologies. Lasers can then be used to initialize, control, and read out the electronic state of the ion. We will describe the control scheme that we use for our $^{40}\text{Ca}^+$ ions in Section 4.1.

In order to measure the power spectral density of the electric-field noise, the ion must be held in a harmonic potential. In our system, we use a RF quadrupole trapping configuration, the details of which will be discussed in Section 3.1. The harmonic potential has evenly spaced vibrational energy levels with a transition energy of $\hbar\omega$. Electric-field noise at frequency ω drives transitions between these vibrational energy levels, thus causing the ion to heat up.

When the ion heats up, the control lasers become Doppler shifted with respect to the electronic transitions in the ion. This changes the speed at which a laser pulse can alter the electronic state. As a result, after a laser pulse, the electronic state of the ion depends on its motional state. The laser has coupled these energy systems together. Having already developed the tools to initialize and read out electronic states, it is now possible to deduce the vibrational energy of the trapped ion. To measure the power spectral density of the electric-field noise, one may simply measure how quickly the vibrational energy of an ion changes in the presence of an electric field. Section 4.2 will describe these measurements and calculations in more detail.

2.3 Quantum information processing

Trapped ions have proven to be a promising architecture for quantum information processing [2]. Every ion of the same species is exactly identical, and electronic states of select species can be reduced to simple two-level systems. Levitated ions are well isolated, and can safely store qubit information for extended periods of time. Ion qubits can be initialized and read out optically. In addition, high-fidelity single-qubit gates and multi-qubit entangling gates can be performed using simple laser pulse sequences.

Quantum computers are designed to take advantage of the computational power of entangled superpositions. These superpositions can contain massive amounts of information. Through carefully engineered constructive and destructive interference, some superpositions can be distilled down to reveal simple solutions to complex problems. Some interesting problems that are intractable in classical computing are thought to be solvable with a quantum computer.

Long-term quantum-computing goals include breaking classical encryption schemes and simulating chemical reactions, but these milestones require quantum computers far more powerful than those in existence today. The first useful application of a quantum information processor will likely be a quantum emulation. Even simple quantum systems are difficult to simulate classically, but could be emulated and studied with a small-scale quantum processor. In order to build such a processor, many engineering challenges must be overcome, including the mitigation of surface electric-field noise.

Electric-field noise lowers the fidelity of both single- and multi-qubit gates. Gates depend on laser pulses with precise frequencies and stable amplitudes. Uncontrolled ion vibrations can introduce frequency instability via Doppler shifts, and amplitude instability via the movement of the ion away from the center of focused laser beams. Multi-ion gates are particularly sensitive to electric-field noise, as these gates require ultra-stable motional states. Coulomb interactions between ions in a chain cause the ions to share motional modes. In a multi-ion gate operation, the motional modes of the chain are used as a bus to entangle together the electronic states of different ions. If electric-field noise drives a change in the motional state of the chain during a multi-qubit operation, the operation will fail.

The fidelity of a two-qubit entangling gate performed in a standard 3D ion trap is not typically limited by surface electric-field noise [3]. However, the engineering required to scale up this system into a useful quantum processor amplifies electric-field-noise-induced motional heating. A useful ion-based processor must contain many ions, yet the heating rate of the center-of-mass vibrational mode of a chain scales linearly with its ion number. The processor must be capable of quickly shuttling ions between different chains, but shuttling requires the ions to be close to the surface of the electrodes. The closer an ion gets to the noisy metal surface, the higher the noise at the ion becomes. In addition to enabling shuttling, moving the ion close to the electrode makes it possible to raise the ion trap frequency without raising the electrode voltage, thus lowering the time required for entangling gates. Furthermore, traps with small ion-electrode distances can be microfabricated, enabling complex electrode configurations that would not otherwise have been possible to build.

2.4 Current progress

Many ion-trapping projects could benefit greatly from the successful mitigation of surface electric-field noise. For this reason, over the past two decades, a significant effort has been put towards studying electric-field noise in ion traps. In early literature on this subject, these efforts were referred to as the study of *anomalous heating*, as it was not known where the noise was coming from.

Electric-field-noise power spectral densities ranging from 10^{-16} to $10^{-6} \text{ V}^2/\text{m}^2\text{Hz}$ have been measured by trapped ions. Over the course of many different experiments, noise has been studied at frequencies between 0.1 and 20 MHz, at ion-surface distances between 30 and 3500 μm , and at temperatures between 4 and 600 K [1, 4].

Frequency-scaling measurements taken in many different ion traps show that surface noise scales as $1/f^\alpha$, where f is the noise measurement frequency. Measurements of α cluster around 1 and 1.5 [1]. Noise has been found to scale as $1/d^\beta$, where d is the ion-electrode distance. β has been measured to be 2.4 and 4 in different systems [5, 6]. Temperature-scaling measurements have revealed a variety of different scaling behaviors, but in most cases noise decreases as the substrate temperature is lowered, and increases as the substrate temperature is raised, indicating that the dominant noise sources are heat activated [7, 8, 4]. A study comparing traps with different species of untreated metal films found no significant correlations between noise levels and electrode materials [8].

Several different types of surface treatments have been done in ion traps in conjunction with electric-field-noise measurements. UV light exposure reduced electric-field noise by

about 50% in one ion trap [10]. Argon ion milling reduced noise by up to two orders of magnitude [11, 12] and oxygen plasma reduced noise by a factor of four [13]. In all cases, these treatments removed contamination from the surface of the trap. These results indicate that surface contaminants play a key role in generating electric-field noise in ion traps.

However, the relationship between contamination and electric-field noise is not straightforward. Daniilidis et. al. found that a trap recontaminated after milling maintained a low noise magnitude [11]. Sedlacek et. al. observed that for some materials, ion milling actually increased noise at cryogenic temperatures, and Sedlacek et. al. found that noise first rose and then fell in response to a series of small-dose ion milling treatments [14]. This dissertation presents additional surface treatment experiments. We combine electron bombardment, heat treatment and argon ion milling in a single trap to further investigate the complexities of electric-field noise generated by contaminants.

The data gathered through measurements of electric-field noise in ion traps can be used to inform models of the underlying noise processes. In surface noise experiments, a serious effort is made to remove electromagnetic pickup and technical noise from trapping electronics, so these mechanisms can be set aside. Metals are known to produce black-body radiation and Johnson-Nyquist noise. These sources have been carefully considered and ruled out, as their magnitudes are far too low to explain the observed noise [1].

Some promising physical models include fluctuating adsorbate dipoles [15], adsorbate diffusion on surfaces [16], and noise from a surface dielectric layer [17]. No single model has been able to fully explain the experimental data described above, but all are able to describe an interesting subsection of the observed noise behaviors and characteristics. Additional discussion of noise models can be found in the surface noise review by M. Brownnutt et. al. [1]. We have found that measurements taken in our Al/Cu ion trap are consistent with the thermally activated fluctuator (TAF) model. This model does not fully establish predict the properties of the underlying noise sources, but it establishes a simple framework to describe their dynamics. A discussion of this model and its applicability to our data will be presented in Chapter 6.

In summary, the noise measurements taken in ion traps reveal a jumbled and confusing landscape of information. None of the models developed to explain them have done much to demystify the situation. We believe that our exploratory surface treatment work provides a clear and consistent overview of noise in one trap, which can pave the way for more concrete studies of surface noise.

Consider moving some of the comments specific to our experiments out to the introduction

Chapter 3

Micro-fabricated surface trap

The ultimate goal of our work is to understand the microscopic processes that generate electric-field noise on metal surfaces. To this end, we perform a variety of surface treatments on a single ion trap substrate, and use trapped ions to measure changes in the surface electric-field noise. In these experiments, the metal film on the surface of the ion trap is the subject of our scientific inquiry, and it is also a critical component of an actively-operating electronic device. In this chapter we will explain how this device (the quadrupole ion trap) works, present the design of our trap, describe our microfabrication processes, and show some ~~preliminary~~ surface characterization measurements.



3.1 RF quadrupole traps

The RF quadrupole ion trap, also known as the Paul trap, is a well-established tool in experimental atomic physics. It is designed to trap charged particles at the null point of an electric field. The field is generated by a set of electrodes carrying DC and RF voltages.

To create a stable trapping point, the electric field at that point must be zero, and the field must exert a restoring force if the trapped particle (the ion) is displaced in any direction. A positive ion will encounter a restoring force along a given axis if the second derivative of the electric potential is negative along that axis. If the second derivative is positive, then a slight displacement will cause the ion to be ejected away from the null point instead of restored back. It is impossible to create a stable 3D trapping point with static electric fields, as electric potentials must obey the Laplace equation. The Laplace equation states:

$$\Delta^2 V = \frac{\partial^2 V}{\partial x_1^2} + \frac{\partial^2 V}{\partial x_2^2} + \frac{\partial^2 V}{\partial x_3^2} = 0, \quad (3.1)$$

where V is the electric potential and x_1 , x_2 and x_3 are orthogonal spatial dimensions. It follows that if there is a restoring force along any axis, then a different axis must have an ejecting force so that the second derivatives of the potentials sum to zero.

Remarkably, it is possible to create a stable, 3D restoring force using oscillating electric fields. Electrodes in Paul traps are designed to produce a saddle potential. A two-dimensional saddle potential is shown in Figure 3.1a. In this image, red and blue coloring correspond to areas with high and low potential respectively. A saddle potential provides a

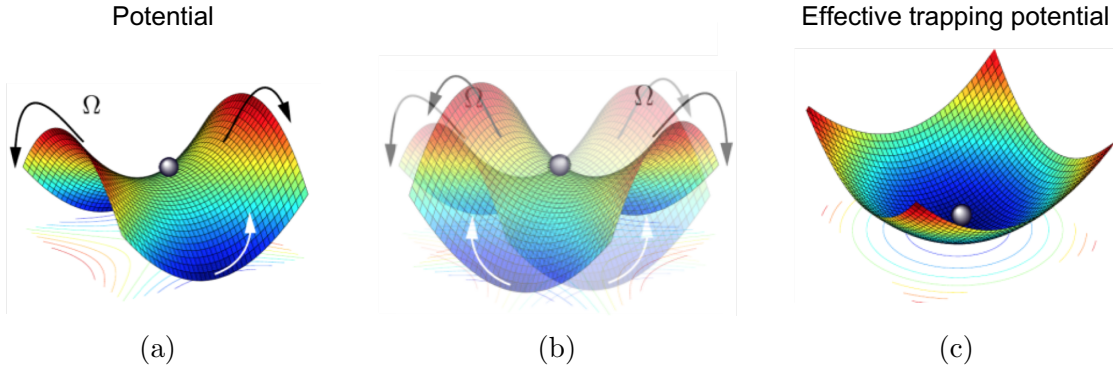


Figure 3.1: Illustration of RF trapping mechanism, adapted from [18]. (a) 2D saddle potential, where red and blue coloring correspond to areas with high and low potential respectively. (b) Saddle oscillating between two configurations. (c) Effective trapping potential, achieved when trapping parameters meet conditions for stability.

orative force along one axis, and ejecting force along the other, thus obeying the Laplace equation.

In Figure 3.1b, the saddle oscillates at frequency Ω , while keeping constant the potential at the position of the ion. This can be implemented in an ion trap by applying an oscillating voltage to some of the electrodes. The motion of an ion in an oscillating saddle potential can be derived from the Mathieu equation.

If the electrode geometry, voltages, and RF drive frequency Ω are precisely tuned to the mass and charge of the ion, the oscillating saddle generate an effective trapping potential, as illustrated in Figure 3.1c. For a discussion of the Mathieu equation in the context of ion trapping, including how to determine stable trapping parameters for a given ion, see reference [19].

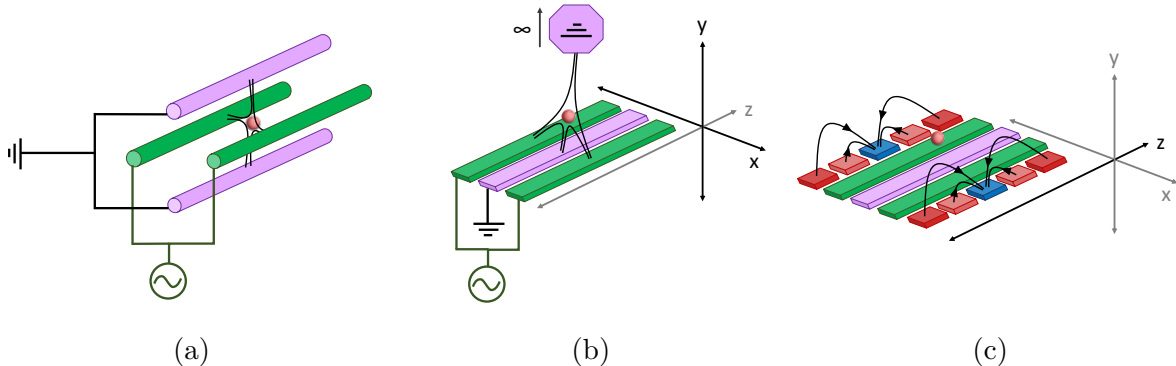


Figure 3.2: a) Cartoon of a simple 3D RF quadrupole Paul trap. (b) Microfabricated surface trap with RF-generated radial confinement. (c) Microfabricated surface trap with DC-generated axial confinement.

A cartoon of a simple 3D RF quadrupole Paul trap is shown in Figure 3.2a. This trap has four poles, two of which are grounded, and two of which oscillate between positive and

negative voltages at a frequency of Ω . An ion is trapped between the poles. Typically, a 3D Paul trap also has DC end-cap electrodes to provide confinement along the z-axis.

The first RF Paul trap was built in 1954 [20] by Wolfgang Paul. In 2005, Chiaverini et. al. developed the microfabricated surface trap [21]. This trap was designed to be a modular component of a large-scale trapped-ion quantum information processor. As illustrated in Figure 3.2b, the surface trap is ~~simply~~ a 3D trap in which the poles have been rearranged. In a surface trap, two oscillating and one grounded electrode are fabricated on a flat plane. The grounded vacuum chamber serves as the fourth electrode, and the ion is trapped above the microfabricated center electrode. Typically the distance between the ion and the nearest electrode surface is smaller in a surface trap than in a 3D trap.

The electrodes illustrated in Figure 3.2b provide confinement along the x- and y-axes, commonly referred to as the radial directions. In a surface trap, additional planar DC electrodes generate confinement along the z-axis, which is commonly referred to as the axial direction. Axial confinement electrodes are illustrated in Figure 3.2b. For more information on the principles of RF and DC confinement in surface traps, refer to L^uch masters thesis [18].

3.2 Chip design

Having outlined the basic operating principles of surface RF quadrupole traps, we will now present the specific details of our trap design. Figure 3.3 shows a top view of the ion trap chip, with DC and RF electrodes highlighted. In this design, the RF electrodes are connected together. The RF electrodes are driven at frequency $\Omega = 36$ MHz, with a peak-to-peak amplitude of about 100 V.

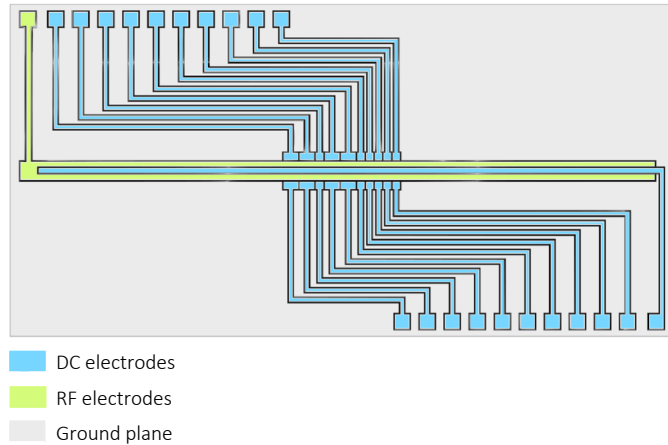


Figure 3.3: Electrode design of TRAP C.

As shown in Figure 3.4, the electrodes are designed so that ions can be trapped within a central trapping region. Electrical connections between the trap electrodes and the control electronics are made via wirebonds at the outer edges of the chip.

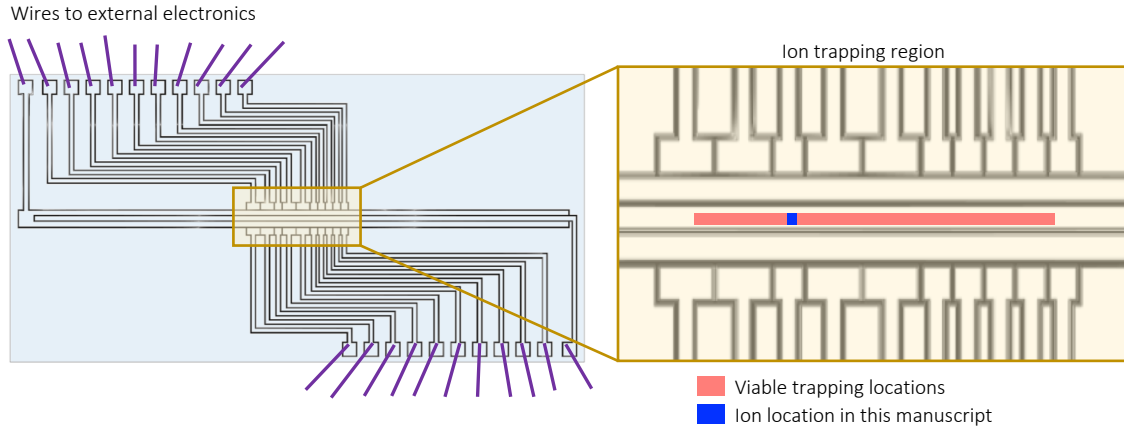


Figure 3.4: TRAP C electrode wiring and ion trapping position.

This chip contains 21 independent DC electrodes. The availability of a large number of electrodes is useful for surface treatment experiments, as treatments can sometimes cause electrodes to short. If DC electrodes short, then the voltages on the remaining DC electrodes can be adjusted to compensate. In addition, with this electrode design ions can be trapped at many different locations along the trap axis, as illustrated in Figure 3.4. The majority of measurements presented in this dissertation were taken at a single trapping location, but an earlier publication compared measurements from three separate locations in this trap ??.

The position of the ion along the trap axis is set by dynamically-adjustable voltages on the DC electrodes. In contrast, the height of the ion is fixed by the geometry of the RF electrodes, and cannot be altered. In this trap, the two RF electrodes are asymmetric, with widths of 65 and 80 μm , and they are separated by a distance of 105 μm . With this geometry, the ion height is fixed at 72 μm . Further details on trap potential control and simulation can be found in the Littich masters thesis [18].

After designing a chip and running simulations to confirm that it can produce a stable trapping potential for a calcium ion, the electrode pattern is etched into a fused silica chip. Trenches with 100 μm depth and 20 μm width surround all electrodes, as illustrated in Figure 3.5.

The surface is coated with 1.09 μm of metal, which is deposited via e-beam evaporation at a vertical angle of 45°. The angled evaporation coats the top surface of the electrodes with metal, which is necessary to conduct electricity to the trapping location, while preventing metal from coating the entirety of the trenches. To prevent metal from being deposited at the base of the trenches, all trench lines are oriented parallel to the trap edges, and evaporation takes place at a horizontal angle of 45°.

Evaporation is done from two orthogonal directions, as shown in Figure 3.5. With these two evaporation steps, we are able to coat the top 20 μm of each sidewall with metal. This coating acts as shield between the ion and the electrically-noisy dielectric substrate. In each evaporation step we include a titanium sticking layer, a thick layer of aluminum to act as the primary medium for electrical conduction, and a layer of copper to slow oxidation of the surface between and after evaporation steps.

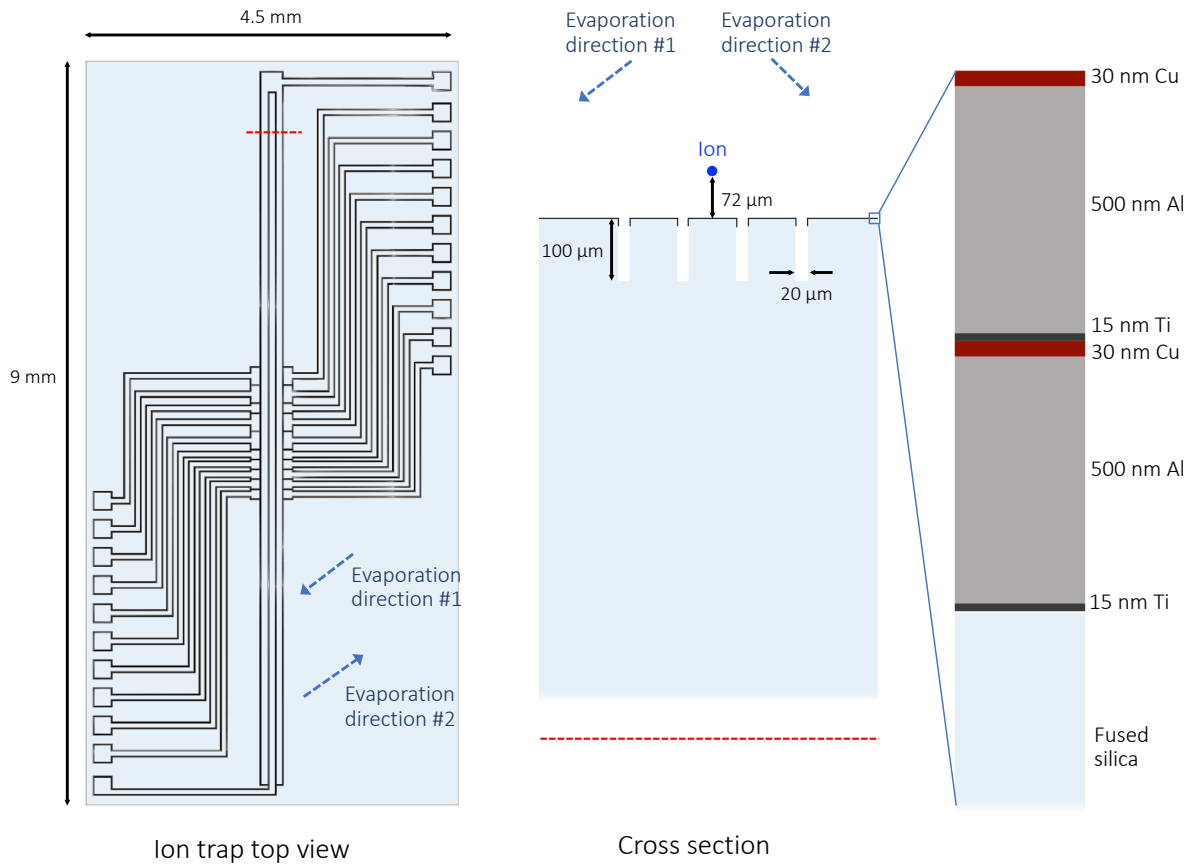
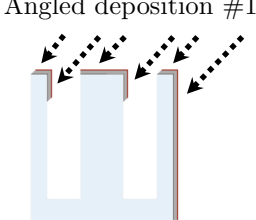
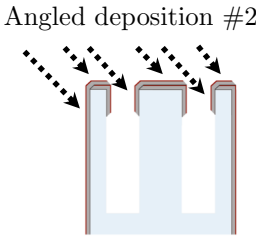
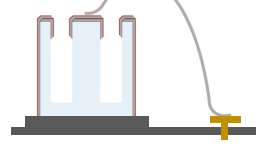
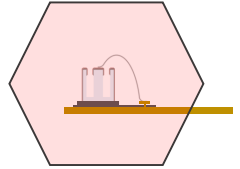


Figure 3.5: On the left is the top view of TRAP C, with arrows to illustrate the horizontal orientations of the two evaporation steps. In the center is a cross section of a portion of the trap illustrating the geometry of the trenches. This cross section also includes arrows to illustrate the vertical orientations of the two evaporation steps. On the right is a further zoomed-in cross section of the evaporated metal film after all evaporation has been completed.

3.3 Fabrication process

The following table (Table 3.1) contains the details of our ion trap microfabrication process, including trench etching and metal deposition. Information about the packaging and handling of the trap after fabrication is also included, as these steps affect the properties of the metal film. In Chapter 8 we will discuss how variations in handling correspond to variations in surface electric-field noise.

Table 3.1: Ion trap chip fabrication process

Step 1: Etch trenches into fused-silica chip	 	Laser weakening: Pattern trenches onto fused silica chip. using laser weakening. Remove material from trenches using hydrofluoric acid. Pattern designed at Häffner lab (Figure 3.5) Performed by Translume, Ann Arbor, MI [22].
Step 2: Deposit metal onto surface	 	Angled deposition #1: Remove organic contaminants in a Pirahna bath before deposition.  Electron-beam evaporation at two angles to coat the side-walls of the trenches and shield the ion from the noisy fused-silica dielectric. Pressure in chamber during evaporation = 5e-7 Torr. At first angle, deposit: 15 nm Ti (deposition rate = .5 Å/s) 500 nm Al (deposition rate = 5 Å/s) 30 nm Cu (deposition rate = 1 Å/s) Expose trap to atmosphere for 5 minutes to manually rotate the trap by 180°. Repeat deposition at second angle. Performed by Häffner lab at Berkeley Marvell Nanolab, Class100 clean room.
Step 3: Package and store trap		Mount chip to carrier and use wire-bonds to connect each electrode to the control electronics. Store trap in Class100 clean room at Marvell Nanolab until ion-trapping vacuum chamber is prepared.
Step 4: Install and bake		Install trap in vacuum chamber at Häffner lab. Bake vacuum chamber at 160° C, 1e-8 Torr, to achieve post-bake chamber pressure below 9e-11 Torr.

An image of an ion trap mounted and wire-bonded to a chip carrier is shown in Figure 3.6. This image was taken before the trap was baked.

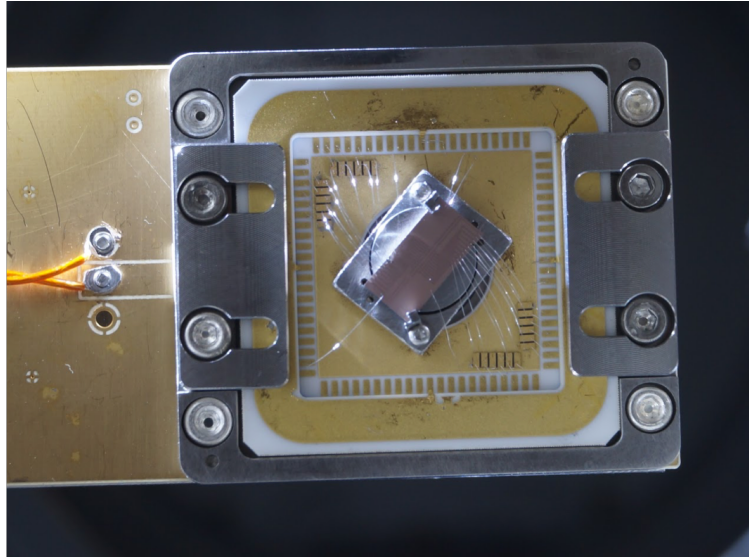


Figure 3.6: Photograph of an ion trap mounted and wire-bonded to a chip carrier.

3.4 Properties of the trap surface

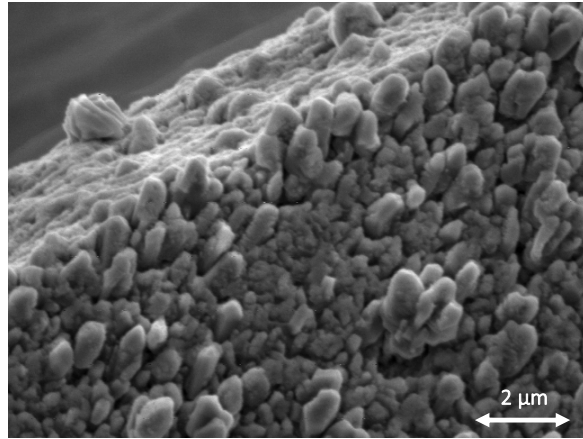


Figure 3.7: SEM of an ion trap surface at edge of a trench. This trap was fabricated as described in Table 3.1, and baked for 9 weeks at a temperature of 160 C under 5e-8 Torr vacuum before this image was taken.

The metal film on the surface of the trap is highly irregular, with features on the order of 1 μm in size. These features are visible the SEM image presented in Figure 3.7. The

trap in this image was fabricated with the process presented in Table 3.1 and baked for 9 weeks at a temperature of 160 °C. These features form during the evaporation process. Angled evaporation is known to enhance shadowing effects and grow bumpy surfaces [23]. In addition, hillocks form during evaporation if the evaporation-chamber pressure is higher than 1e-7 Torr [24]. The background pressure in the evaporation chamber during our deposition process is around 5e-7 Torr.

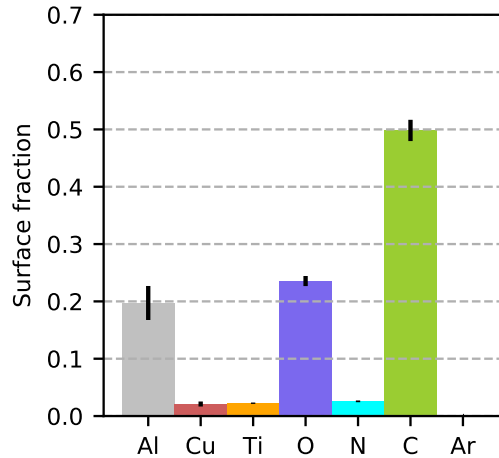


Figure 3.8: Relative surface fractions of metals and contaminants measured using in-situ Auger spectroscopy before milling of TRAP C.

Although the top 30 nm of the deposited metal film was pure copper when it came out of the evaporator, by the time we began performing surface treatment experiments, the surface composition had changed considerably. Many weeks of baking and local heating of the trap caused the metals to mix, bringing a considerable amount of aluminum to the surface. In addition, a large amount of oxygen and carbon were deposited onto the surface during extended periods of both atmosphere exposure and vacuum-chamber baking.

The complexity of the surface composition and topology of our ion trap substrate make its microscopic dynamics impossible to model from first principles. In addition, in a system with this complexity there can be many different noise processes taking place simultaneously. However, it has been shown that traps fabricated with these methods can have very low noise magnitudes compared to many other surface ion traps, as will be discussed in Chapter 8. For this reason, the traps produced by these methods merit investigation.

Chapter 4

Noise measurement methods

Measuring electric-field noise requires precise control over the electronic and vibrational energies of a trapped ion. In this chapter, we will first describe our optical control and read-out methods. Then, we will present the method that we use to measure the motional heating rate of the ion, and describe how this measurement can be used to determine the power spectral density of the electric-field noise that drives motional heating. Next, we will explain how the electric-field noise can be further characterized by frequency-scaling measurements. Finally, we will give an overview of the experimental setup that makes all of these measurements possible.

4.1 Optical control of calcium ions

A background on standard optical control methods for trapped $^{40}\text{Ca}^+$ ions can be found in the Roos thesis [25]. Here we will review only the basics of the methods required in our experiments.

To determine the motional state of an ion, we cycle through a specific laser-mediated control sequence while varying its timing parameters. The sequence has four major components: Doppler cooling, electronic initialization via optical pumping, coherent operation on a quadrupole transition, and electronic-state read out. The illustration of the electronic energy levels and transitions that are relevant to each step can be found in Figure 4.1.

At the beginning of each measurement, we use Doppler cooling to reduce the vibrational energy of the ion. This is accomplished using a 397 nm laser, which is red-shifted with respect to the transition between the electronic ground state and the short-lived (7 ns) $4\text{P}_{1/2}$ excited state, as illustrated in Figure 4.1a. The incoming photons are only resonant with the $4\text{S}_{1/2} \rightarrow 4\text{P}_{1/2}$ transition when the ion is approaching the laser, so each absorption event provides a momentum kick that counteracts the ion's motion. Each time this happens, the ion loses a small amount of vibrational energy. The absorption of a 397 nm photon is rapidly followed by a decay of the electronic state. If the ion decays to the $4\text{S}_{1/2}$ ground state, it can continue the cooling process by absorbing another red-shifted photon. If instead it decays to the meta-stable $3\text{D}_{3/2}$ state, as will happen 6.5% of the time, a 866 nm laser pumps the ion back to $4\text{P}_{1/2}$. We continue this process until cooling has plateaued.

After Doppler cooling, the ion may be in either of the two Zeeman sublevels of the

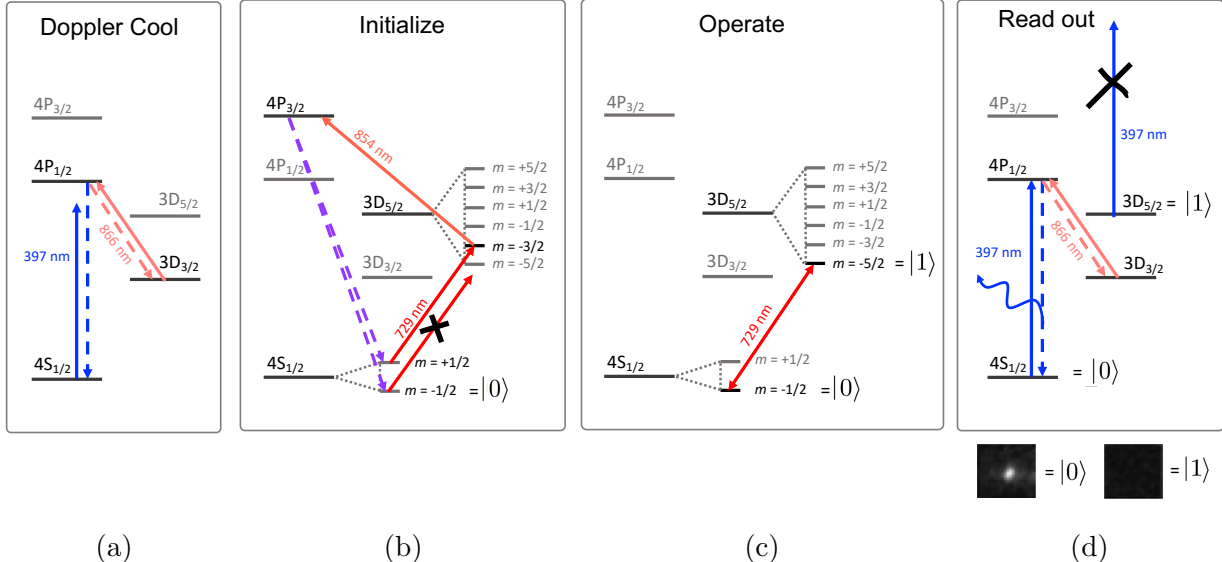


Figure 4.1: The hydrogenic level structure of $^{40}\text{Ca}^+$ in the context of our laser-mediated ion control scheme. Dotted lines correspond to spontaneous emission, and solid lines correspond to laser-driven transitions. (a) Doppler cooling with a red-shifted cycling laser and a re-pump laser. (b) Initialization via optical pumping, with a laser tuned to selectively pump the ion out of the $m = +1/2$ Zeeman sublevel of the ground state, and into the $m = -1/2$ ground state sublevel. (c) Quadrupole operation on the $\text{S}_{1/2} \leftrightarrow \text{D}_{5/2}$ qubit transition. (d) Optical read-out of qubit state via detection of emitted photons.

$4\text{S}_{1/2}$ ground state. Before we can commence with a controlled operation, the ion must be initialized to a specific sublevel. This initialization is performed via a process called optical pumping. A 2 G magnetic field removes the degeneracy of the Zeeman sublevels of the $4\text{S}_{1/2}$ and $3\text{D}_{5/2}$ states, splitting them by about 2 MHz, ensuring that these levels can be addressed individually.

With a 729 nm, 200 Hz line-width laser tuned to the $4\text{S}_{1/2}(m = +1/2) \leftrightarrow 3\text{D}_{5/2}(m = -5/2)$ transition, the ion is pumped selectively out of the $m = +1/2$ sublevel of the ground state. It is subsequently driven to the $4\text{P}_{3/2}$ level with a 854 nm laser, at which point it decays back down to the ground state, as illustrated in Figure 4.1b. If it decays instead to the $3\text{D}_{5/2}$ or $3\text{D}_{3/2}$ levels, it will be re-pumped to $4\text{P}_{3/2}$ by 854 and 866 nm lasers respectively (not pictured). If it decays to the $m = +1/2$ ground state, the optical pumping cycle will repeat. Finally, if it decays to the $m = -1/2$ ground state, the ion will no longer be able to absorb light from the 729 nm laser, and the pumping cycle will cease. If this process is carried out for a suitable amount of time, we can guarantee with almost perfect certainty that the ion will be pumped into the $m = -1/2$ ground state.

Now that the ion has been cooled and initialized, we can perform an operation on the $4\text{S}_{1/2}(m = -1/2) \leftrightarrow 3\text{D}_{-5/2}(m = -5/2)$ transition. This can be thought of as a qubit operation, where $|0\rangle = 4\text{S}_{1/2}(m = -1/2)$ and $|1\rangle = 3\text{D}_{-5/2}(m = -5/2)$, as illustrated in Figure 4.1c. This is a dipole-forbidden, quadrupole-allowed ($(\Delta m = 0, \pm 1, \pm 2)$) transition, and has a lifetime of about 1.2 s. The laser-driven transition rate depends on the parameters of the

laser, and on the vibrational energy of the ion. This interaction will be discussed further in Section 4.2. At the end of the quadrupole operation, the ion will be in a superposition of states $|0\rangle$ and $|1\rangle$.

In the read-out step of the control sequence, we use 866 and 397 nm lasers to read out the state of the ion as it is projected into either state $|0\rangle$ or state $|1\rangle$. If the ion is in state $|0\rangle$, it will cycle rapidly between the ground state and a short-lived excited state as described in the context of Doppler cooling and illustrated in Figure 4.1d. Each time the ion decays from this excited state, it emits a photon. In contrast, if the ion is in state $|1\rangle$, it will not cycle or emit light in the presence of a 397 nm driving laser. To determine the electronic state of the ion, we can either take an optical image of the ion, or collect its light with a . As shown in Figure 4.1d, the ion will appear as a bright spot on the camera if it is in state $|0\rangle$, and it will appear dark if it is in state $|1\rangle$. After the state has been read out, the ion is pumped into the $4P_{3/2}$ state with the 854 nm laser, at which point it decays down and is continuously Doppler cooled until the next experiment begins.

As experiments are carried out, the laser positions, frequencies, powers and pulse timings are frequently tuned to optimize the speed and precision of each step in the control sequence. The read-out excitation threshold and photon collection optics are also adjusted as needed.

4.2 Ion heating rate measurements

The vibrational energy state of the ion can be coupled to the electronic state via a simple qubit operation. Since we have all of the necessary tools to manipulate and read out the electronic state, we can take advantage of these same methods to measure the vibrational energy.

The ion is held in a 3D harmonic potential using the electronic trapping methods described in Chapter 3. In a quantum harmonic potential, states are evenly spaced, with a transition energy of $\hbar\omega$. The motional state of the ion can be characterized by its vibrational occupation numbers n_x , n_y and n_z , where x , y and z correspond to the axes of ion's motional modes. The magnitudes of the secular trap frequencies ω_x , ω_y and ω_z depend on the strength of the confinement along each axis.

As illustrated in Figure 4.2, we align the qubit operation laser so that it is nearly parallel with the z -axis. This ensures that our measurements of vibrational energy are dominated by the axial mode of motion. We are able to selectively probe a single mode of motion because our electric-field-noise detection method essentially measures the Doppler shift of the laser due to the motion of the ion. Oscillations perpendicular to the k - or of the laser will not induce a Doppler shift. In all future discussion of vibrational occupation numbers and secular trap frequencies, we will use the variables n and ω and it can be assumed that these correspond to n_z and ω_z .

A laser tuned to the qubit transition can drive the ion back and forth between the two qubit states in a process called Rabi flopping. With a few reasonable assumptions, we can describe the interaction between the trapped-ion qubit and the 729 nm laser with the following Hamiltonian:

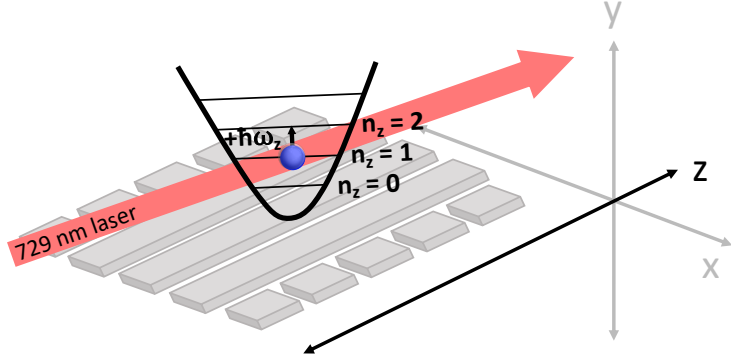


Figure 4.2: DC-electrode-generated axial confinement of the ion produces a harmonic trapping potential with evenly spaced energy levels. Alignment of the at a small angle (11.5°) to the z-axis implies that measurements of the motional occupation number will be dominated by the axial mode of motion.

$$H_I = \frac{1}{2} \hbar \Omega_n (\sigma^+ + \sigma^-) \quad (4.1)$$

where σ^+ and σ^- are the qubit raising and lowering operators, and Ω_n is the Rabi flop oscillation frequency. This Hamiltonian applies to a two-level system ~~with~~ motional mode, an exactly-resonant driving laser, and a motional heating rate far slower than the timescale of the Rabi excitation For a more thorough quantum-mechanical treatment of carrier Rabi flop measurements, and justifications for our simplifying assumptions, refer to the Noel thesis [26].

Rabi frequency Ω_n depends on the vibrational occupation number n , to first order, according to the equation:

$$\Omega_n = \Omega_0 (1 - \eta^2 n) \quad (4.2)$$

where Ω_0 is the bare Rabi frequency, and η is the Lamb-Dicke parameter η is proportional to the power of the driving laser. η depends on the secular trap frequency and the angle between the driving laser and the vibrational mode of motion. It characterizes the strength of the coupling between the electronic and vibrational energy states of the ion.

An ion under the Hamiltonian from Equation 4.1 will evolve in time according to the equation:

$$P_D(t) = \sin^2(\Omega_n t) \quad (4.3)$$

where P_D is the probability that the ion will be found in the $D_{5/2}$ state after a qubit operation pulse of length t . Rabi flops simulated from ions with the same bare Rabi frequency but different motional occupation numbers are plotted in Figure 4.3a. The excitation time on the x-axis corresponds to the pulse length of the qubit operation performed with the 729 nm laser.

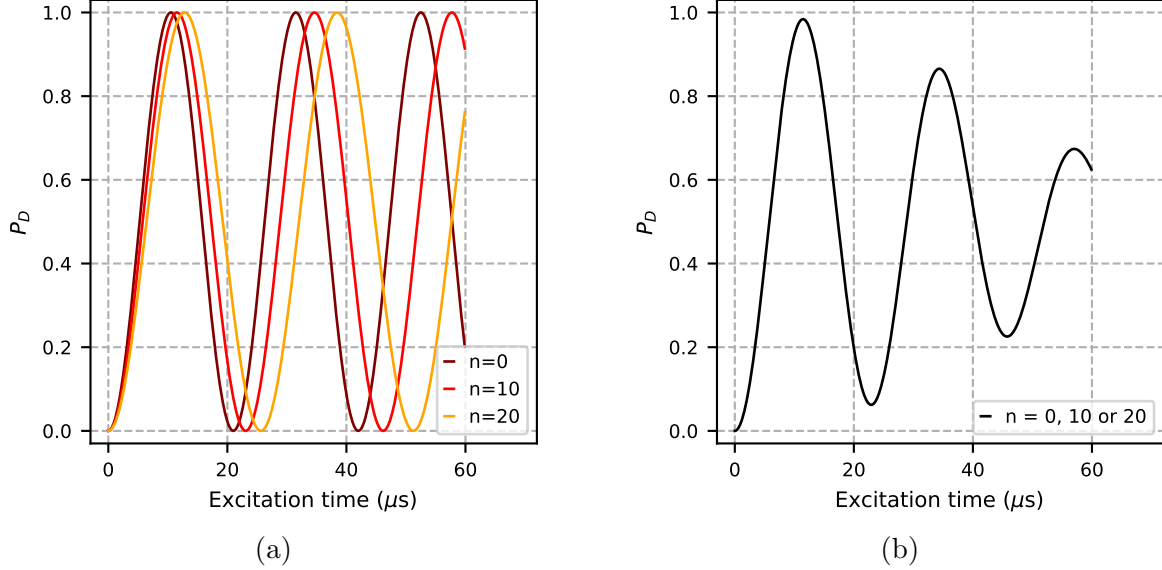


Figure 4.3: Simulated Rabi flops, where P_D is the excitation probability. (a) Ions with higher vibrational energies flop more slowly, as illustrated by Rabi flops from ions in three different Fock states. (b) If the ion is in an equal superposition of the three simulated Fock states, the Rabi flop will decay as a function of excitation time.

Since the frequency of the Rabi flop is tied to the motional state of the ion, we can measure the vibrational occupation number by mapping out a Rabi flop. However, this measurement is complicated by the fact that to map out a Rabi flop, the sequence of cooling, initialization, operation and state-readout must be repeated many times. Each time the ion is cooled, it can end up in one of many different motional states. As a result, the measured Rabi flop will be a convolution of many sine waves with different frequencies. This is illustrated in Figure 4.3b, where we have plotted a simulated measurement in which the ion had an equal probability of being in states $n=0$, $n=10$, and $n=20$. As shown, the Rabi flop decays as the three sine waves dephase.

It is reasonable to assume that an ensemble of Doppler cooled ions will have a thermal distribution of vibrational energies. A set of measurements from a single ion is equivalent to a single measurement of an ensemble of ions, so we can assume that the occupation probability P_n for any vibrational state n will be approximately equal to:

$$P_n = \frac{\bar{n}^n}{(\bar{n} + 1)^{n+1}} \quad (4.4)$$

where \bar{n} is the average motional occupation number. We combine Equations 4.3 and 4.4 to make a fitting function appropriate for our Rabi flop measurements:

$$P_D(t) = \sum_{n=0}^{\infty} P_n \sin^2(\Omega_n t). \quad (4.5)$$

We use this function to fit for \bar{n} and Ω_0 .

Examples of three Rabi flop measurements taken in our system along with fits to Equation

4.5 are plotted in Figure 4.4. Each point in this plot corresponds to 100 measurements in which the ion was cooled, initialized, operated on and read out. We plot in what fraction of these measurements the ion was projected into the excited $D_{5/2}$ state during state read out. Then, we change the excitation time (the qubit operation pulse length) and repeat this process to map out the Rabi flop. When Rabi flop data is fitted in practice, measured datapoints are weighted to account for projection noise, and an additional fit parameter is included to account for initialization errors.

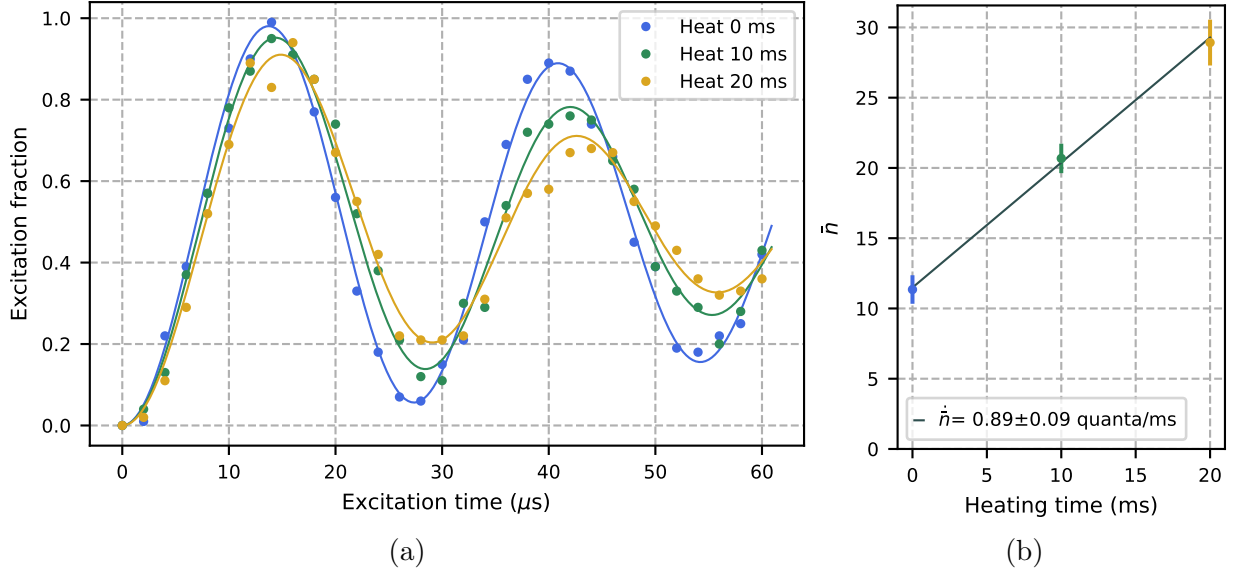


Figure 4.4: (a) Excitation fraction measurements (points) and Rabi flop fits (lines), taken with a secular trap frequency $\omega = 2\pi \times 1.3$ MHz. (b) Average occupation numbers extracted from Rabi flop fits (points) and a linear fit (line) to determine the ion heating rate.

Figure 4.4b contains the \bar{n} values associated with the fits from Figure 4.4a. Heating time, on the x-axis, corresponds to a waiting time added between the initialization and operation steps of each measurement. Since the ion is not cooled during this waiting time, it is free to heat up in response to electric fields fluctuating at the secular trap frequencies. The longer the ion is allowed to heat, the higher \bar{n} will become. The ion heating rate is equal to the slope of a linear fit of \bar{n} with respect to the heating time.

4.3 Calculation of electric-field noise

The electric-field-noise power spectral density $S_E(\omega)$ is directly proportional to the ion heating rate according to the equation [1]:

$$S_E(\omega) = \frac{4m\hbar\omega}{q^2} \dot{n}(\omega), \quad (4.6)$$

where m and q are the mass and the charge of the ion, \hbar is the reduced Planck constant, and ω is the secular trap frequency. $S_E(\omega)$ is a measure of the amplitude of the electric-field-

noise at frequency ω . The power spectral density depends on the autocorrelation function of the fluctuating electric field according to the equation:

$$S_E(\omega) = 2 \int_{-\infty}^{\infty} d\tau \langle \delta E_t(\tau) \delta E_t(0) \rangle e^{-i\omega\tau}. \quad (4.7)$$

The majority of the data in this dissertation will be presented in the form of ion heating rates. These heating rates are scaled to a measurement frequency of $2\pi \times 1$ MHz unless otherwise specified. A heating rate of 1 quanta/ms measured by $^{40}\text{Ca}^+$ with a trap frequency of $2\pi \times 1$ MHz corresponds to a power spectral density of $6.85 \times 10^{-12} \text{ V}^2/(\text{m}^2 \text{ Hz})$.

4.4 Frequency scaling of ion heating rates

We further characterize noise in our system by measuring heating-rate amplitudes at a range of different frequencies. This is called a frequency-scaling measurement.

Our heating rates, as described in Section 4.2, are sensitive only to noise at the axial trap frequency. In the axial direction, harmonic confinement is generated by DC electrodes, which can be tuned to set the measurement frequency anywhere between 0.4 and 2.4 MHz. We do simulations to predict the DC voltages that are needed to set the trap frequency to a specific value. After the DC voltages have been set, the trap frequency can be measured and adjusted with a precision of about 1 kHz.

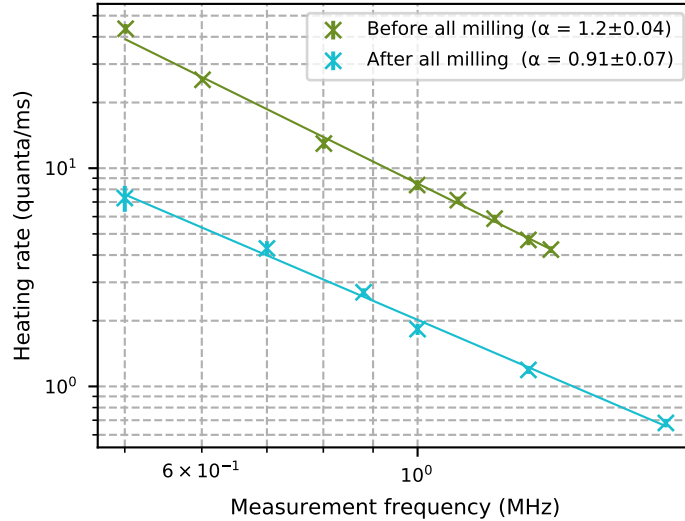


Figure 4.5: Frequency scaling measurements of ion heating rates taken in TRAP C while the substrate was at room-temperature.

Two frequency-scaling measurements are plotted in Figure 4.5. One was measured before TRAP C was milled, and other was measured when the noise was at its lowest point after extensive milling. In both cases, the heating rate scaled as:

$$\Gamma = \dot{n} \propto 1/f^{1+\alpha} \quad (4.8)$$

where Γ is the ion heating rate and α is the so-called frequency scaling exponent of the noise. The corresponding noise power spectral density scales as $1/f^\alpha$. Noise that has this frequency dependence, and a value of α close to 1, is referred to in academic literature as 1/ noise, flicker noise, or pink noise. 1/f noise is found in many physical systems, and in Chapter 6 we will discuss how previous measurements and models of 1/f noise can inform our study of noise in ion traps.

In addition to establishing a link  between our work and other studies of 1/f noise, the data presented in Figure 4.5 helps us confirm that our heating rate measurements are not dominated by technical noise. We put great care into filtering electrodes, shielding the trap from electromagnetic pickup, and choosing electronic grounding configurations so that measurements in our system are surface-noise limited. Technical noise often has sharp frequency resonances. Our noise measurements at different frequencies form a smooth line, and show no indication of resonances. In addition, the amplitude of technical noise can vary by orders of magnitude over daily or hourly time periods. In our measurements, the heating rates are very stable over time. This gives us confidence that technical noise is not a problem in our system.

Both of the frequency scaling measurements plotted in Figure 4.5 were taken while the trap substrate was at room temperature. We also have taken many measurements of α while the substrate temperature was elevated. In early measurements of TRAP C, we confirmed that the noise generated by the heated substrate had a frequency scaling consistent with Equation 4.8. This work is published in reference ??.

4.5 Experimental setup

Accomplishing the feat of trapping an ion and measuring its heating rate requires a large number of tools. Pictured in Figure 4.6 is the vacuum chamber that houses TRAP C, and many of the instruments required in the ion trapping process.

Vacuum

All ion-trapping experiments are performed in UHV chambers. If a gas molecule collides with a trapped ion, the ion can be ejected from the trap, so ideally all background gasses should be removed.

To achieve low pressures in our experiment, our trap is installed in a vacuum chamber and then the whole chamber is baked at 160° C for two or more weeks. During the baking process, a pressure of  Torr is maintained by two turbo pumps. After baking is complete, a titanium sublimation pump is run to further reduce the pressure.

During general operation of the ion trap, the chamber is continuously pumped by an ion pump, which is able to achieve pressures below $1\text{e-}10$ Torr. At these low pressures, the average ion lifetime is approximately 6 hours. The pressure in the chamber is measured using a residual gas analyzer (RGA).

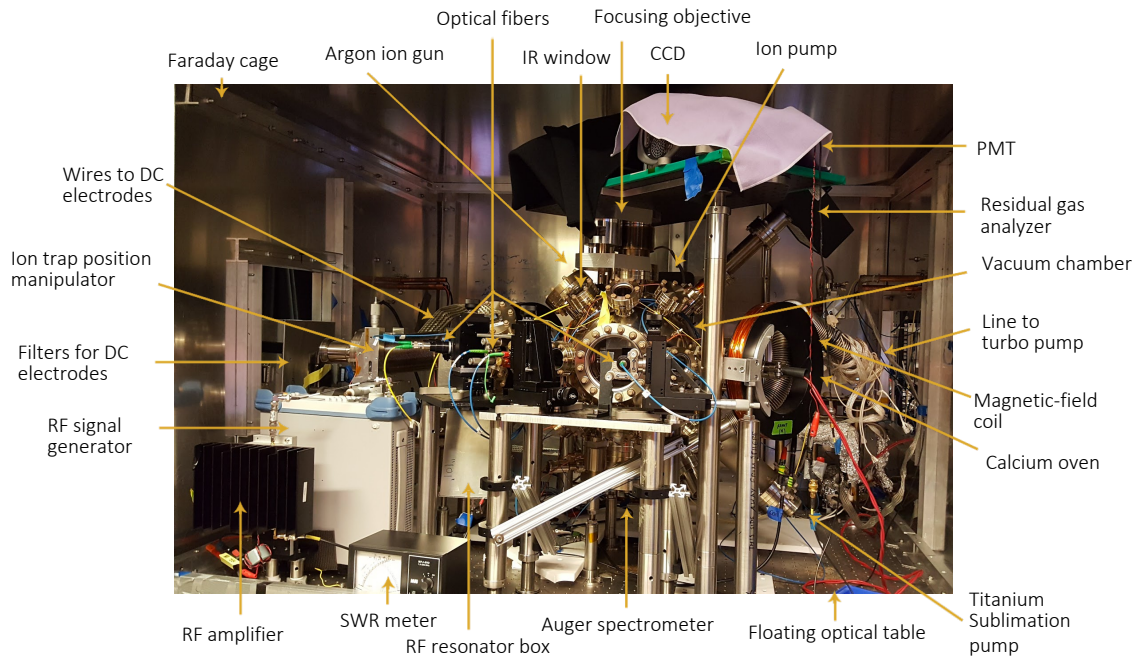


Figure 4.6: Photograph of our ion trapping chamber and other various tools.

Ion trapping electronics

In Chapter 3, we described how RF and DC voltages applied to ion trap electrodes can create a stable trapping potential for a $^{40}\text{Ca}^+$ ion.

In our setup, DC voltages are set via a computer interface. The computer communicates to an FPGA (field programmable gate array) which sends a signal to a series of DACs (digital to analog converters) which output voltages. These voltages are then amplified to the desired values, which can be between -40 and +40 V. Between the amplifier and the trap electrodes there are five stages of RC filters, plus a set of capacitors soldered directly to the chip carrier. These filters remove excess electric-field noise that could interfere with measurements of surface noise.

In an additional effort to minimize electronic noise, the entire vacuum chamber is surrounded by a 1.25 mm thick aluminum Faraday cage. Wires and power cables are low-pass filtered as they enter the cage.

Inside the Faraday cage, a Rohde & Schwarz signal generator outputs the RF signal required for radial confinement of the ion. This signal is amplified, passed through an SWR meter and inductively coupled to the in-vacuum RF electrode circuit via a helical resonator. The frequency of the output signal is tuned to maximize the ratio between the forward and reflected RF power, as measured on the SWR meter.

In addition to trapping electronics, two coils of wire are present on opposite ends of the vacuum chamber. By passing a current through these coils, we generate a 2 G magnetic field to control and separate the Zeeman sublevels of trapped ion.

For further details and diagrams of our trapping electronics, filtering, and vacuum system,

refer to Chapter 4 of the Noel thesis [26].

Calcium ion generation

Once the RF and DC trapping voltages are in place, we use a two-photo photoionization process to generate ions from a beam of neutral atoms as it passes through the trapping location.

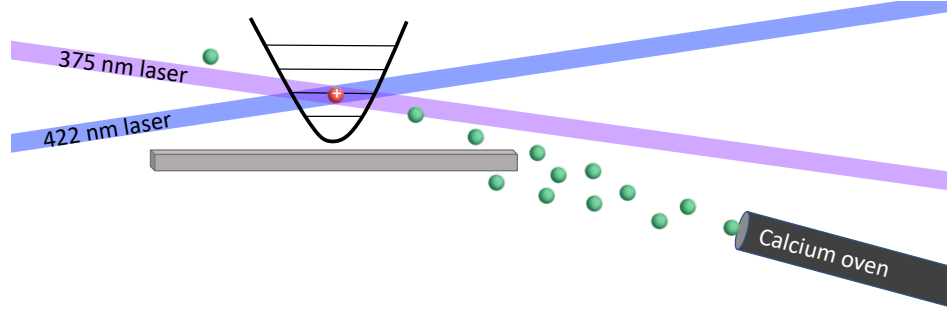


Figure 4.7: Diagram of calcium ion generation. A beam of neutral calcium atoms (green) passes through the electronic trapping point, while intersecting with lasers that excite and ionize the calcium. Trapped, ionized calcium is shown in red.

The neutral atom beam is produced by a home-built calcium oven. The oven consists of a thin tube with calcium granules placed at its base. When the tube is resistively heated, it produces a beam of calcium atoms. The tube is placed below the trap and angled upward, as shown in Figure 4.7, so that calcium atoms can reach the trapping location but will not be deposited onto the surface of the trap.

The two lasers for the two-photon photoionization process are aligned to intersect at the ion trapping location above the surface of the trap. A portion of the calcium ions will be excited by the 422 nm laser, and subsequently ionized by the 375 nm laser. Doppler cooling lasers are also present (though not picture) to cool down the ions so that they can be trapped.

Lasers

As presented earlier in this chapter, the electronic state of the ion can be manipulated and read out using four lasers with wavelengths of 397, 729, 854 and 866 nm. Calcium is ionized using two additional lasers with wavelengths of 375 and 422 nm. The injection-locked 729 laser is described in Section 4.1 of the Gorman theses [27]. The setups of the other five lasers are described in Chapter 3 of the Pruttivarasin thesis [28].

The two photoionization lasers are manually unblocked when a new ion needs to be trapped, and manually re-blocked once trapping has been successful. However, during the process of taking heating-rate measurements, the cooling and state-control lasers must be turned on and off with sub-microsecond precision. In addition, their frequencies must be dynamically tuned to selectively drive different transitions in the ion. For these reasons, the measurement lasers must be controlled digitally.

At the beginning of each experiment, the parameters of its pulse sequence are programmed into a computer. This computer communicates with an FPGA, which transmits precisely-timed electrical signals to four acousto-optic modulators (AOMs). Each of the AOMs controls the frequency, amplitude and phase of one of the four measurement lasers.

After each laser beam is doubled through an AOM, it is coupled into an optical fiber. The laser output from each fiber is aligned to the trapped ion. To reduce vibrations, the whole setup is mounted to a floating optical table. The table and some of the optical fibers are visible in Figure 4.6.

Imaging

A trapped calcium ion emits 397 nm light as it cycles between the $4S_{1/2}$ and $4P_{1/2}$ energy states. We use this light to identify when an ion has been trapped, and to determine its electronic state after a qubit operation. The emitted light is focused through an objective aligned above the trap, then passed through a filter to remove stray light of other wavelengths, and finally directed into either a PMT or a CCD camera. Both the PMT and camera are used to detect ions when they are initially trapped, but only the PMT is used for state readout.

Control system

All ion measurement experiments are run via the LabRAD digital control software, as described in Appendix A of the Ramm thesis [29]. We use this software to control the voltages on the DC electrodes, run laser pulse sequences, record the ion fluorescence, and process the collected data.

Surface treatment and characterization tools

In addition to all of the equipment used for ion trapping and heating-rate measurements, some of our surface treatment and characterization tools are also pictured in Figure 4.6. These tools include an Auger spectrometer positioned below the vacuum chamber, an argon ion gun at the back of the chamber, and an IR window through which we can detect light for substrate temperature measurements. Also pictured is the ion trap position manipulator, which allows us to rotate and shift the trap so that it can be aligned to each of these treatment and characterization tools. These tools will be discussed in the following chapter.

Chapter 5

Surface treatment & characterization techniques

The experiments presented in this dissertation incorporate a range of different in-situ surface treatment and characterization techniques. An illustration of how these tools are arranged around the ion trap is shown in Figure 5.1.

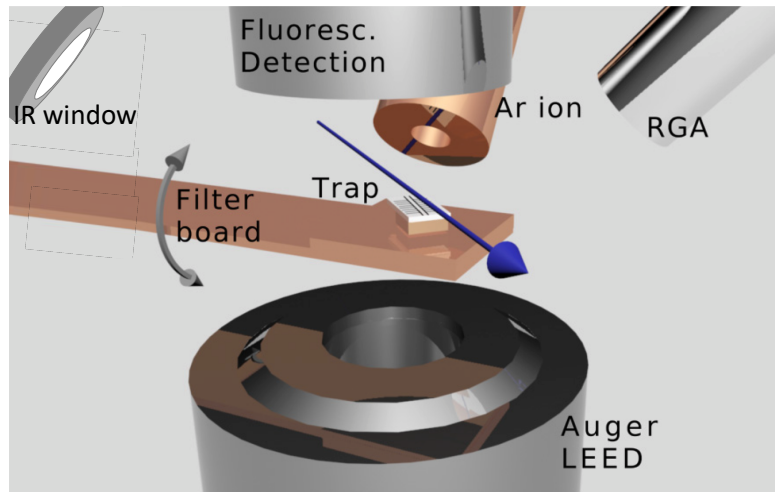


Figure 5.1: Arrangement of in-situ surface treatment and characterization tools. Adapted from [11]

Earlier, in Figure 3.6, we showed how the ion trap is clamped and wire-bonded to a chip carrier. This chip carrier is screwed onto a filter board, which is attached to a manipulator arm. With this manipulator arm, the trap can be rotated by $\pm 180^\circ$ and moved along the x, y and z axes without breaking vacuum. The trap must be shifted and rotated each time we switch between taking ion-heating-rate measurements, doing argon ion milling, or using the Auger spectrometer.

During ion-heating-rate measurements, the trap is faced upward and aligned to the center of the fluorescence detection optics. Lasers for ion trapping and state manipulation enter the chamber parallel to the trap surface through a series of windows. The trap is rotated downward for Auger spectroscopy, and diagonally backward for argon ion milling.

In this chapter we will describe the tools we use to treat and characterize the trap surface in-situ. For a summary of all surface treatments and measurement results, refer to Chapter 7.

5.1 Trap substrate heating

The trap sits directly on top of a resistive button heater that was manufactured by HeatWave Labs (101136 0.320" 1200oC UHV Button Heater). With this heater, the temperature of the trap can be raised to over 620 K. 

The heater and trap are clamped together and thermally isolated from the gold-plated top of the ceramic chip carrier using a stainless-steel holder. This holder was built by machinists in the UC Berkeley Physics Machine Shop. The heater stem and wire pass through a hole in the center of the chip carrier, where the stem is secured by a small screw and the wire is connected to an external power source. An exploded image of this setup is shown in Figure 5.2.

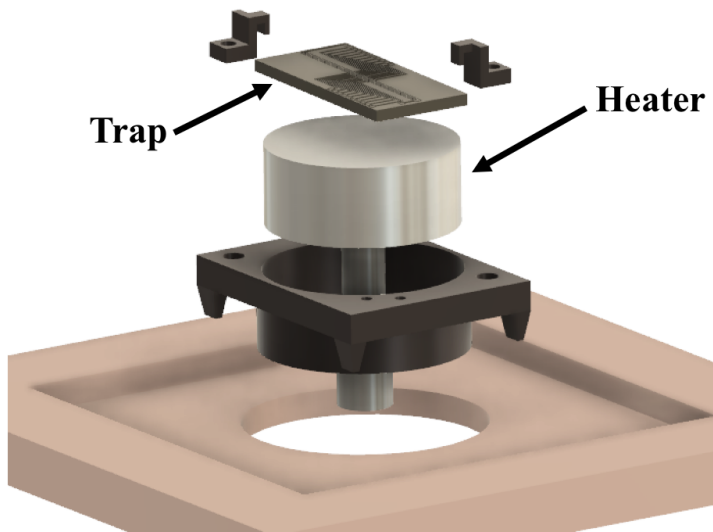


Figure 5.2: Exploded image of the trap, button heater, steel holder, and chip carrier.

Substrate temperature measurement

We use a Seek Thermal, model CompactXR, camera to determine the temperature of the heated trap. An IR-transmitting ZnSe window is installed in the chamber so that the trap temperature can be taken while the trap is oriented for ion-heating-rate measurements, as shown in Figure 5.1.

A thermal image of the trap, heater and holder, as shown in Figure 5.3, will display a range of different temperatures. The temperature read out directly from an object will be a convolution of its true temperature and the emissivity  of its surface. Surfaces with emissivities close to 1, such as glass, are read out most accurately. Surfaces with lower

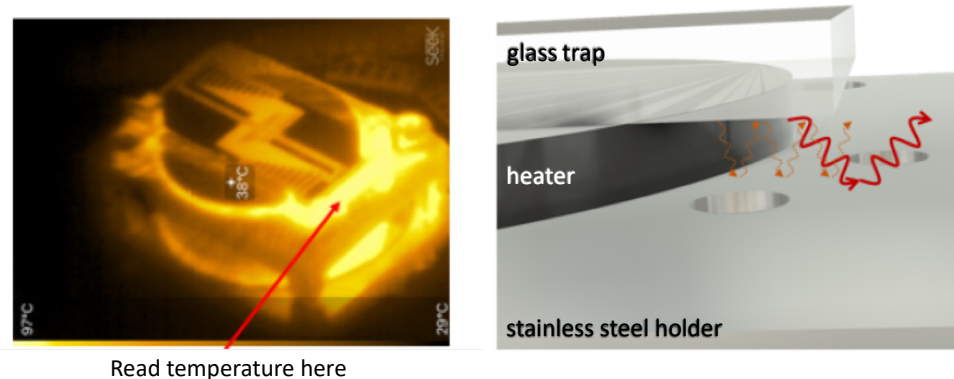


Figure 5.3: Left: thermal image of heated ion trap and holder. Right: cartoon illustrating the path of photons emitted from the glass bottom of the ion trap.

emissivities, such as the metal-coated surface of an ion trap, appear in the thermal camera to be colder than they actually are.

Although the top of the fused-silica trap is coated with metal, the bottom is smooth and glassy, and thus has an emissivity close to 1. The corners of the trap hang off the top of the heater, which is raised slightly above the base of its holder. This leaves just enough space for blackbody radiation emitted from the bottom of the fused silica chip to reflect off of the stainless steel holder and then out through the ZnSe window. With this reflected light, we can accurately determine the temperature of the trap. The cavity created between the glass and the holder, as illustrated on the right in Figure 5.3, further enhances the accuracy of this measurement.

Before the reflected blackbody radiation reaches the infrared camera, it passes through a window and a series of lenses that attenuate its intensity. We use a second ZnSe window, identical to the one installed on the vacuum chamber, to calibrate the thermal camera and lenses before they are mounted in place for in-situ measurements. In this calibration process, we cycle a hot plate through a wide range of heat settings. We measure the hot-plate temperature directly using a thermal imaging gun, while also measuring the temperature read out by the thermal camera through the ZnSe window. With these measurements, we generate a mapping between the true temperature and the read-out temperature. All substrate temperatures reported in this dissertation have been scaled using these mappings.

Temperature scaling of ion heating rates

A measurement of how surface electric-field noise responds to heat can provide valuable information about the microscopic noise sources. In our experiments, we determine the temperature scaling of the surface noise by measuring ion heating rates between room temperature and 605 K. At around 600 K, the trapped ion can be held in the trap for an average of five minutes before ejection. The lifetime rapidly deteriorates at temperatures above 600 K. Ions cannot be trapped at all when the substrate temperature is above 605 K.

In Figure 5.4a is a plot of a measurement in which we raised the temperature of the trap from room temperature to 580 K, while stopping periodically to measure heating rates

at 0.88 and 1.3 MHz. We did measurements similar to this before and after every surface treatment described in this dissertation. By measuring temperature scalings simultaneously at multiple frequencies, we are able to determine how the frequency scaling exponent α scales with temperature. This is valuable information in the context of the TAF model, which we will discuss in Chapter 6. In later chapters, when we explore how the magnitude of the heating rates change in response to surface treatments, it is much simpler to present single-frequency temperature scalings.

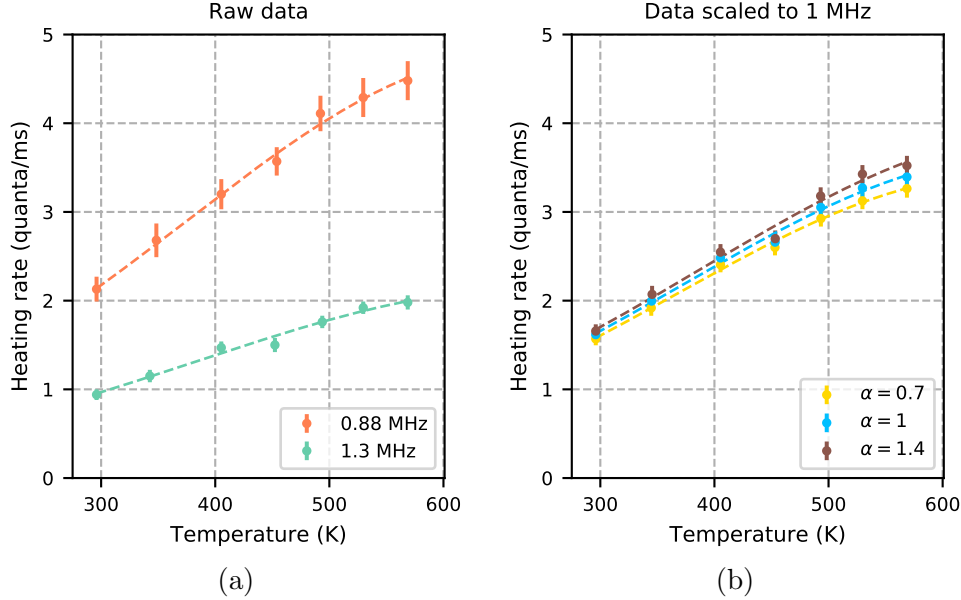


Figure 5.4: (a) Temperature scaling of heating rates, measured with two different measurement frequencies. (b) Temperature scalings re-scaled to a measurement frequency of 1 MHz using three different values of α . Even using the highest and lowest measured values of α , the re-scaled temperature scalings differ by at most one standard deviation from $\alpha=1$.

Unless otherwise specified, all temperature scalings presented in this dissertation are scaled to 1 MHz assuming the heating rates scale as $1/f^\alpha + 1$ where $\alpha = 1$. After data has been scaled, measurements taken at similar temperatures are averaged together. Values of α measured throughout our experiments typically lie between 0.9 and 1.1, but outliers have been as high as 1.4 and as low as 0.7. Figure 5.4b shows the data from Figure 5.4a scaled to 1 MHz assuming three different values of α . Since we typically measure heating rates at frequencies both above and below 1 MHz, the chosen value of α has very little impact on the magnitude of the re-scaled temperature scaling.

In all temperature scaling plots, the temperature on the x-axis refers to the temperature of the substrate. The heating rate on the y-axis refers to the rate of the rise of the motional state of the ion in response to electric-field noise, as introduced in Chapter 4. To avoid confusion, we will often refer to the heating rate as the *ion heating rate*. If the word ion is ever omitted, it is for the sake of brevity, and is never in reference to a different type of heating.

Heat as a surface treatment

In a typical heating experiment, we measure the temperature scaling as the temperature is raised, and again when it is lowered. In some experiments, such as the one plotted in Figure 5.5a, the initial and final temperature scalings match. In other experiments, the substrate is transformed by the heat treatment, and we observe that the initial and final temperature scalings are different. An example of this type of experiment is shown in Figure 5.5b.

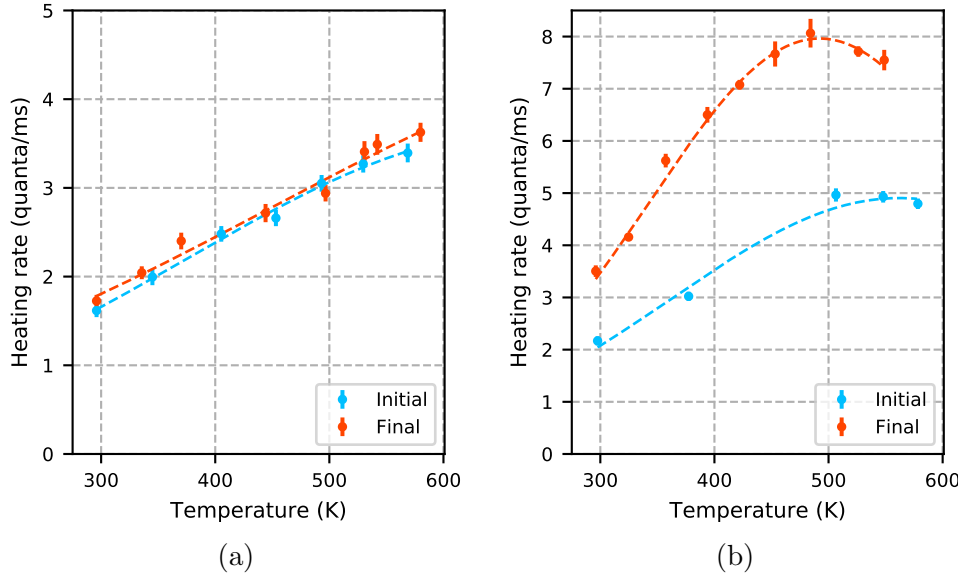


Figure 5.5: Examples of heating experiments in which (a) the initial and final temperature scalings match, and (b) the heat transforms the substrate, thus changing the temperature scaling.

A chronological summary of all of the heating experiments we have done can be found in Chapter 7.

5.2 Auger spectroscopy & electron bombardment

Tools

The surface composition of the trap is measured in-situ using an Auger spectrometer (OCI Vacuum Microengineering model BDL800IR). The system includes an electron-beam power supply (model LPS-075/300), a lock-in amplifier (model SR830), and retarding field analyzer a gold-coated-tungsten wire-mesh grid. The electron beam has an energy of 2 keV and is generated by a thermally emitting tungsten-rhenium filament. The tool has a 20 mm sample-to-optics working distance, and when the electron beam reaches the trap it has a diameter of 1 mm, as illustrated in Figure 5.6.

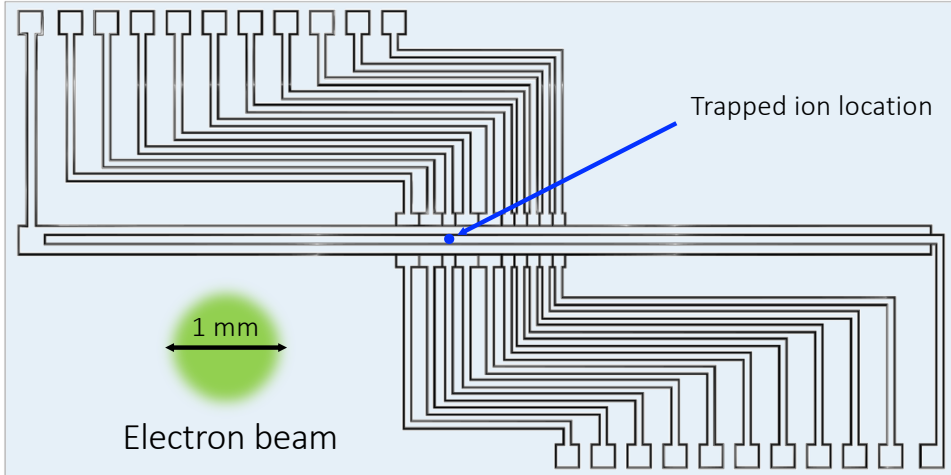


Figure 5.6: The spot size of the Auger electron beam shown in the context of the ion trap substrate.

Auger spectrum data processing

The lock-in amplifier outputs the derivative (dN/dE) of the Auger-electron emission amplitude (N) as a function of energy (E). This is the signal that we analyze and plot. The energies, shapes and relative amplitudes of the peaks in an Auger spectrum can be used to gain information about the atomic and chemical composition of the surface of the substrate. This measurement is sensitive to the top 3 to 10 monolayers of material [30].

After taking an Auger spectrum, the first thing that we do is identify the elements on the surface by comparing measured peaks to known reference spectra. In our measurements, we have found signals from aluminum, copper, titanium, nitrogen, oxygen, carbon and, after ion milling, argon. Next, we use a three-step process to remove background from the data. These steps are shown in Figure 5.7 using one of our measured spectra as an example.

In Step 1, we remove the peaks from all identified elements by replacing the signal from each element with a straight line. The line resulting from this removal is shown in red in Step 1 of Figure 5.7, along with the raw data which is plotted in black. Next, we use a Savitzky–Golay filter to smooth the red line. The smoothed line is shown in red in Step 2. Finally, we subtract the background (the red line in Step 2) from the raw data. The final background-subtracted result, for this example, is plotted in green.

The relative amplitudes of the differential Auger peaks are used to determine the atomic composition of the trap surface. In Figure 5.8, we have plotted a background-corrected spectrum and highlighted the strongest (high energy) peak from each element. To determine the fraction of each element, we measure the peak-to-peak amplitude of all of the strongest peaks. This amplitude is equal to the difference in voltage between the lowest and highest points in each highlighted region. Each amplitude is scaled by the Auger sensitivity of its corresponding Auger energy. These sensitivities were provided by the manufacturer of the spectrometer, and are listed in Table 5.1.

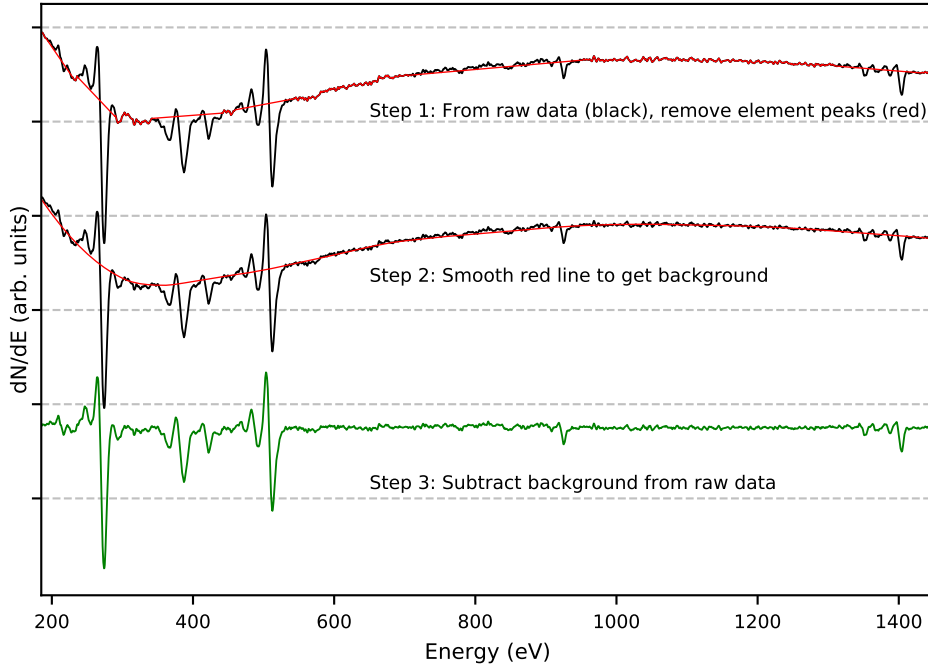


Figure 5.7: Illustrate of our background correction method using a typical measured Auger spectrum as an example.

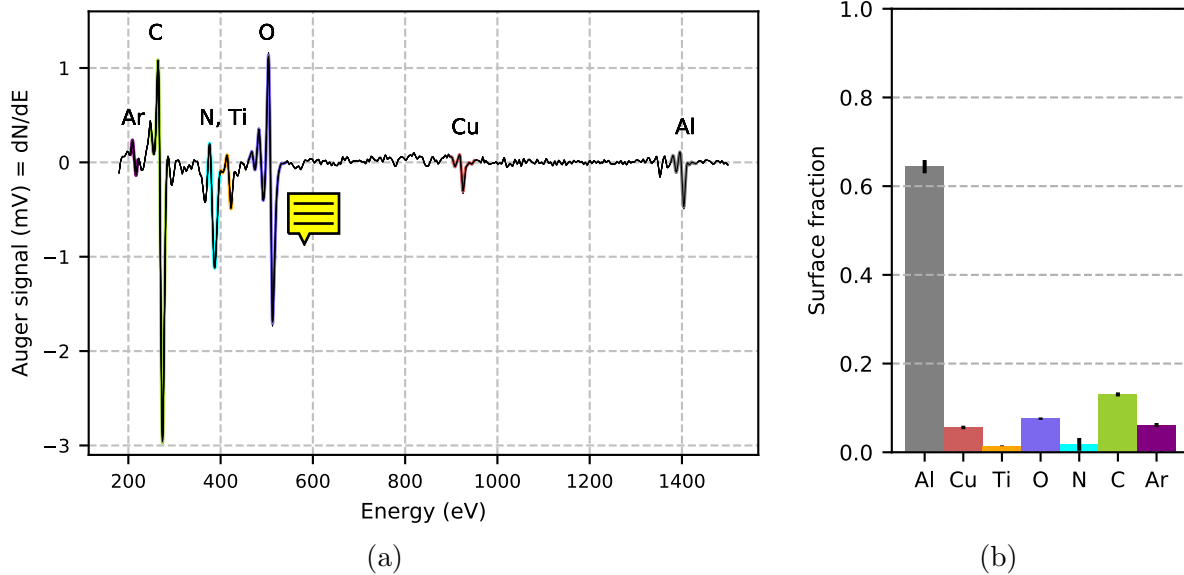


Figure 5.8: This data corresponds to [Electron 4](#) in Chapter 7. (a) Auger spectrum with the strongest peak of each element highlighted. (b) The atomic surface composition extracted from (a).

The surface fraction of a given element is proportional to the peak-to-peak amplitude of its strongest peak, divided by the corresponding Auger sensitivity. This procedure works well for all elements except for nitrogen, which will be discussed separately. After all amplitudes have been measured and scaled, the set is normalized so that all fractions add up to 1. The

Table 5.1: Auger sensitivity

Element	Peak energy (eV)	Auger sensitivity
Aluminum	1396	.0076
Aluminum oxide	1396	.0076
Argon	215	.0522
Calcium	294	.5543
Carbon	272	.2426
Copper	920	.0639
Nitrogen	379	.0921
Oxygen	503	.3023
Titanium	418	.3297

surface composition corresponding to the Auger spectrum in Figure 5.8a is shown in Figure 5.8b.

The surface fractions plotted in figure 5.8b include an error bar that corresponds to the peak-to-peak measurement uncertainty. Each Auger scan has some high-frequency, low-magnitude noise. A zoomed-in plot of a portion of a scan containing no Auger peaks is shown in Figure 5.9. The standard deviation of this data is 0.2 mV, so it gives rise to a peak-to-peak error of 0.3 mV.

The errors reported in Figure 5.8b are equal to the 0.3 mV error scaled by the Auger sensitivities from Table 5.1 and multiplied by the normalization factor. The reported error is a lower bound. It does not account for imperfections in background correction, uncertainty in the scaling factors, or the fact that electrons with different energies can travel different distances through the substrate. In addition, this error does not account for electron-beam-induced changes in the surface composition. The Auger measurement process deposits carbon and can cause low-energy elements such as oxygen and nitrogen to desorb from the surface. Since elements are measured one-by-one, the calculated surface fractions will not exactly represent the state of the substrate either before or after the spectrum was taken.

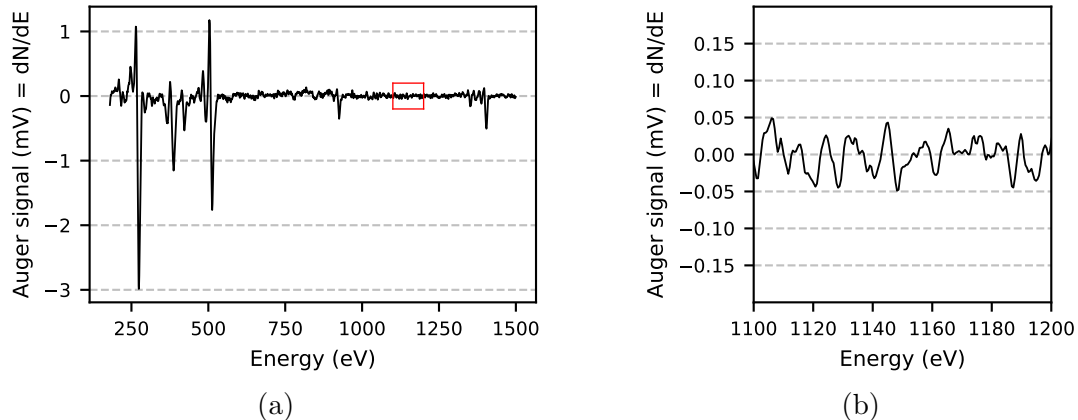


Figure 5.9: (a) Background-corrected Auger scan. (b) Zoom in on area of scan with no Auger peaks, illustrating high-frequency noise with a standard deviation of 0.2 mV.

We will now address how we determine the surface fraction of nitrogen. The measurement of nitrogen is complicated by the fact that its strongest peak  overlaps exactly with the second-strongest titanium peak. As a consequence of this, to determine the amplitude of nitrogen we must somehow subtract out titanium. The subtraction process is further complicated by the fact that the relative heights of the two titanium peaks are altered when titanium is bound up with oxygen, nitrogen, or carbon, as shown in Figure 5.10.

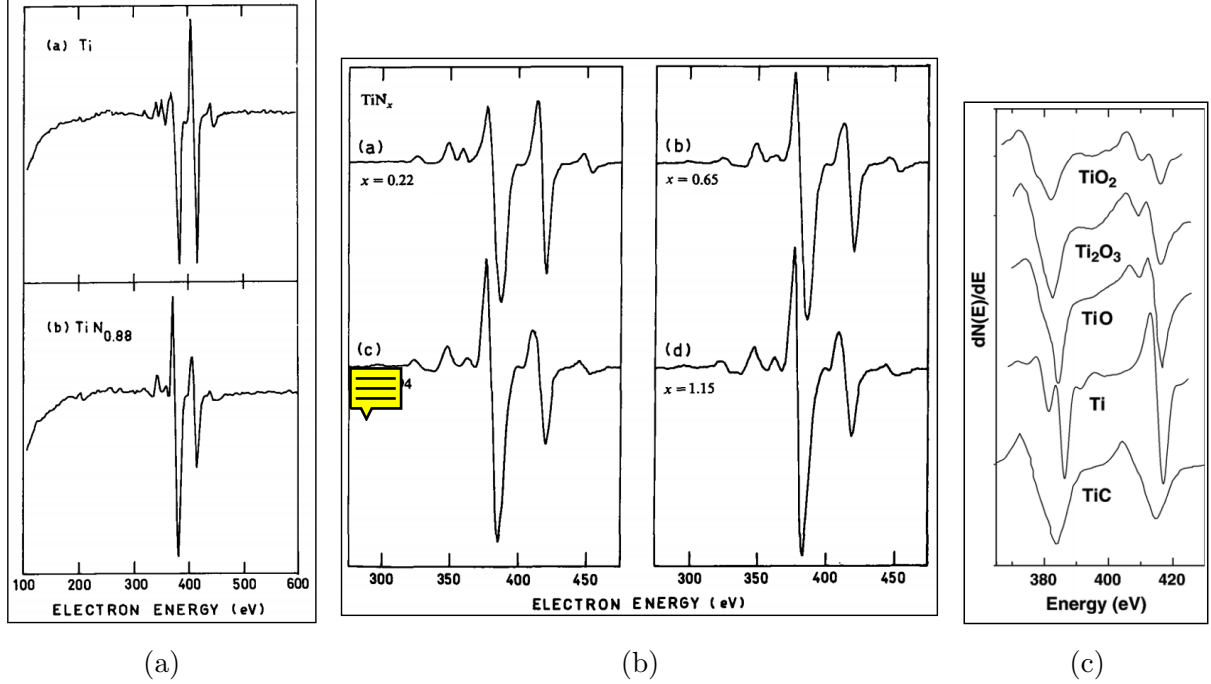


Figure 5.10: Sample Auger spectra of titanium in different chemical states, reproduced from (a) [31], (b)[31], (c)[32].

Four representative titanium spectra measured throughout our surface treatment experiments are shown in Figure ???. The line labelled *Electron 1* was taken before all argon ion milling, but after extensive heating. The other three spectra were taken after increasing amounts of argon ion milling and heat treatments. The four spectra are measured chronologically, top to bottom. When we line-shapes from Electron 1, Mill 6 and Electron 4 are compared to the reference spectra from Figure 5.10, we see that the shapes look consistent with titanium nitride, but the features are not clear enough to make a definitive judgement. In contrast, in the spectrum from Electron 2 the 380 eV peak is far stronger than the 420 eV peak, indicating that a large amount of nitrogen is present.

To estimate the surface fraction of nitrogen, we first measure the peak-to-peak amplitudes of both the 380 and 420 eV peaks. We set the nitrogen amplitude to the amplitude of the 380 eV peak minus the amplitude of the 420 eV peak. We set the error of the nitrogen amplitude to the amplitude of the 420 eV peak. With this analysis method, it is clear that in most scans there is some probability that a small amount of nitrogen is present, but that the uncertainty in this value is large, as shown in Figure 5.8b. In scans where the 380 eV peak is much stronger than the 420 eV peak, the nitrogen signal appears very clearly in the calculated surface fractions, as shown in Figure ??.

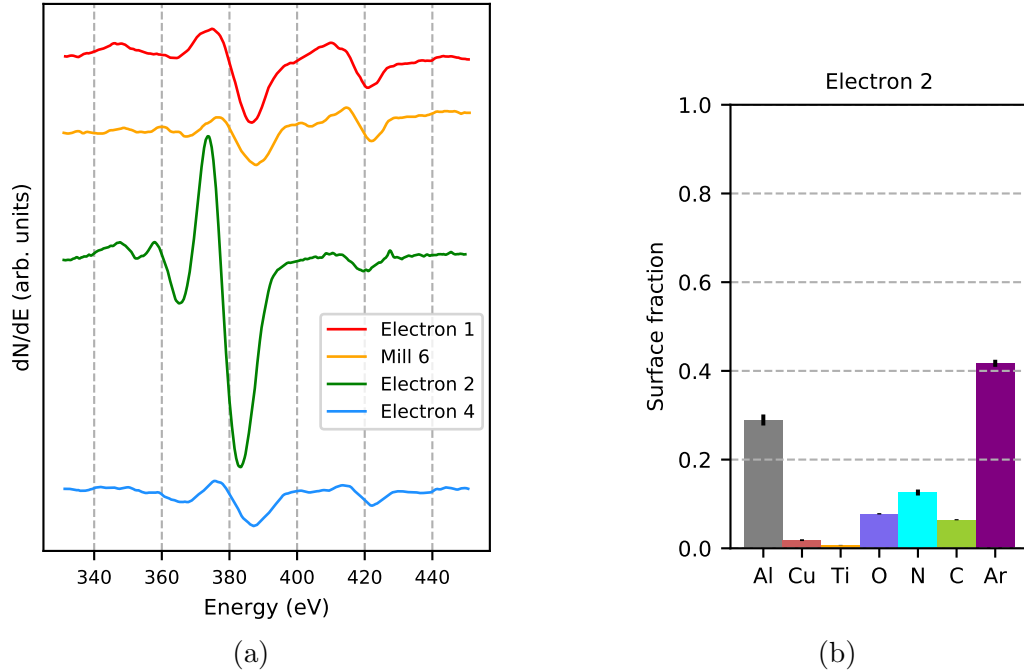


Figure 5.11: (a) Spectra of nitrogen and titanium measured throughout our surface treatment experiments. For the full context of these measurements, refer to [Electron 1](#), [Auger Mill 6](#), [Electron 2](#), and [Electron 4](#) in Chapter 7. (b) Relative surface fractions from Electron 2 shows a large nitrogen fraction with low uncertainty.

In this dissertation, we sometimes plot Auger spectra that have been directly smoothed by a Savitzky–Golay filter. Examples of smoothed carbon and aluminum spectra are plotted in Figure 5.12. Smoothing is never done before fractional analysis.

The Auger spectra also contains information about the chemical state of the surface. In our discussion of titanium, we compared its line-shape to reference spectra and found that it is difficult to make a clear statement on its chemical state. However, the line-shapes of carbon and aluminum can be interpreted much more clearly. We will present reference spectra for these elements in later chapters as their chemical states become relevant.

Electron bombardment as a surface treatment

The electron beam from the Auger spectrometer can alter the chemical composition and physical structure of the trap surface. Figure 5.6 showed the size of the electron beam in relation to the trap electrodes. When the Auger spectrometer is performing as a surface treatment tool, the electron beam is centered on the ion trapping location. When our goal is to measure the surface composition without affecting the electric-field noise at the ion, we align the electron beam so that it hits the ground plane near the outer edges of the trap.

To determine the location of the electron beam, we direct the beam towards the trap, and measure the current passing from the electron beam through each of the 21 DC electrodes. We track these currents while adjusting the position of the trap until the beam is aligned to the desired location. To determine the total energy deposited during an electron bombard-

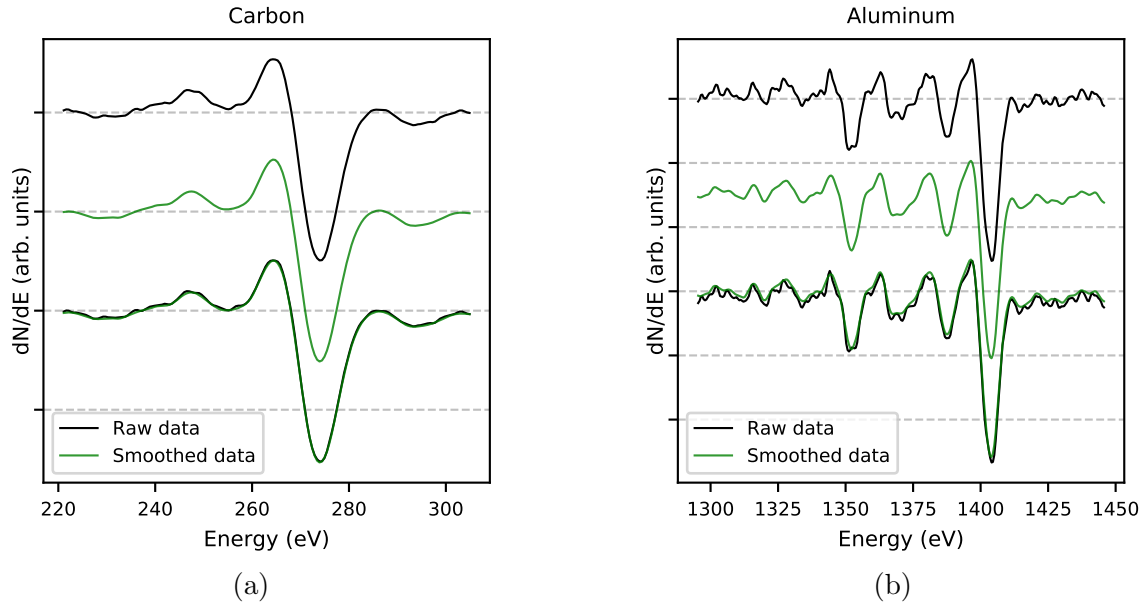


Figure 5.12: Examples of Auger spectra smoothed with a Savitzky–Golay. (a) Smoothed carbon spectrum. (b) Smoothed aluminum spectrum.

ment treatment, we first measure the current passing through the electrodes nearest to the ion trapping site. We estimate the surface area of the overlap between the electron beam and each electrode, and from this we can calculate the current density. The total energy deposited during an electron treatment can be calculated directly from the electron beam energy (2 keV), the current density, and the treatment time.

When the filament for the electron beam is turned on, the pressure in the chamber rises from $1\text{E-}9$ Torr to $1\text{E-}8$ Torr. We use a residual gas analyzer (ExTorr RGA model XT100M) to gain chemical information about the gasses in the chamber before and after the filament is turned on.

5.3 Argon ion milling

Ion-milling surface treatments are performed using an in-situ argon ion sputter gun. Before the treatment begins, the ion trap is shifted and rotated so that the beam will hit the trap at the desired angle and location. From measurements of individual electrodes, we estimate that the diameter of the ion beam is larger than the size of the ion trap chip. Next, the electron source in the ion gun is turned on, and the entire vacuum chamber is filled with argon gas. When argon diffuses into the gun, it is bombarded with electrons and becomes ionized. Ionized argon ions are accelerated toward the surface of the trap. We have performed milling treatments with ion energies of 200, 400 and 500 eV.

To prevent electrodes from shorting, the RF electrode is biased -2 V with respect to ground during ion milling, and the DC electrodes are biased +2 V with respect to ground. If a bridge of metal begins to form between differently-biased electrodes during the sputter process, a current will flow through the bridge and quickly burn it off.

While the milling process is underway, we continuously measure the amplitude of the current that passes through the DC electrodes as a consequence of argon-ion bombardment. We know the surface area of the combined DC electrodes, so we can calculate the current density of the argon treatment. With the argon ion energy, current density and treatment time the total deposited energy can be calculated.

The SRIM (the stopping range of ions in matter) simulation software [33] is used to estimate how much material is removed by each ion milling treatment. These estimates depend on the energy, mass and angle of the ion beam. They also depend on the atomic composition of the substrate, as different elements can have widely varying sputter rates. Our milling experiments were interspersed with Auger spectroscopy. We extrapolated between these surface composition measurements to find the appropriate surface compositions to input into the SRIM simulations.

5.4 Ion-trapping side effects

We deliberately alter the surface of an ion trap chip using heat treatments, electron bombardment, and argon ion milling. We have observed changes in ion heating rates in response to these treatments. There are also several ways in which the trap can be altered as a side effect of its operation as an ion trapping device. In our lab, teams have observed heating rate increases after RF current spikes, UV laser exposure, and calcium ion deposition. In addition, our titanium sublimation pump may deposit titanium onto the surface of the trap.

We take measures to avoid these side effects, and we have not found them to have any effect on ion heating rates in our system. The neutral calcium beam, as previously discussed, is angled upward to avoid depositing calcium onto the trap surface. The titanium sublimation pump is similarly angled. All lasers are angled parallel to the trap surface to prevent UV-induced surface reactions. The RF power is continuously monitored, and we have never observed any spiking behaviors.

Chapter 6

Thermally activated fluctuators

The surface of a typical ion trap is far too complicated to simulate fully from first principles. Trap surfaces have multiple length-scales of surface roughness, a variety of atomic species in different chemical configurations, and complicated crystal grain structures. In the absence of first-principle simulations, the thermally activated fluctuator (TAF) model is a powerful tool, as it provides an accessible way to investigate how a physical system generates electric-field noise.

The TAF model was developed by P. Dutta, P. Dimon, and P. M. Horn to describe 1/f noise processes in metals [34]. In 2018, our team found evidence that this model is relevant to studies of electric-field noise in ion traps. A detailed overview of the TAF model in the context of ion trapping can be found in reference [4]. This reference presents early data from the trap referred to as TRAP C in this dissertation, analyzed through the lens of the TAF model. It also includes a discussion of why we ruled out, for this trap, other noise models that have been previously proposed to describe ion-trap surface noise.

In this chapter we will present the mathematical framework of the TAF model. Then, we will demonstrate that the data taken in TRAP C throughout a series of surface treatment experiments can be described by an ensemble of TAFs with a distribution of energy barriers. Finally, we explore physical processes that are known to take place in metals, have dynamics that are consistent with the TAF model, and can generate electric-field noise.

6.1 Mathematical framework

A single two-level fluctuator can inhabit one of two possible states at any given time. To change between these states, the fluctuator must pass over a static energy barrier with magnitude E_a . In the thermally-activated regime, jumps between states are thermally driven. We assume, for simplicity, that the two states are at the same energy level. These concepts are illustrated in Figure 6.1a.

A single fluctuator produces random telegraph noise with a Lorenzian spectrum centered at zero. As shown in Figure 6.1b, the magnitude and corner frequency of the noise spectrum are temperature dependent. If the noise of a fluctuator is measured at a single frequency as its temperature is varied, the measured noise amplitude will peak at the temperature at which the corner frequency Γ is equal to the measurement frequency ω . For this reason, Γ

is called the characteristic frequency of the fluctuator. The characteristic frequency depends on the substrate temperature T and energy barrier E_a according to the equation:

$$\Gamma = \frac{1}{\tau_0} e^{-E_a/k_B T}, \quad (6.1)$$

where τ_0 is a temperature-independent attempt time that depends on the physical embodiment of the fluctuator. We assume that $E_a \gg k_B T$, where k_B is the Boltzmann constant.

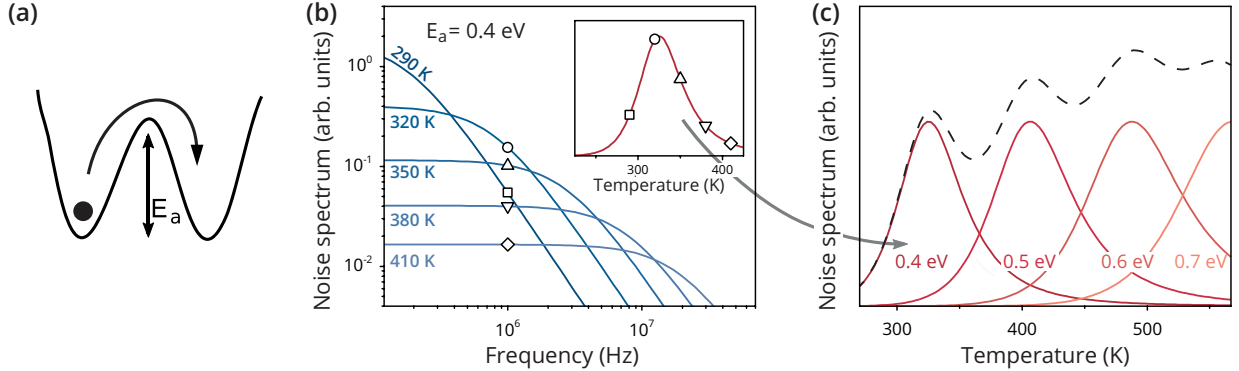


Figure 6.1: Illustration of TAF spectral properties. (a) Cartoon picture of a TAF showing a charge hopping between two potential wells separated by an energy barrier E_a . (b) Noise spectra for a single TAF with $E_a = 0.4$ eV at different temperatures. Inset: Temperature dependence of noise at a frequency of $2\pi \times 1$ MHz. Corresponding data points are displayed in the same shape. (c) Noise spectrum as a function of temperature for four TAFs (continuous curves) at $2\pi \times 1$ MHz. The dashed line shows the sum. (This figure and caption are reproduced from reference [4], and assume $\tau_0 = 10^{-13}$ s.)

In a macroscopic physical system such as a metal film, TAF noise is produced by an ensemble of fluctuators with a distribution of energy barriers. Noise from a sample distribution of fluctuators is plotted as a function of temperature in Figure 6.1c. If the distribution of TAF energies $D(E_a)$ is continuous and slowly-varying, we can make the approximation [34]:

$$S(\omega, T) \propto \frac{k_B T}{\omega} D(\bar{E}), \quad (6.2)$$

where S is the noise amplitude at measurement frequency ω and temperature T , and \bar{E} is the activation energy when $\Gamma = \omega$ for a given temperature.

This approximation can be used to extract a fluctuator distribution from measurements of noise at a range of different temperatures or frequencies. We use this capability to draw a concrete link between ion-heating-rate measurements and the physics of underlying noise processes. It is, however, important to recognize that a TAF distribution extracted from an ion-heating-rate temperature scaling may have smoother features than the true physical TAF distribution. This is due to the fact that even a TAF with an infinitely-precise activation energy produces smoothly-varying noise distributions in frequency in temperature space, as illustrated in Figure 6.1c.

6.2 Fit to ion-heating-rate data

The TAF model does not predict a functional form for how noise from a generic distribution of fluctuators should scale with temperature. Instead, it establishes that there is a very specific relationship between the temperature scaling and frequency scaling of TAF noise.

TAF noise scales inversely with frequency according to the equation:

$$S(\omega) \propto 1/\omega^\alpha \quad (6.3)$$

where α is the frequency scaling exponent, and the measurement frequency ω is equal to the secular frequency of the ion. In Chapter 4, we presented experimental evidence that noise in TRAP C follows this scaling behavior.

The TAF model predicts that α will depend on the slope of the temperature scaling according to the following equation [34]:

$$\alpha(\omega, T) = 1 - \frac{1}{\ln \omega \tau_0} \left(\frac{\partial \ln S}{\partial \ln T} - 1 \right). \quad (6.4)$$

To test this prediction in our system, we measure electric-field noise as a function of temperature at two frequencies. Then, we fit a Gaussian to each temperature scaling to obtain noise distributions with smoothly-varying slopes. The choice to use a Gaussian fit is not a statement about the underlying physics. It is simply versatile enough to fit the temperature scalings that we measure.

Before the smoothed heating-rate temperature scaling can be used to make a prediction of how α scales with temperature, a value must be chosen for attempt time τ_0 . In the context of defect dynamics in solid state systems, attempt times between 10^{-12} and 10^{-14} s have been used, as this is on the order of the inverse phonon frequency [35, 36, 37]. Attempt times on the same order have been used in the context of adatom diffusion on metal surfaces [38]. In contrast, Weckesser et. al. measured an attempt time of 10^{-10} s in a study of hydrocarbon diffusion on metals [39]. Figure 6.2 illustrates the impact that the choice of τ_0 has on the analysis of a temperature scaling measurement.

Figure 6.2a contains a plot of a heating-rate temperature scaling measured at a frequency of 0.88 MHz, along with a Gaussian fit line. This data was taken immediately after surface treatment MILL 7 & HEAT. The slope of the Gaussian fit from Figure 6.2a is inserted into Equation 6.4 to predict how frequency scaling exponent α will scale with temperature. Predictions made with two different choices of τ_0 are plotted in Figure 6.2b.

We measure α as a function of temperature by measuring heating rates at two or more frequencies between 0.5 and 2.0 MHz from room temperature to 575 K. The α values measured after treatment MILL 7 & HEAT are plotting in black in Figure 6.2b. To determine the accuracy of the TAF prediction, we do a reduced χ^2 analysis of this data, assuming that there is zero error in the TAF prediction lines. For the data and predictions plotted in Figure 6.2b using τ_0 values of 10^{-10} and 10^{-13} , the reduced χ^2 values are 1.16 and 0.89 respectively.

In Figure 6.2c are plotted two possible TAF distributions calculated directly from the temperature scaling in Figure 6.2a using two different attempt times. There are stark differences in the amplitudes and peak energies of these distributions. This illustrates that we must take great care in interpreting our extracted TAF distributions as we cannot measure τ_0 directly and must use values measured in other systems.

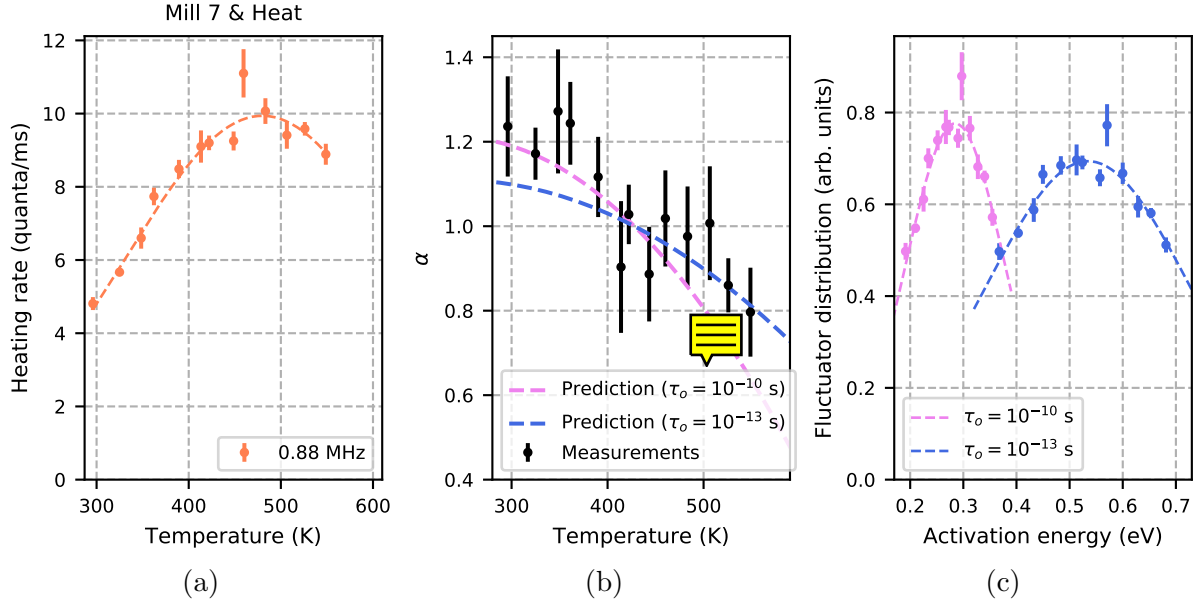


Figure 6.2: (a) Temperature scaling measured at 0.88 MHz with a Gaussian fit. (b) Measurements of the frequency scaling exponent as a function of temperature and predictions from the TAF model (Equation 6.4) using the slope of temperature scaling and two possible attempt time values. (c) TAF distributions calculated from the temperature scaling using two possible attempt times.

Figure 6.3a shows temperature scalings measured at two different frequencies after surface treatment MILL 1. As expected in a TAF system, the α predictions plotted in Figure 6.3b are the same for both temperature scalings, and match the measurements with a reduced χ^2 value of 1.52. The TAF distributions, as plotted in Figure 6.3c, are slightly offset in energy, and they match in regions where the energies overlap. Demonstrating that measurements at different frequencies probe the same underlying ensemble of TAFs is equivalent to demonstrating that the measured α values match the predicted values.

In Chapter 7 are plotted all of temperature scalings measured during TRAP C surface treatment experiments, scaled to a measurement frequency of 1 MHz assuming $\alpha = 1$. Also plotted are the corresponding TAF distributions, extracted from unscaled heating-rate measurements, assuming an attempt time of 10^{-13} s. In twenty of these data sets, temperature scalings were measured at two or more frequencies. The degree of overlap of TAF distributions extracted from temperature scalings measured at different frequencies gives a qualitative indication of how well each data set fits to the TAF model.

Before we do a quantitative assessment of how well the TAF model fits to the twenty-data-set collection, we must exclude certain measurements that we know to be outside of . First, we exclude data taken at the highest temperatures. At high temperatures, the heating rates abruptly increase in magnitude. The presence of this sharp feature is an indication that an entirely new noise source becomes activated at high temperatures. This new source does not appear to be consistent with TAF noise, and will be discussed in detail in Chapter ???. An example of a data set including the so-called *high temperature shoot-off* is plotted in Figure 6.4a, where excluded datapoints are marked with black x's.

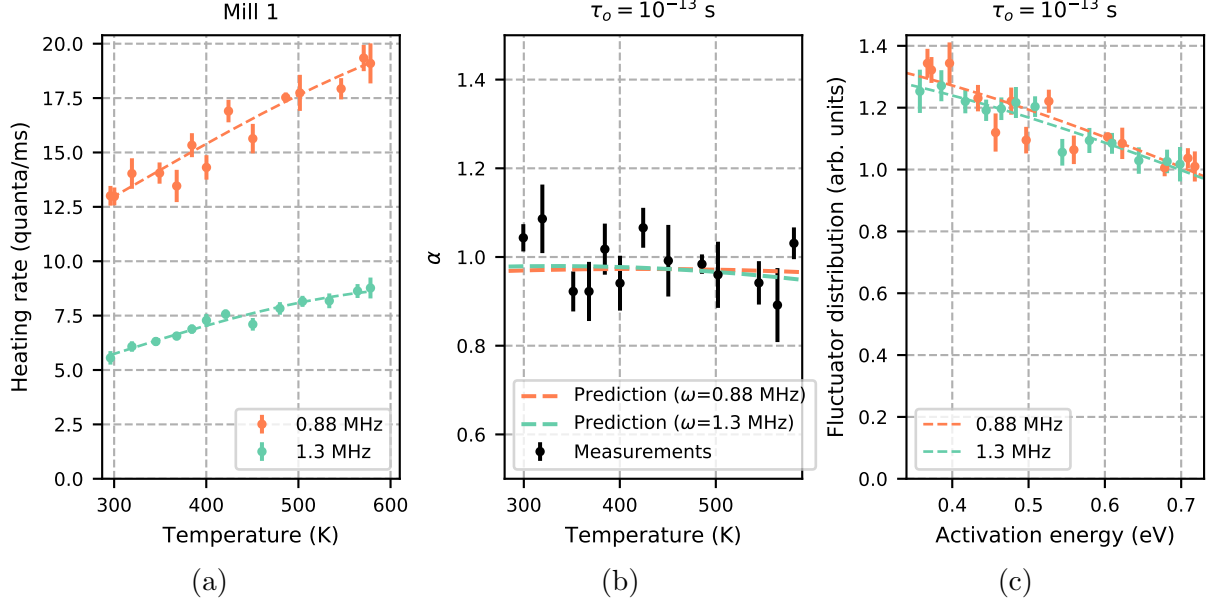


Figure 6.3: (a) Temperature scalings measured at two frequencies after treatment MILL 1, with Gaussian fit lines. (b) Measurements of the frequency scaling exponent and predictions from the TAF model (Equation 6.4) from each of the two temperature scalings. (c) A single TAF distribution measured at two frequencies.

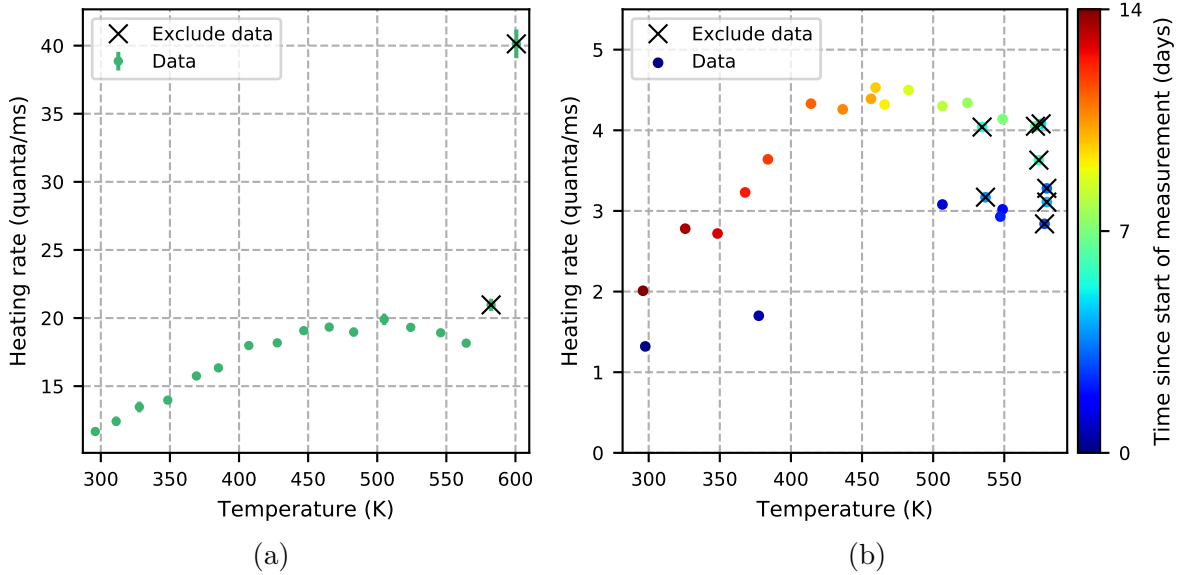


Figure 6.4: (a) Heating rates following treatment ELECTRON 1 scaled to 1 MHz, with data from the high-temperature shoot off excluded. (b) Heating rates measured at 1.3 MHz following treatment MILL 7, with data taken during an active thermal transformation excluded.

We also exclude measurements that were taken while the TAF distribution was undergoing a time-sensitive heat-induced transformation. Although noise during an active transformation may still be dominated by TAFs, temperature scaling slopes and frequency scaling

exponents lose physical significance when each measurement samples a different underlying TAF distribution. An example of a data set in which a thermal-induced transformation took place is plotted in Figure 6.4b. The choice of which data to exclude takes into account the temperature at which the transformation is activated, and the time it takes for the transformation to saturate, as will be discussed further in Chapter 9. Excluded datapoints are marked with black x's.

After high-temperature and transformation measurements have been excluded from a data set, we determine at which frequency the most measurements were taken. We then fit a Gaussian to those measurements to make a prediction of the temperature-dependence of α . Finally, we calculate a reduced χ^2 value to quantify how well the measured values of α match the prediction. This analysis was performed twice: once with an attempt time $\tau = 10^{-13}$ s, and once with $\tau = 10^{-10}$ s. Histograms including all reduced χ^2 values are shown in Figure 6.5.

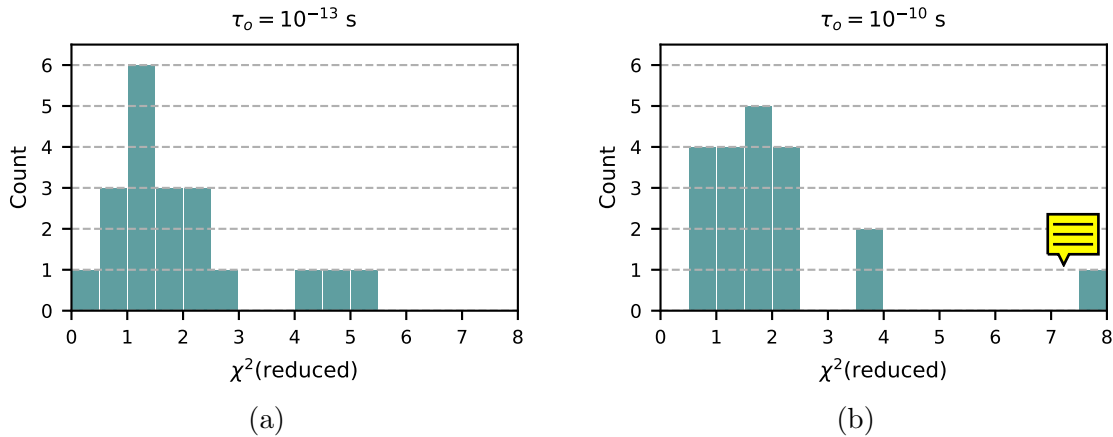


Figure 6.5: (a) Histogram of reduced χ^2 values calculated with attempt time $\tau_0 = 10^{-13}$ s.
(b) Histogram of reduced χ^2 values calculated with attempt time $\tau_0 = 10^{-10}$ s.

The majority of the reduced χ^2 values plotted in Figure 6.5 are low enough to conclude that these data sets are consistent with the TAF model. Data sets ELECTRON 1, MILL 5, and MILL 6 & HEAT have slightly higher values of reduced χ^2 , but are still reasonably low considering that we have not accounted for all sources of uncertainty.

For example, we assumed, for the purpose of these calculations, that the α predictions have zero uncertainty. This cannot be the case, as we have not measured the derivatives of the heating-rate temperature scalings with perfect accuracy. Errors in temperature scaling derivatives have a particularly significant impact on the data sets with the fewest heating-rate measurements, including MILL 5 and MILL 6 & HEAT. In addition, we have chosen specific values of τ_0 , and assumed that τ_0 is constant for all of the TAFs in a given distribution. This is not a good assumption in our system, as we likely have simultaneous noise contributions from multiple types of fluctuators. Measurements of α are further complicated by the possibility that thermally-driven TAF transformations took place without our knowledge.

6.3 The physical embodiment of TAFs

After having demonstrated that the noise in TRAP C is consistent with TAFs, we consider the physical embodiment of the fluctuators. Earlier we made approximations assuming that each fluctuator hops between exactly two states with equal energies, but these are not necessary requirements for physical TAFs. The TAF model requires only that the fluctuators are repeatedly thermally driven across energy barriers between stable states. For TAF electric-field noise specifically, these states must have distinct charge distributions.

With attempt times between 10^{-10} and 10^{-13} s, measurement frequencies between 0.7 and 2.0 MHz, and measurement temperatures between 300 and 600 K, we are sensitive to noise from TAFs between 0.2 and 0.7 eV. These energies and attempt times are consistent with atomic energy barriers associated with metal surfaces. There are several ways in which atomic and molecular fluctuators could produce electric-field noise. We will consider two possible categories of atomic fluctuators: migrating adsorbates, and near-surface defect motion.

In the category of migrating adsorbates, the physical fluctuators are adsorbates, and the TAF energies correspond to the surface migration barriers. Our previously discussed attempt times and energy barriers are realistic for hydrocarbon and adatom adsorbates diffusing on metal and oxide substrates [38, 40, 41, 39]. Molecular and atomic adsorbates bound to metal substrates have induced dipole moments, and these dipole moments depend both on the chemical structure of the adsorbate-metal bond and on the atomic-scale surface roughness of the substrate [42]. When an adsorbate hops between binding sites with different local curvatures, its interaction energy can fluctuate by an order of magnitude, leading to large fluctuations in its induced dipole moment [43]. These dipole fluctuations generate electric-field noise.

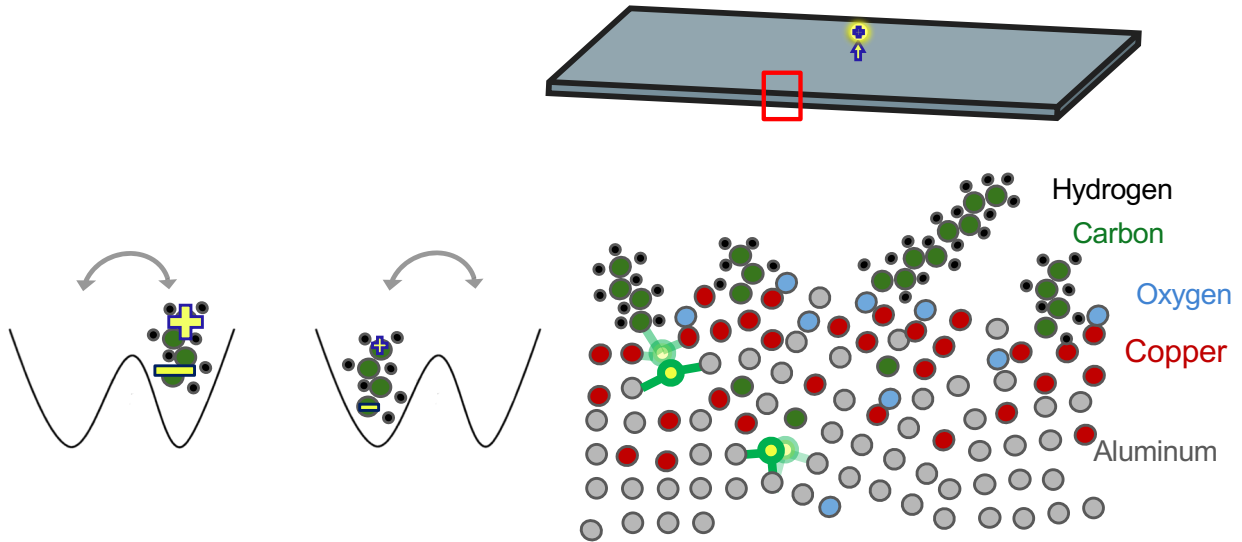


Figure 6.6: Left: cartoon of hydrocarbon dipole moment fluctuating in magnitude. Right: cartoon of trap cross section, illustrating metal defect fluctuations at and below the metal surface.

In the category of near-surface defect motion, the physical fluctuators are metal defects

and impurities, and the TAF energies correspond to the defect diffusion energies. An attempt time of 10^{-13} s and energy barriers between 0.4 and 1 eV are realistic for aluminum defect motion [36, 37, 35]. There is no charge associated with a point defect in an aluminum lattice, so a defect in isolation will not generate electric-field noise. A defect near the surface of a contaminated metal may activate dipole fluctuations in adsorbates, as the local curvature of the surface can fluctuate with the presence and absence of the vacancy. This process is illustrated in Figure 6.6,

Electric-field noise may also be produced by the motion of impurities in the bulk of the metal film. Impurities deep in the bulk will be shielded by the metal, but in a highly-contaminated surface layer the shielding will be suppressed. Unlike metal vacancy defects, impurities can have a charge associated with them. For example, an oxygen impurity atom will pull electrons from the metal bulk to fill its outer shell, and in doing so it will become doubly  charged. The motion of oxygen impurities, and other highly electronegative atoms such as nitrogen, can produce electric-field noise.

We can approximate the density of fluctuating dipoles required to produce the electric-field noise levels in our trap. The power spectral density of electric-field noise from averaged dipoles fluctuating parallel to the surface is given by [1]:

$$S_E = \frac{3\pi}{4\sigma_d} \frac{1}{(4\pi\epsilon_0 d^2)^2} S_\mu, \quad (6.5)$$

where σ_d is the dipole density by area, and d is the distance between the trapped ion and the surface of the metal. For fluctuators with a distribution of energy barriers $D(E_b)$,

$$S_\mu = \mu^2 \frac{\pi k_B T}{4\omega} D(E_b = -k_B T \log(\omega\tau_0)). \quad (6.6)$$

where μ corresponds to the difference between the dipole moments of the two fluctuator states. Dipole moments of adsorbed hydrocarbons, carbon atoms, and oxygen atoms on aluminum are approximately 1, 0.5, and 5 D respectively. As previously mentioned, these values can fluctuate by an order of magnitude if the adsorbate moves between binding sites with different local curvatures. If we assume that $D(E_b)$ is a Gaussian and that the dipole moment fluctuation $\mu = 5$ D, then $\sigma_d \approx 7 - 10 \times 10^{18} \text{ m}^{-2}$, or approximately 7-10 TAF dipoles per square nanometer. For comparison, a flat aluminum surface has about 12 surface atoms per square nanometer. Considering the high contamination levels measured in TRAP C before milling, and the likelihood that there are both surface adsorbate and sub-surface noise sources, these numbers are very reasonable. 

6.4 Summary

In this section, we introduced the mathematical framework of the TAF model and demonstrated that the temperature- and frequency-scaling data taken in TRAP C are consistent with this framework. We also discussed physical processes that may produce TAF electric-field noise in metal films such as ours, including fluctuating adsorbates and near-surface defects. The TAF model will be drawn upon throughout this dissertation to aid in the interpretation of how TRAP C responded to surface treatments.

Chapter 7

Timeline of data and surface treatments

This chapter includes all of the data taken and surface treatments executed on the ion trap that is the focus of this thesis - the trap that will be referred to in Chapter ?? as Trap C. This timeline establishes a naming and numbering system for all surface treatments (ex: Mill 2) and datasets (ex: Mill 2 heating rates). Most of this data will be re-presented one or more times in other chapters, and at those times they will be referred to with these names. The purpose of this system is to make it easy for the reader to determine the greater context of any given datapoint without complicating future chapters with bulky and repetitive explanations of the trap history.

Add a summary plot showing RT rates evolving over time. maybe high temp rates as well. Evenly space and label all treatments. Color code (purple, green, red)

Add info on background pressure, time, and current densities

First heating rates

Electron 1

Heat Electron 1

Mill 1

Heat Mill 1

Mill 2

Heat Mill 2

Mill 3

Heat Mill 3

Mill 4

Heat Mill 4

Mill 5

Heat Mill 5

Mill 6

Auger Mill 6

Heat Mill 6

Auger Heat Mill 6

Mill 7
 Auger Mill 7
 Heat Mill 7
 Auger Heat Mill 7
 Mill 8
 Heat Mill 8
 Mill 9
 Heat Mill 9
 Electron 2
 Heat Electron 2
 Mill 10
 Heat Mill 10
 Electron 3
 Heat Electron 3
 Mill 11
 Mill 12
 Auger Mill 12
 Heat Mill 12
 Electron 4
 Heat Electron 4
 Electron 5
 Heat Electron 5

Add full-range frequency scaling and justification for scaling everything to 1 MHz. Mention why we think we're surface-noise limited.

Table 7.1: Electron bombardment surface treatments

Treatment	Energy deposited (kJ/cm^2)	Treatment time (hr)	Carbon state	0.4 eV TAF amplitude change	0.7 eV TAF amplitude change
Electron 1	2	0.1	Graphite	up 30%	down 35%
Electron 2	76	3.0	Carbide	down 40%	down 30%
Electron 3	176	3.2	Carbide	0	up 20%
Electron 4	281	3.2	Carbide	0	up 25%
Electron 5	2130	23.0	Carbide	0	down 10%

Beam energy of all treatments = 2 keV

Current density = $3\text{ mA}/cm^2$ to $12\text{ mA}/cm^2$

In most cases, longer electron treatments deposit more carbon.

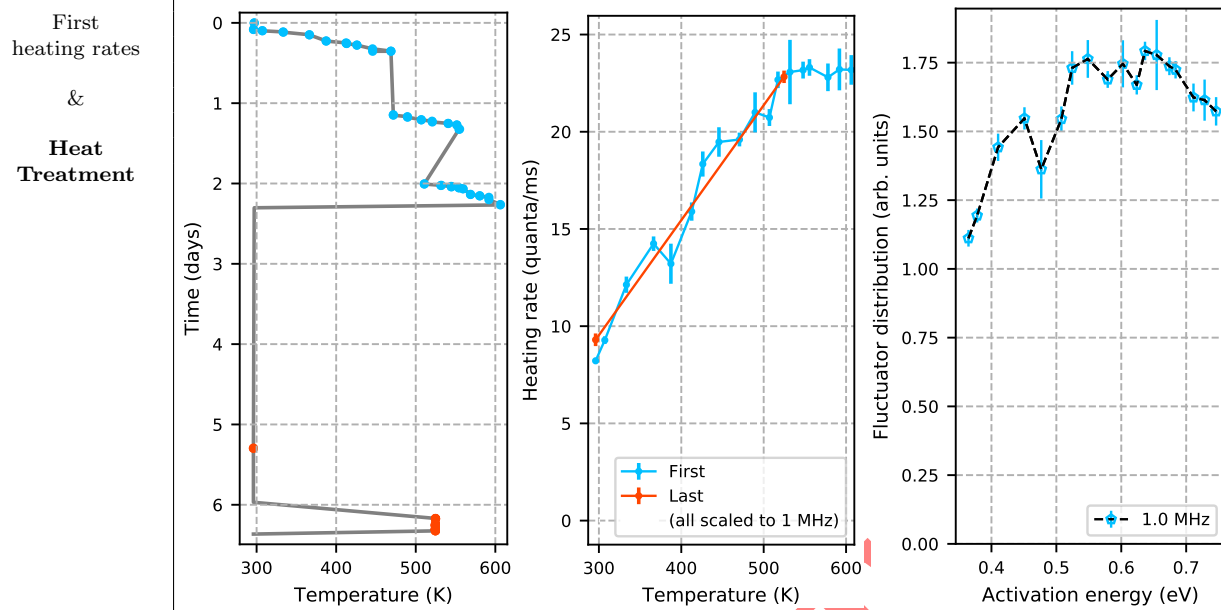
Table 7.2: Argon ion milling surface treatments

Treatment	Energy deposited (J/cm^2)	Material removed (nm)	Beam Angle	Beam Energy (eV)
Mill 1	0.1	0.13	normal	200
Mill 2	0.1	0.13	normal	200
Mill 3	0.5	0.6	normal	200
Mill 4	1.2	1.5	normal	200
Mill 5	2.9	3.9	normal	400
Mill 6	7.5	11.4	normal	400
Mill 7	8.8	16.4	normal	200
Mill 8	0.2	0.6	normal	200
Mill 9	0.6	1.3	normal	200
Mill 10	4.9	12.2	normal	200
Mill 11	9.7	18.9	45°	400
Mill 12	5.2	9.8	45°	500

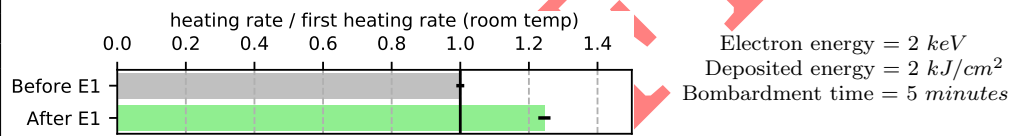
Current density = ? mA/cm² to ? mA/cm²

Argon pressure = ? Torr to ? Torr

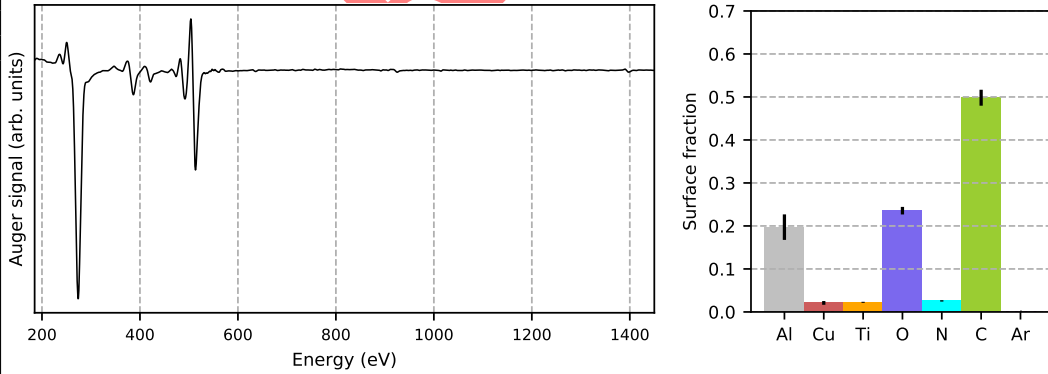
Table 7.3: Timeline of surface treatments and data

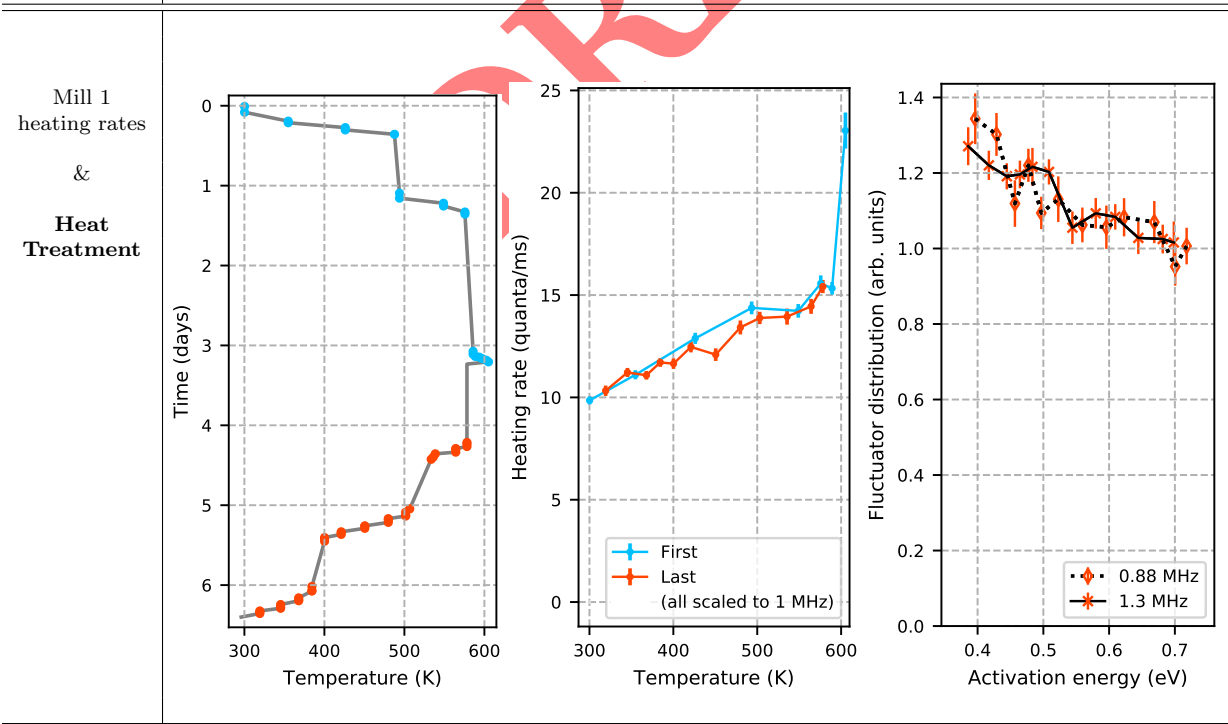
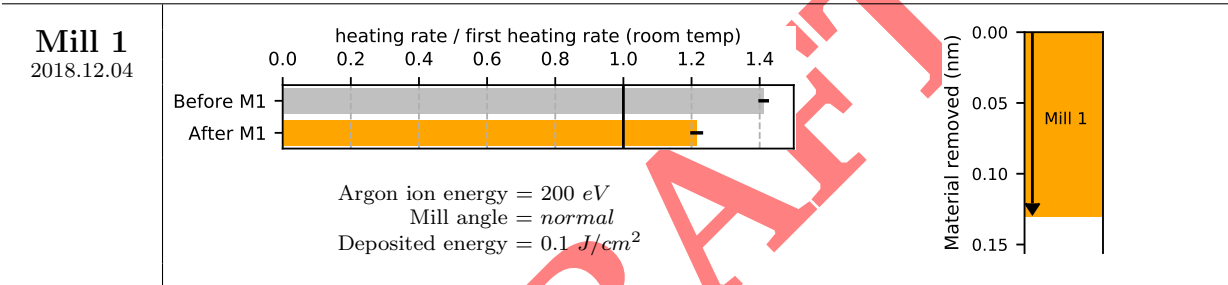
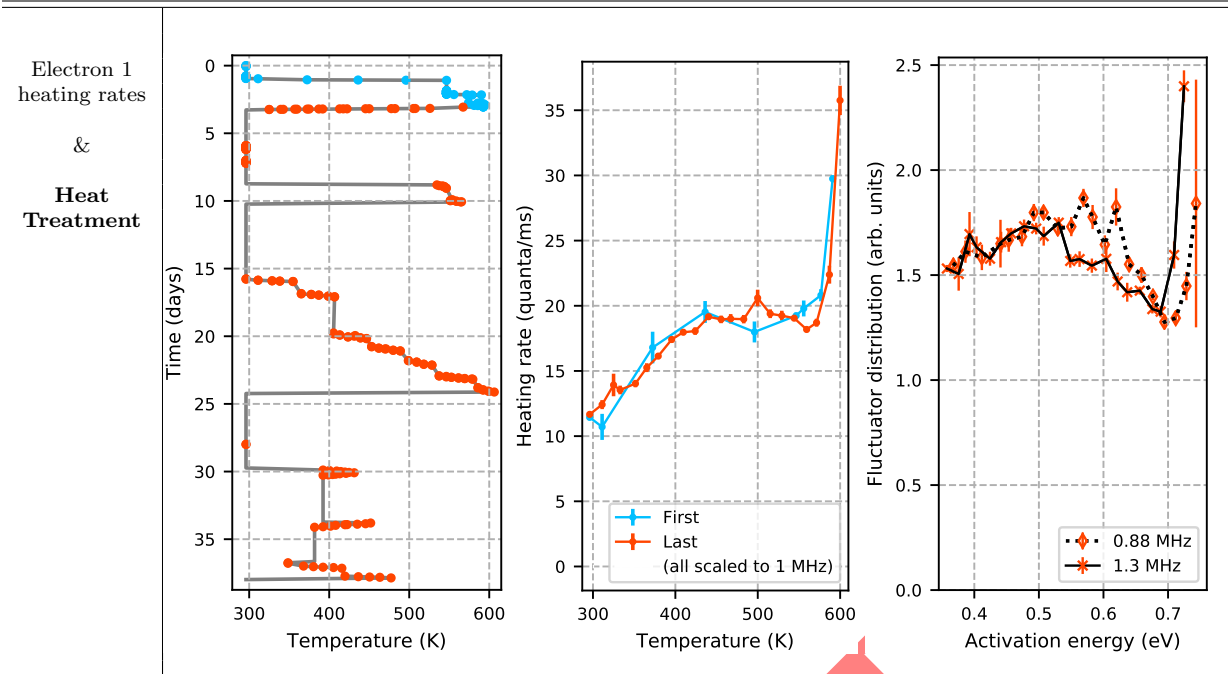


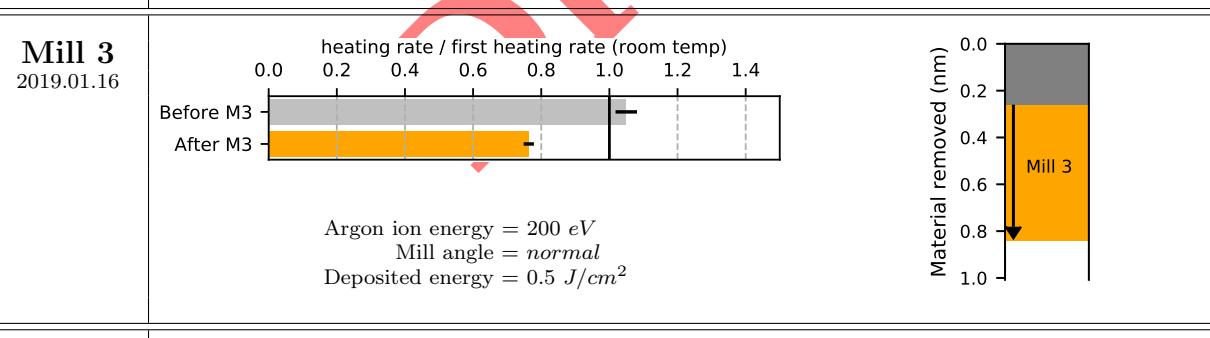
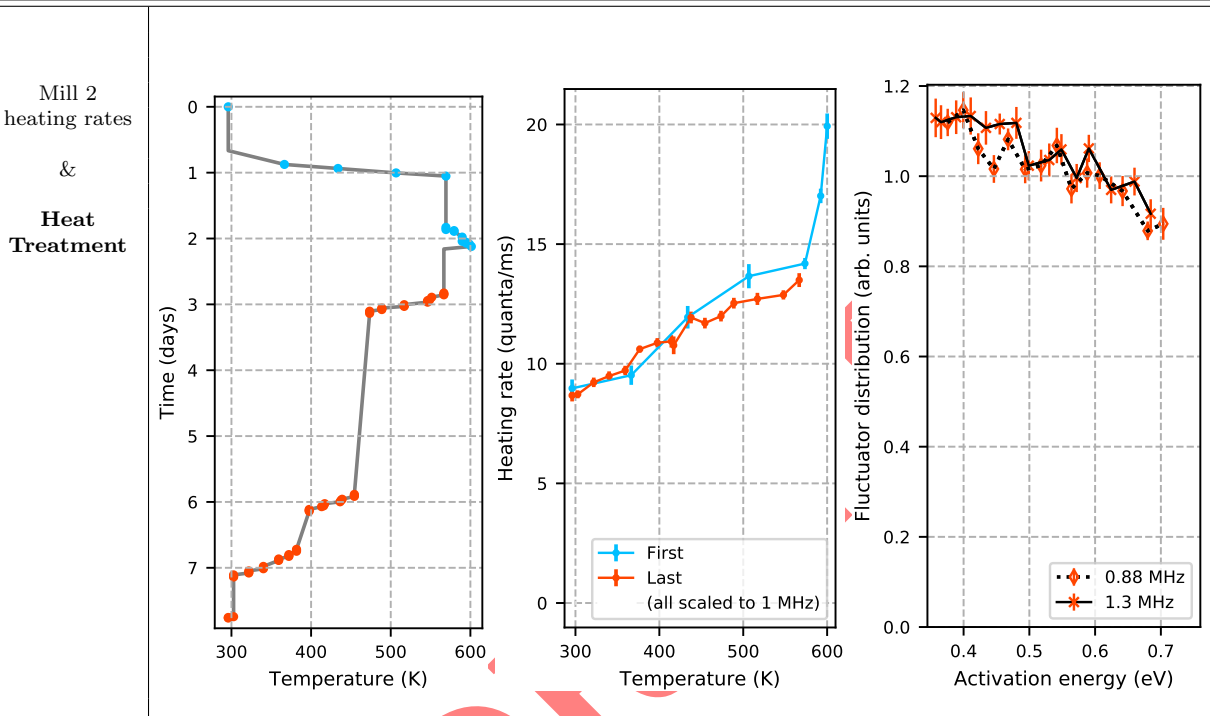
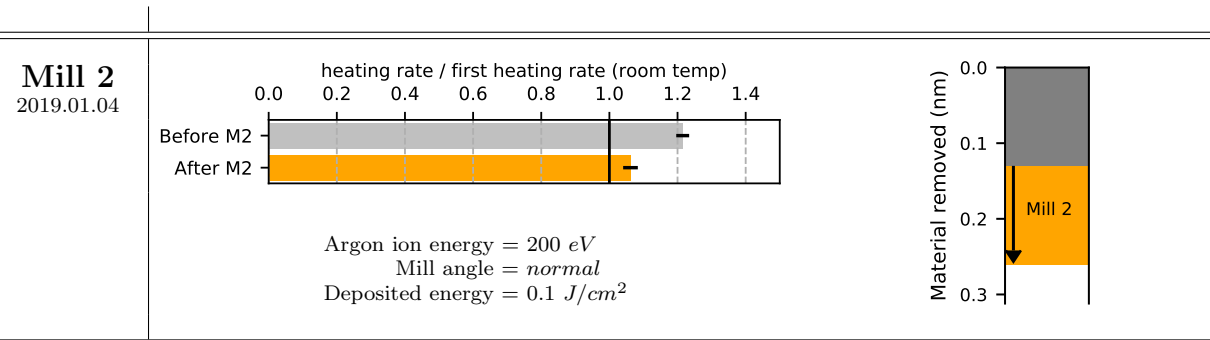
Electron 1
2018.06.22

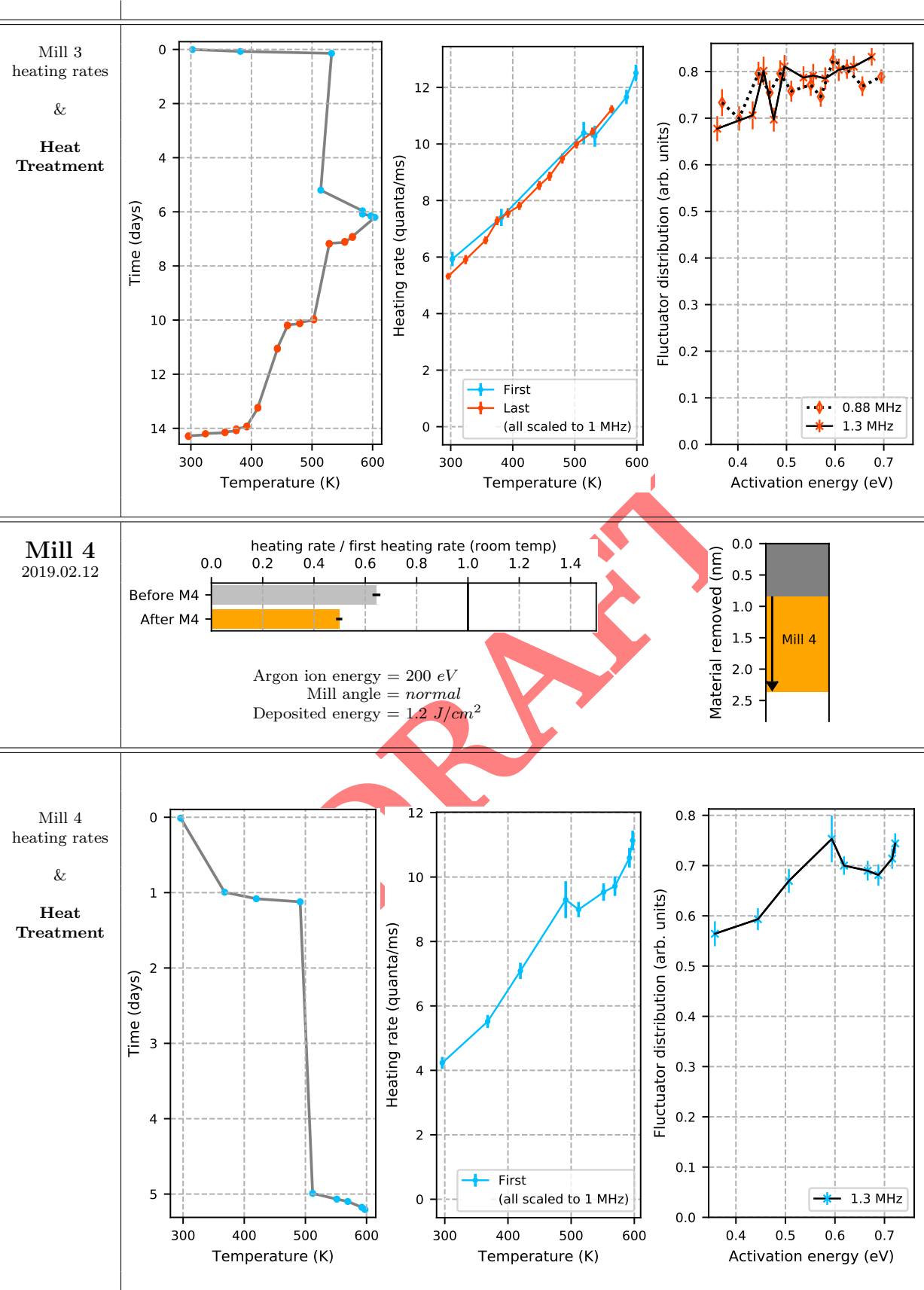


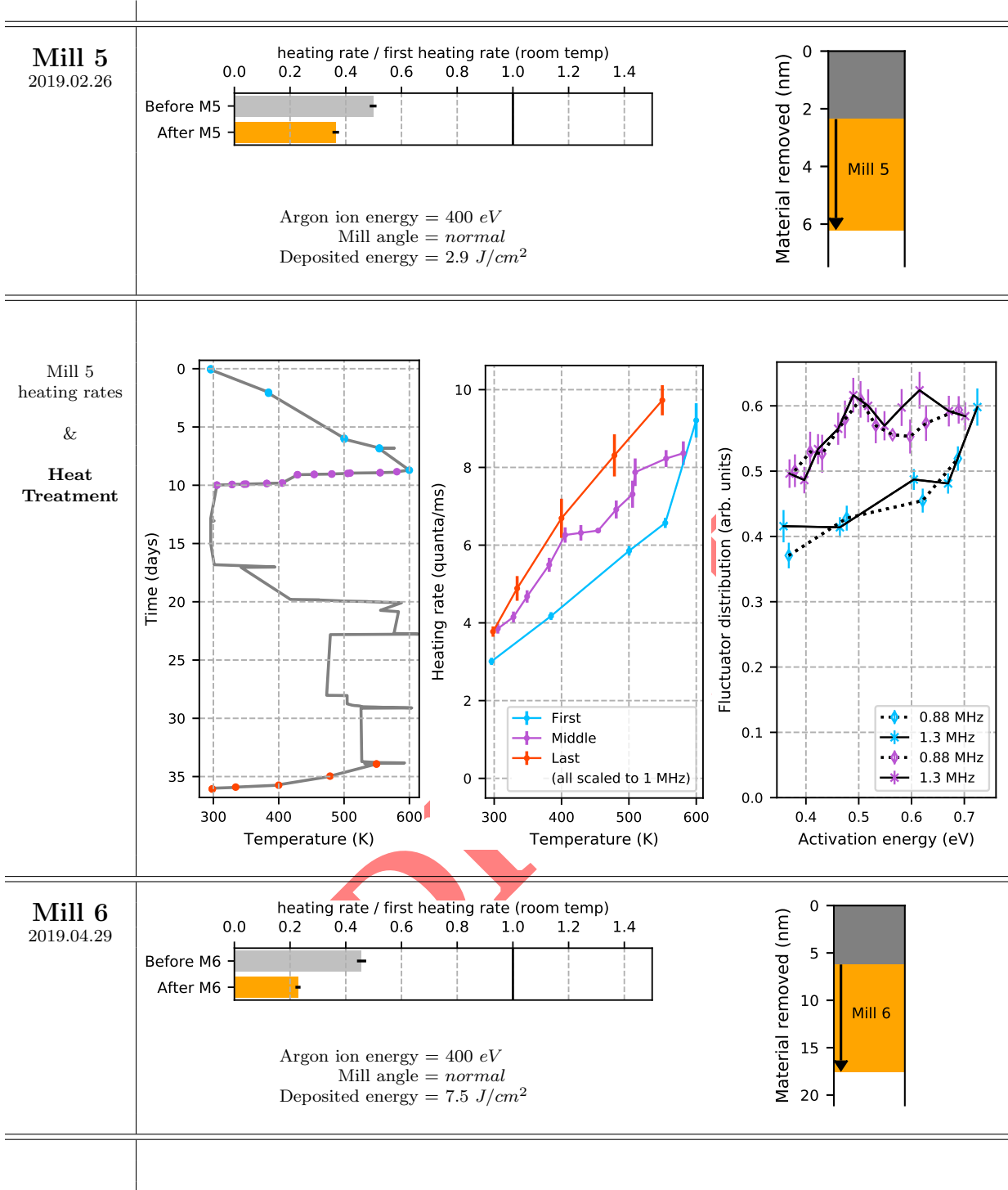
Electron 1
Auger spectrum

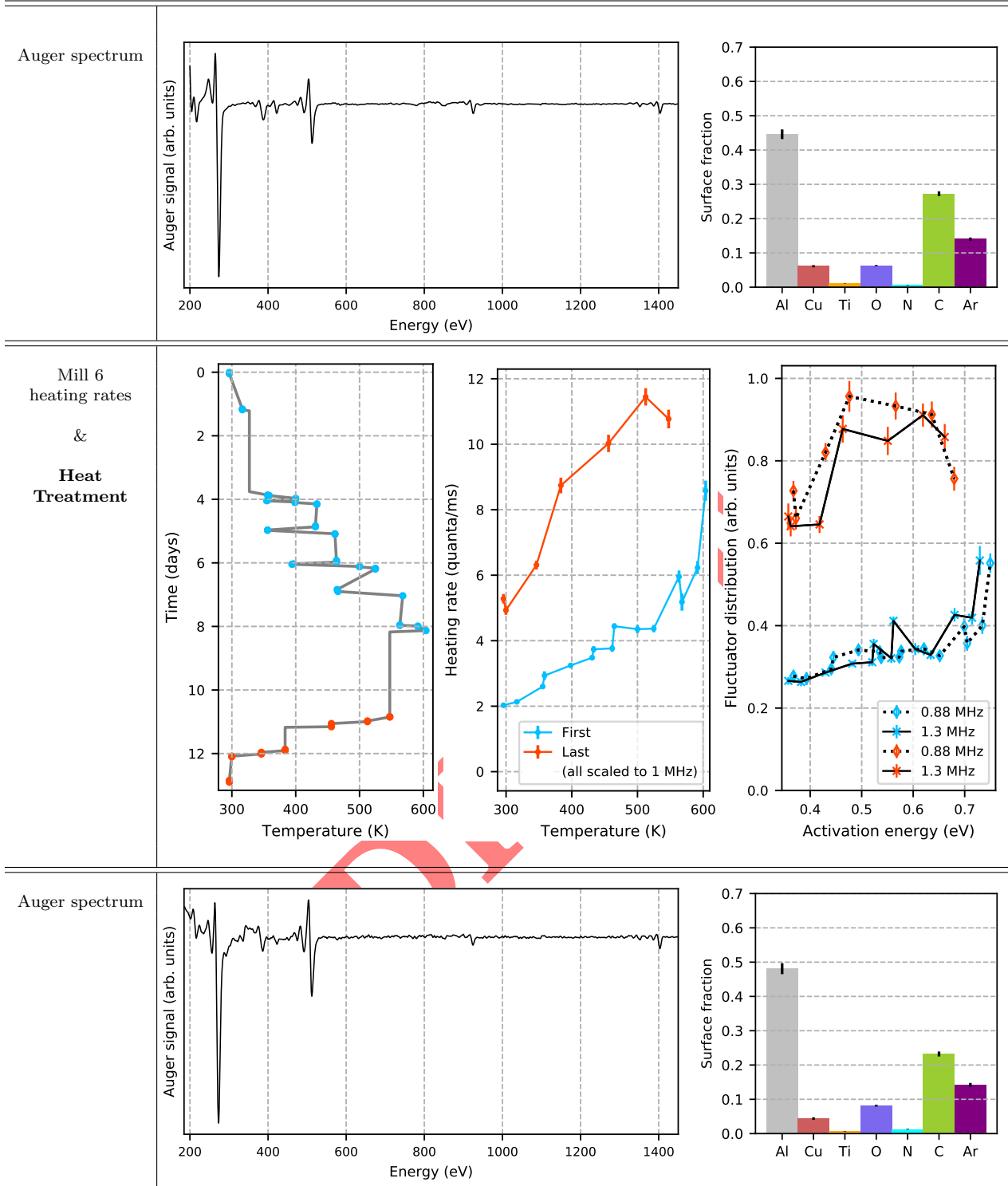


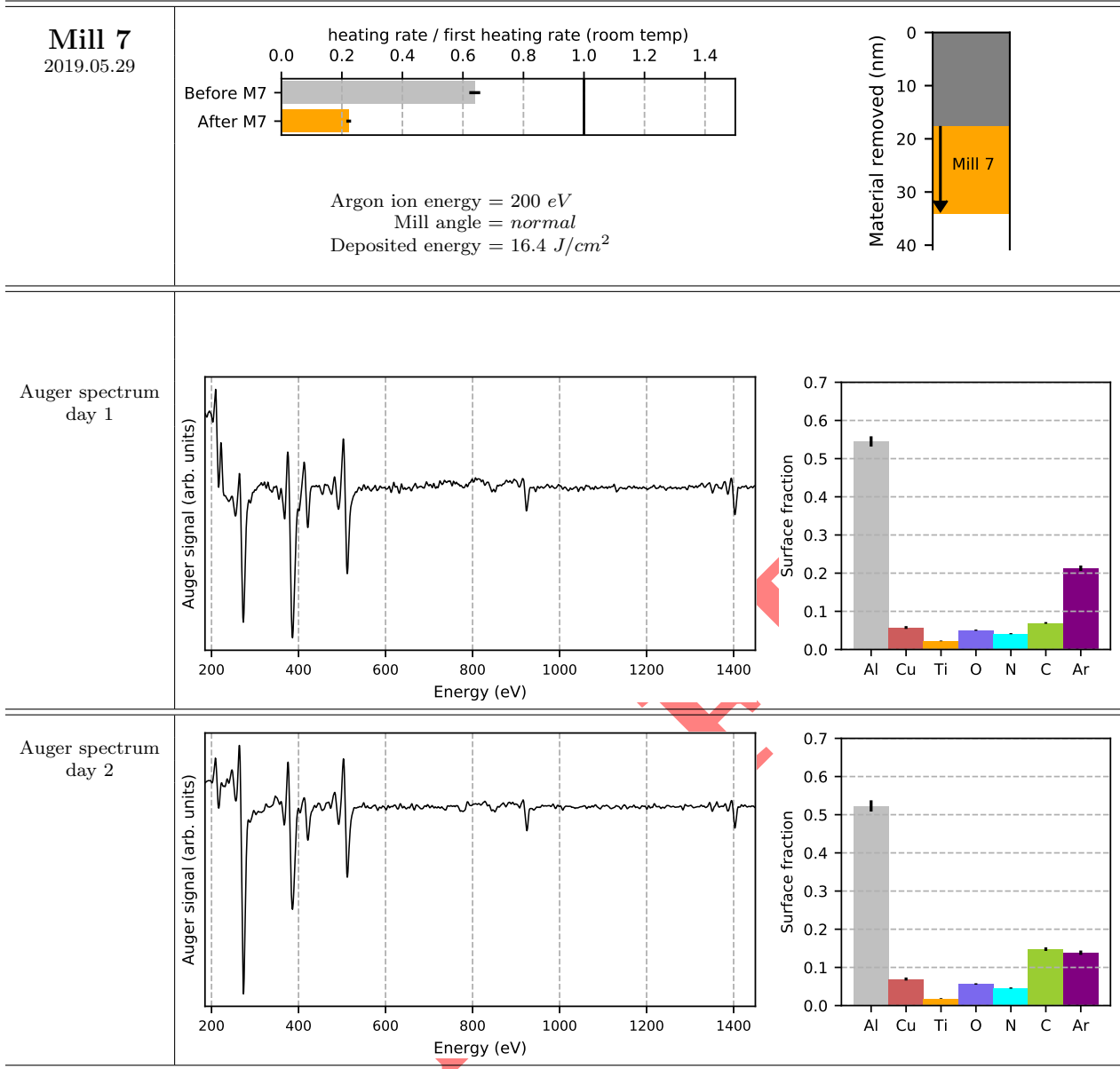


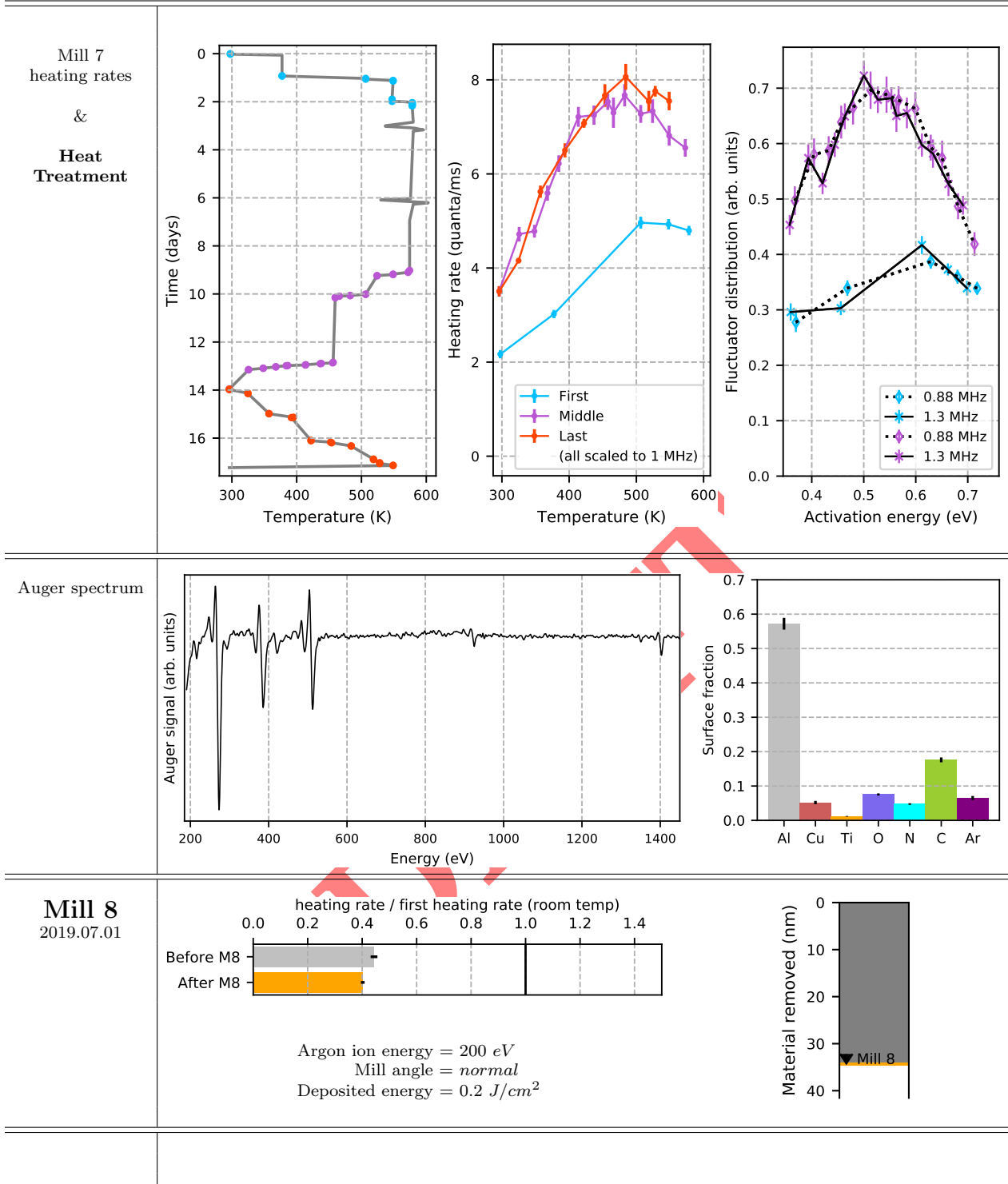


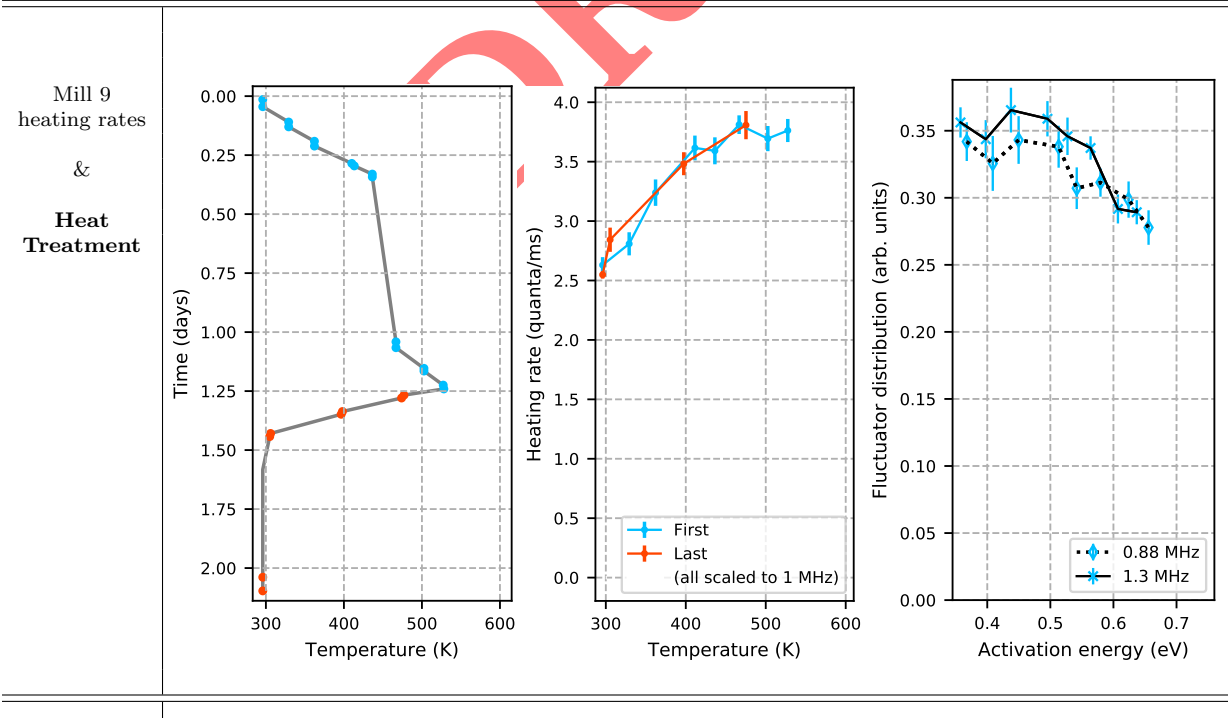
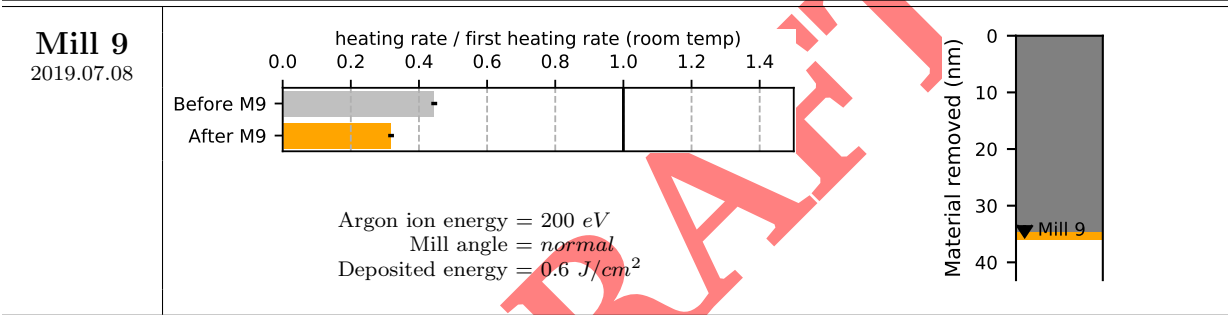
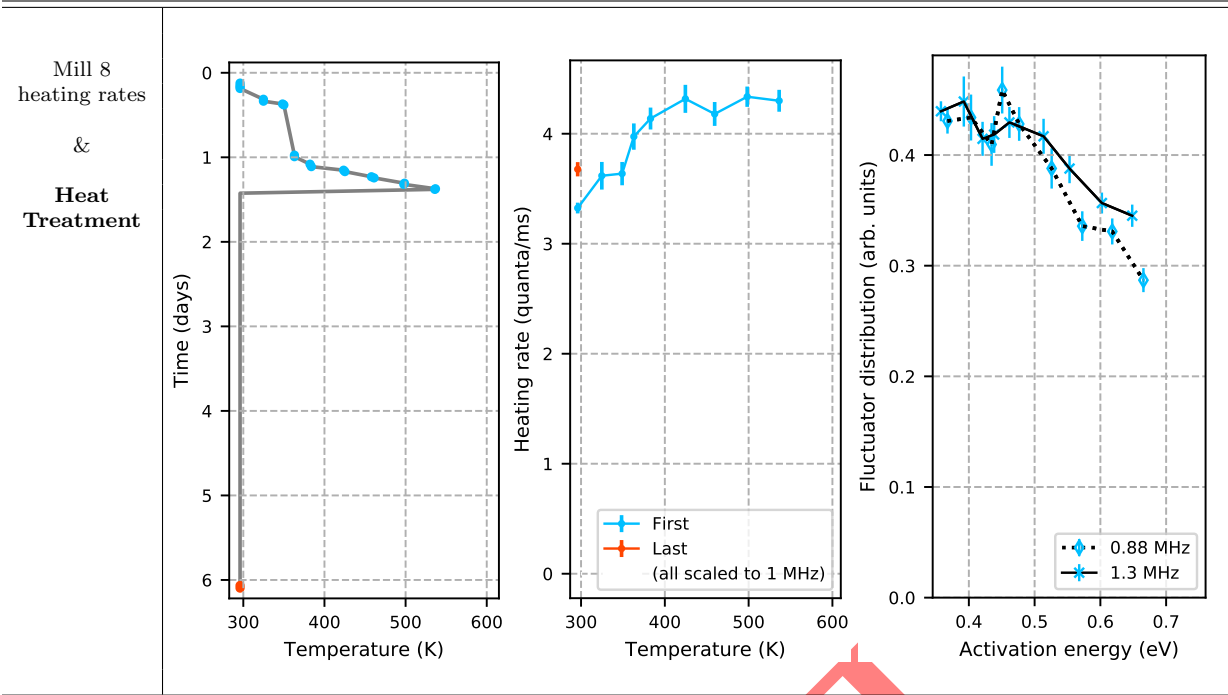




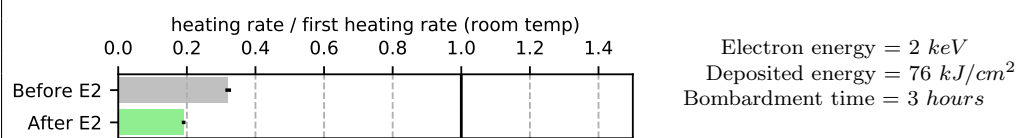




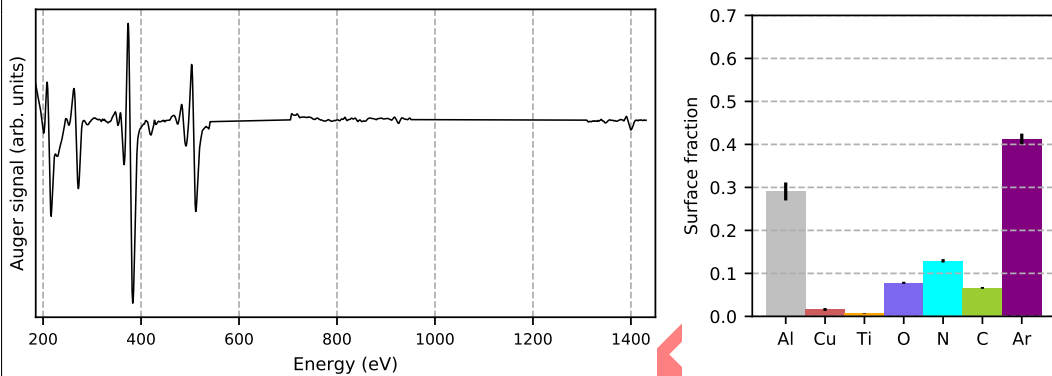




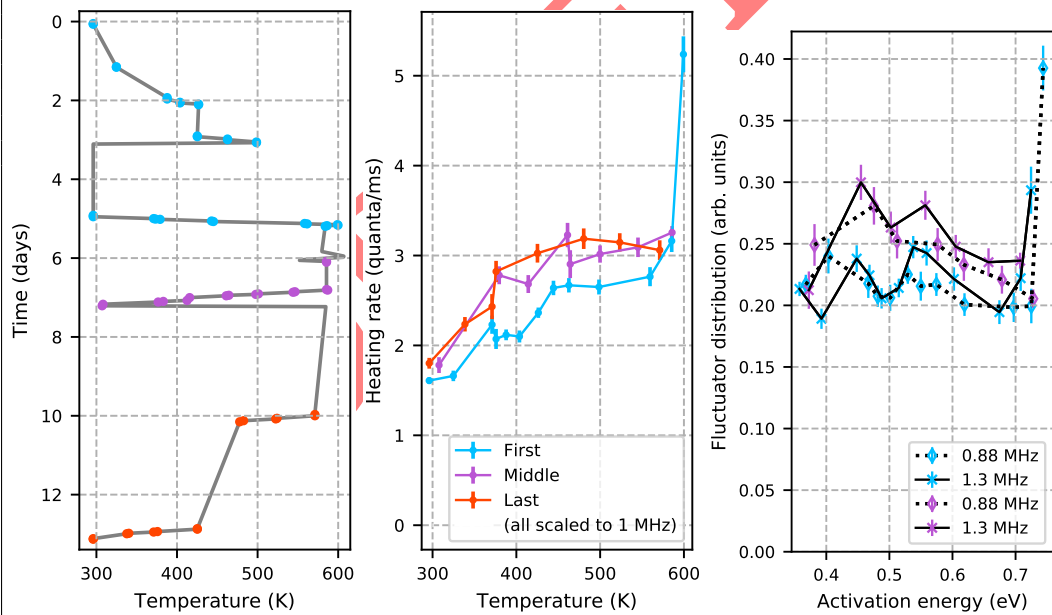
Electron 2
2019.07.15



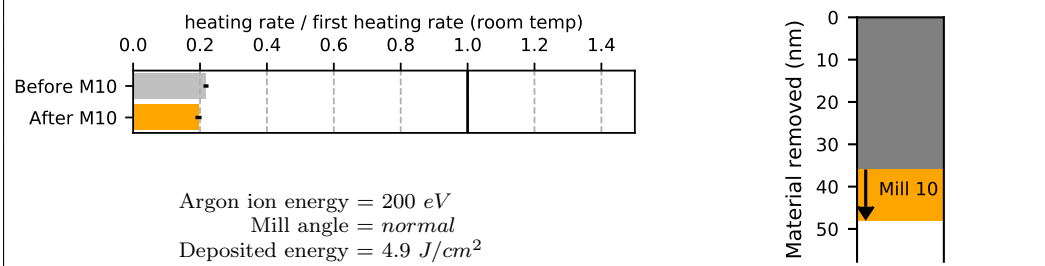
Electron 2
Auger spectrum



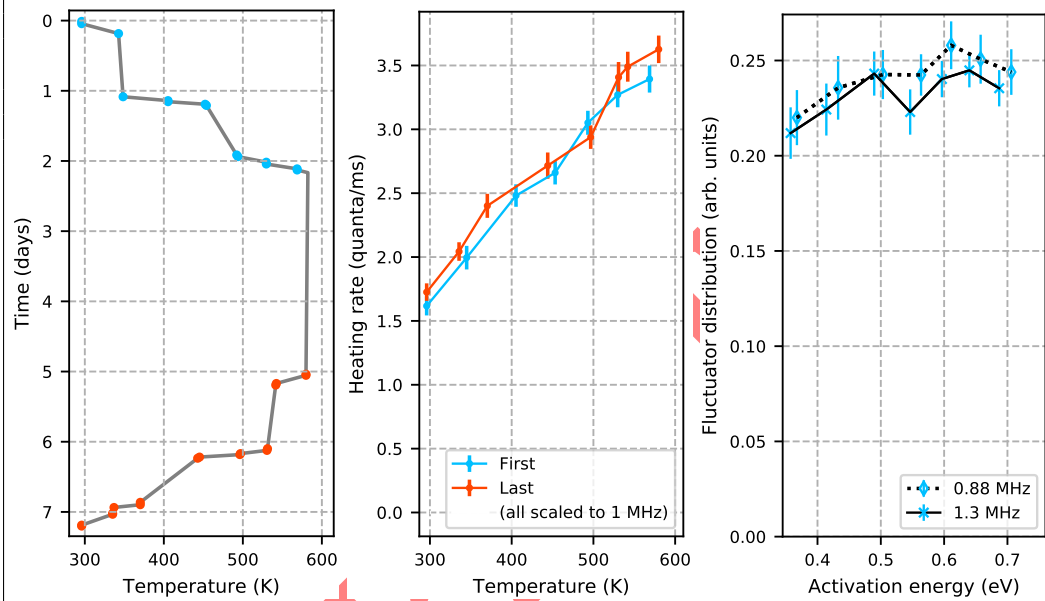
Electron 2
heating rates
&
Heat
Treatment



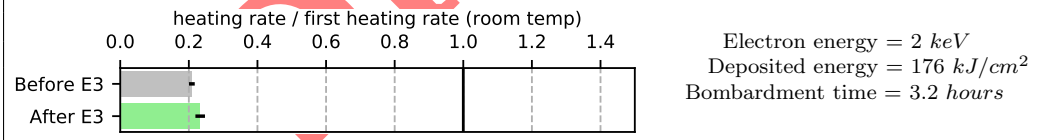
Mill 10
2019.07.30



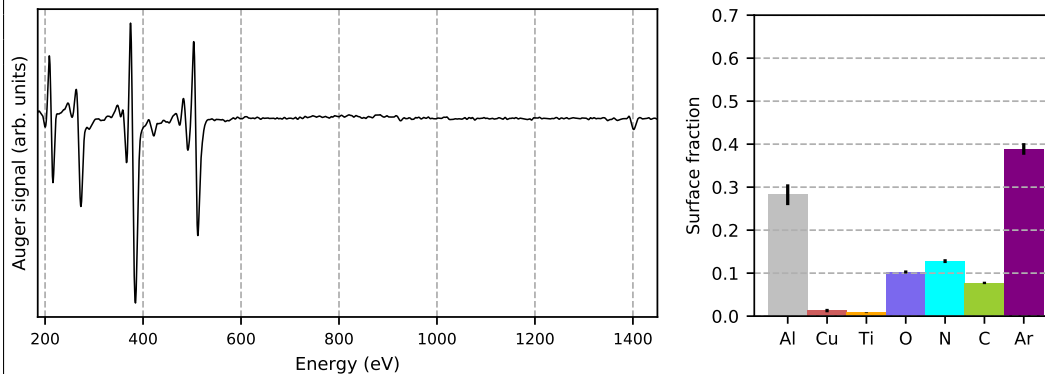
Mill 10
heating rates
&
Heat Treatment

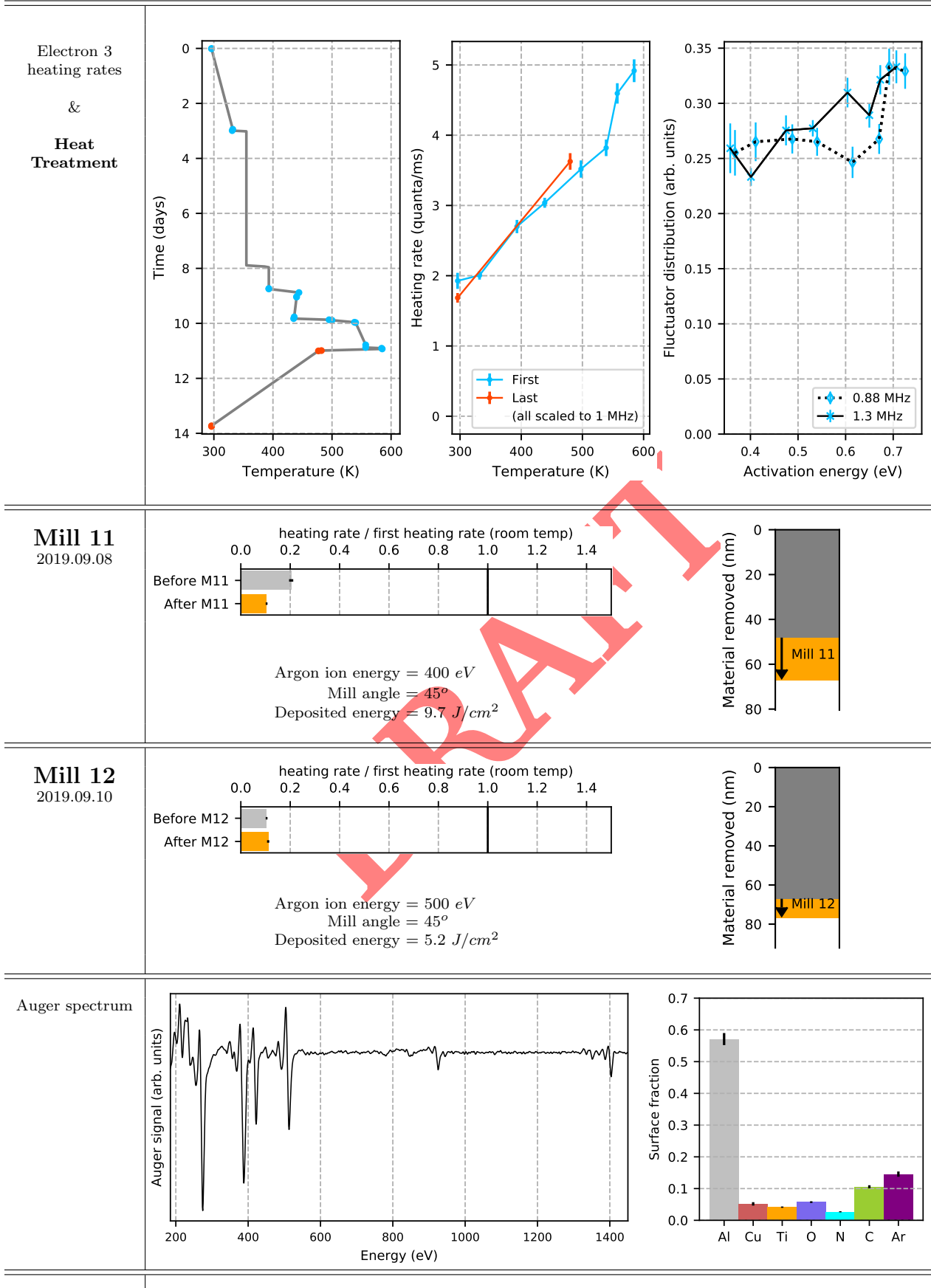


Electron 3
2019.08.13

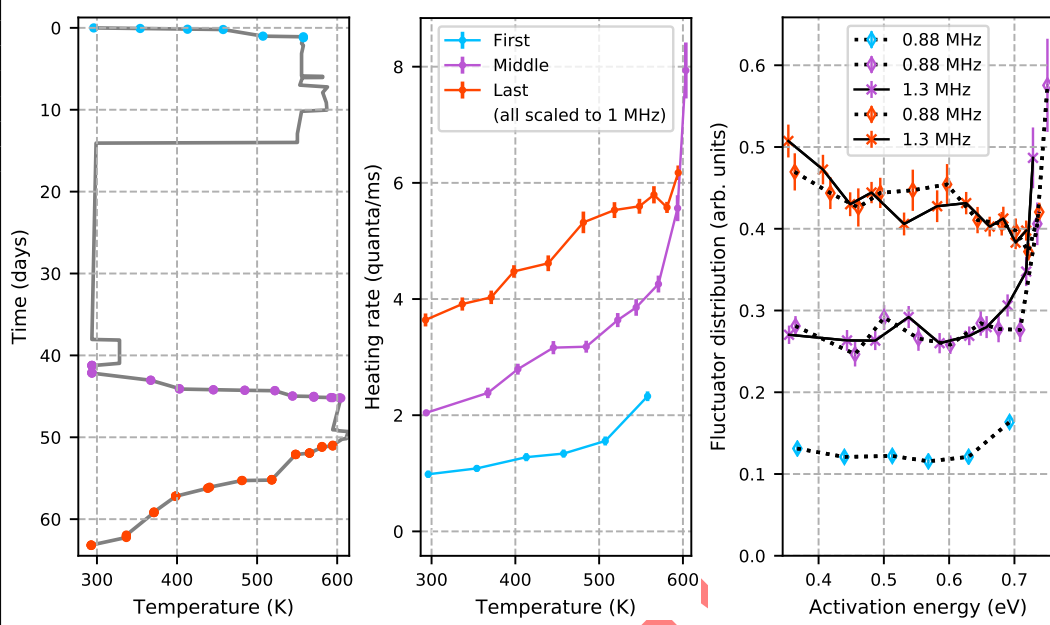


Electron 3
Auger spectrum

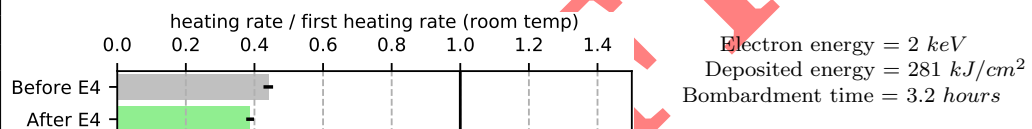




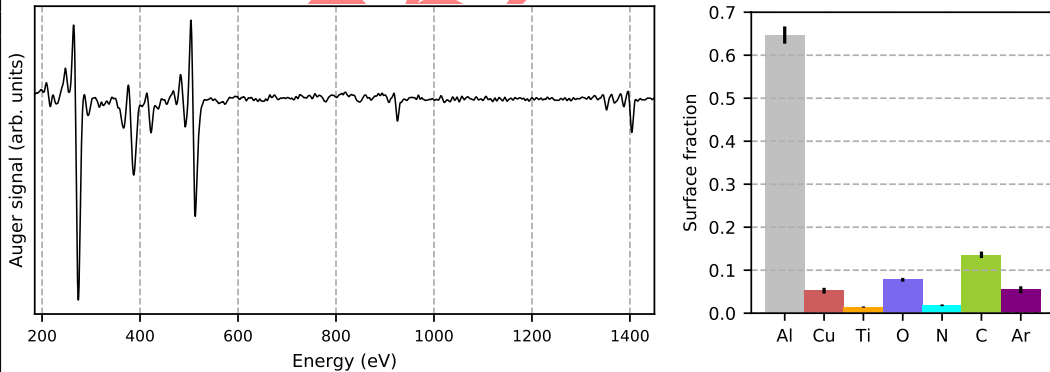
Mill 12
heating rates
&
Heat Treatment



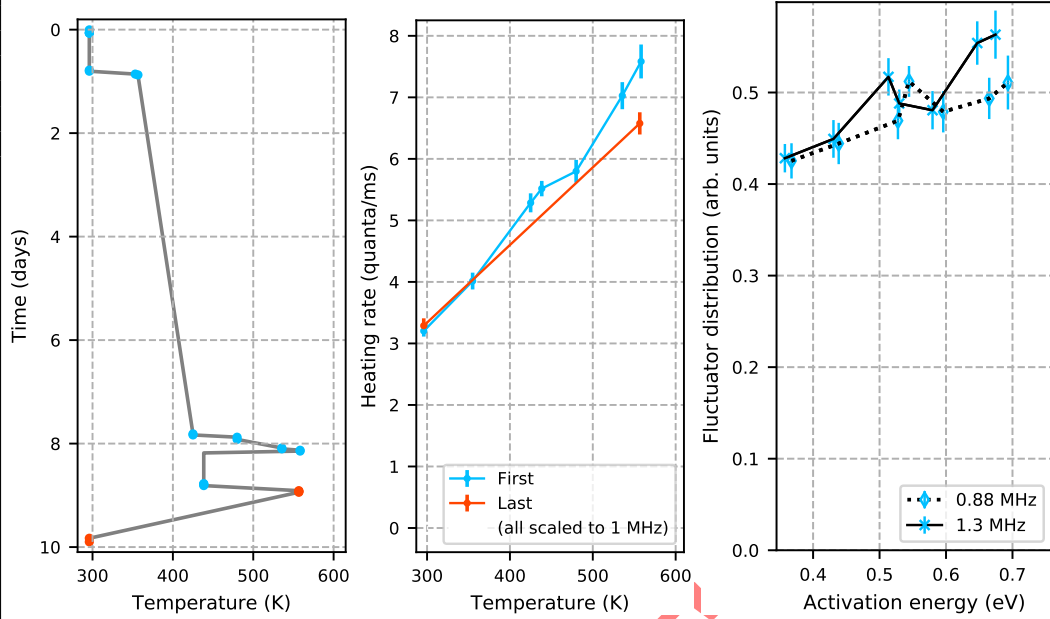
Electron 4
2019.12.06



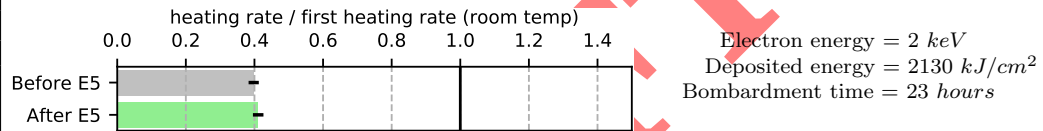
Electron 4 Auger spectrum



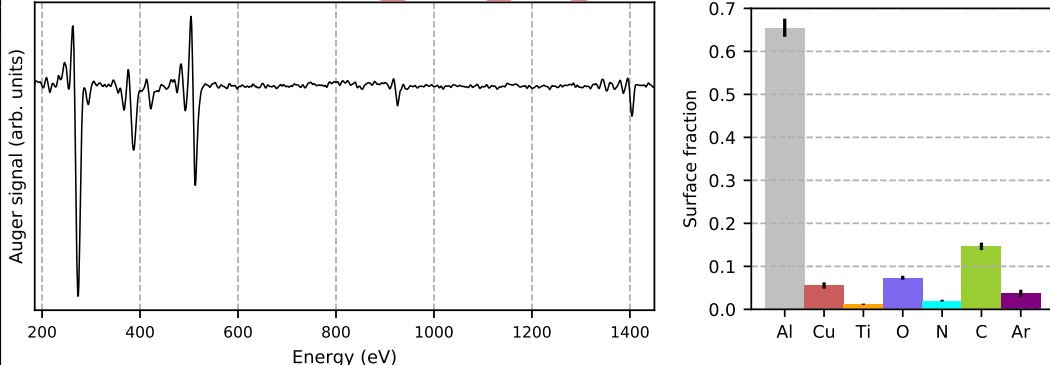
Electron 4
heating rates
&
**Heat
Treatment**



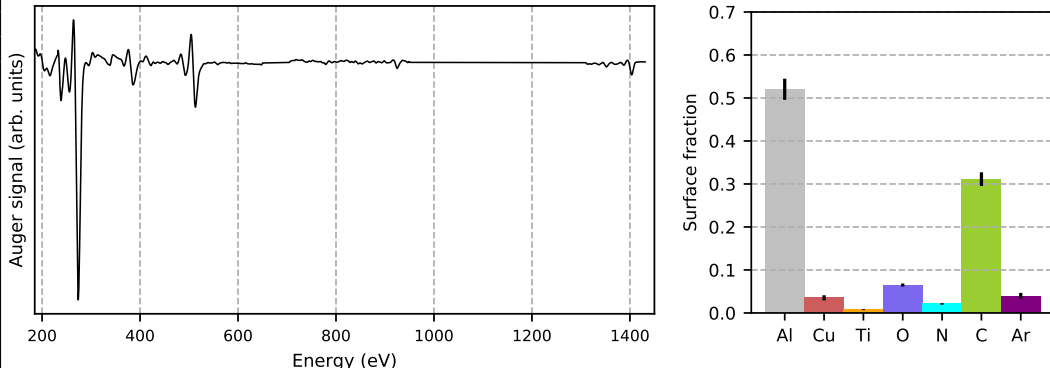
Electron 5
2019.12.19

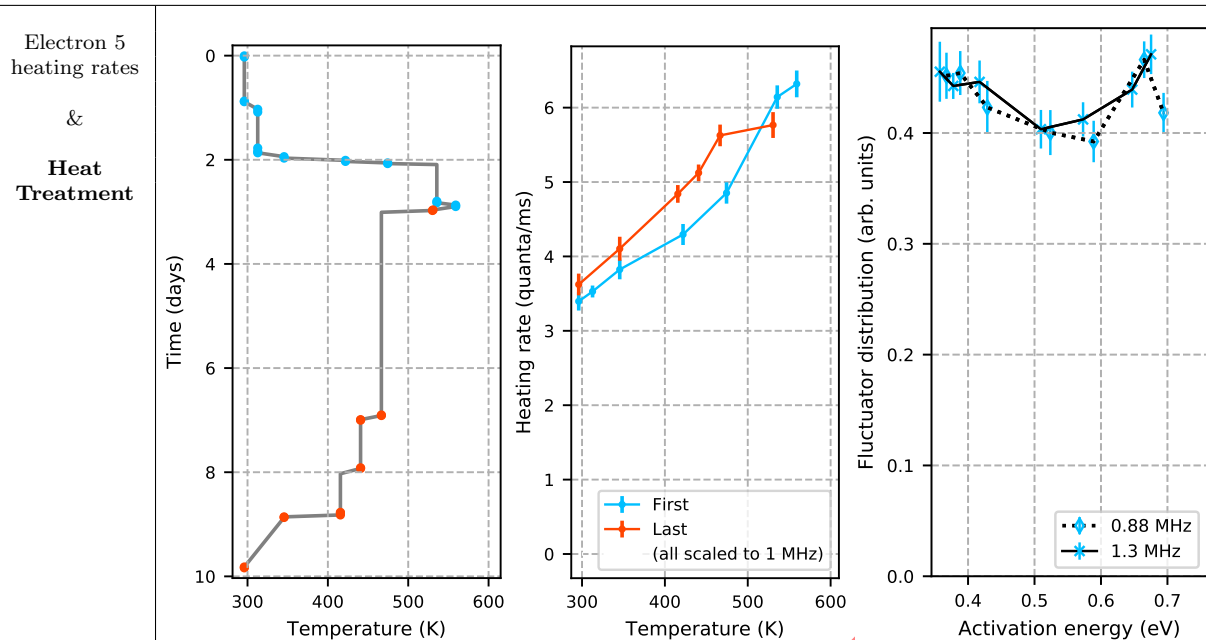


Electron 5
Auger spectrum
Day 1



Electron 5
Auger spectrum
Day 2





DRAFT

Chapter 8

Heating rates in different aluminum-copper traps

Ion traps throughout the world have produced a widely varying and unpredictable range of heating-rate measurements[1]. Researchers have experimented with different trap materials and surface treatments, but little attention has paid to how variations in the ion-trap handling and fabrication process affect the electric-field noise in a trap.

We compare three Al/Cu ion traps that were fabricated and operated by members of the Häffner lab. We find that the untreated Al/Cu traps have significantly different noise magnitudes, and that they also respond differently to surface treatments. We examine and compare these behaviors to determine their root causes in the fabrication and handling process. By doing so, we gain new insights into where the electric-field noise is coming from, and how the noise quality of an ion trap can be controlled.

8.1 Background on 4 Al/Cu traps

All of the measurements and surface treatments discussed in Chapters ??, 7, 10, 9 and ?? took place on a single ion-trap chip. In this chapter, the ion trap from those experiments will be referred to as Trap C. Trap B was fabricated with Trap C and operated in parallel in a second ion-trap experiment chamber. Trap A was fabricated and operated several years earlier than Traps B and C. Experiments of Trap A and Trap C took place in the same ion-trap experiment chamber with the same ion-milling gun, Faraday cage, auger spectrometer, and trap manipulator.

Traps A, B and C were fabricated using identical materials, methods and facilities. There are some differences in trap geometry, which are detailed in Table 8.1. All heating rates in this chapter were taken at room temperature. Heating rates have been scaled to 1 MHz trap frequency using the power law scaling:

$$\Gamma \propto f^{-2} \tag{8.1}$$

where Γ is the heating rate and f is the trap frequency. This frequency-scaling power law has been confirmed experimentally in Traps A, B and C. Heating rates have been scaled to

a $72 \mu\text{m}$ ion height using the power law scaling:

$$\Gamma \propto d^{-\beta} \quad (8.2)$$

where d is the ion height, and β is the distance-scaling exponent. β could not be measured in Trap A, where distance re-scaling is necessary. In other traps, β has been measured to be between 2.5[5] and 4[6]. If $\beta=4$, the Trap A pre-treatment 1 MHz heating rate scales to 0.54 ± 0.03 quanta/ms. If $\beta=2.5$, this heating rate scales to 0.33 ± 0.02 quanta/ms. From this, we know the correctly scaled heating rate is likely between .31 and .57 quanta/ms. The Trap A heating rates presented in Table 8.1 and on subsequent plots reflect this uncertainty.

Table 8.1: Ion trap comparison

Trap	Trench width x depth (μm)	Ion height (μm)	Ion trap chamber	Metal deposition date	Scaled heating rate (quanta / ms)	Reference with more details
Trap A	10 x 100	100	Häffner_1	2012	0.44 ± 0.13	[11]
Trap B	20 x 100	70	Häffner_2	2016.06.29	$0.79 \pm .05$	[44]
Trap C	20 x 50	72	Häffner_1	2016.06.29	$5.7 \pm 0.2^*$	Chapter ??

* Scaled initial heating rate

8.2 Linking fabrication process variations & heating-rate magnitudes

Fabrication and measurement details specific to Trap C can be found in Chapter ?. The basic procedure common to all traps is outlined here, followed by a discussion of which steps in the process may vary between traps, and how these variations may affect the electric-field noise.

Step 1: Pattern trenches into fused-silica chip
(performed by Translume, Ann Arbor, MI [22])

- Laser weakening
- Hydrofluoric acid etch

Step 2: Deposit metal onto surface of chip
(performed at Berkeley Marvell Nanolab, Class100 clean room)

- Pirahna bath removes organic contaminants
- Electron-beam evaporation, 45° to normal, pressure = 10^{-8} to 10^{-7} Torr
 - 15 nm Ti
 - 500 nm Al
 - 30 nm Cu
- Expose trap to atmosphere to manually rotate 180°

- Electron-beam evaporation, -45° to normal
 - 15 nm Ti
 - 500 nm Al
 - 30 nm Cu

Step 3: Package and store trap
(performed at Berkeley Marvell Nanolab, Class100 clean room)

- Mount trap & wirebond to chip carrier
- Store trap in atmosphere

Step 4: Install trap in vacuum
(performed at Häffner lab, UC Berkeley)

- Install chip carrier in vacuum chamber
- Bake vacuum chamber
 - Temperature = 160 to 180° C
 - Pressure during bake = 10^{-8} to 10^{-7} Torr

Step 5: Trap ions & take measurements
(performed at Häffner lab, UC Berkeley)

Step 6: If issues arrise with trapping or measurement: break vacuum, repair, & repeat Steps 3, 4 & 5

While there may be variations in **Step 1** that we are not aware of, all traps arrive at Berkeley with optically-smooth surfaces. In **Step 2**, the pirahna bath cleaning process is repeated as needed until there is no dust or other contaminants visible on the surface of the trap. We do not think that these process variations affect electric-field noise properties.

Metal deposition in **Step 2** is always performed using the same CHA Solution e-beam evaporator, but a range of variations are inevitable during this process. The pressure in the evaporation chamber is anywhere between 5×10^{-7} and 5×10^{-6} Torr. The metal deposition rates vary within a factor of 3 (see more details in Chapter ??), and the atmosphere exposure between metal deposition steps can last from minutes to days. Intuitively, we would expect these variations to have a major effect on film quality and thus electric-field noise. However, we have found no evidence of this. The metal deposition process for Traps B and C was identical, as they were mounted, coated, rotated, and recoated together. While variations in these processes may affect electric-field noise, the fact that Trap B and Trap C have such different noise magnitudes tells us that these effects are not dominant in our system.

The baking process, as described in **Step 4**, varies significantly between traps, yet does not appear to have a significant effect on pre-milling electric-field noise. Trap A was baked at the lowest temperature, and Trap B at the highest. The data in Figure 8.1a shows no correlation between the electric-field noise magnitude and the number of baking weeks. Both Trap B and Trap C were re-exposed to atmosphere and re-baked due to problems with vacuum systems and electronics (Step 6). The data in Figure 8.1b shows no correlation between the electric-field noise magnitude and the number of times the trap was exposed to atmosphere and baked.

Ion trap measurement system variations can have a significant impact on **Step 5** because electric-field noise measurements in ion traps can vary due to sources of noise that do not come from the electrode surface. Technical noise is a particularly common limitation in ion

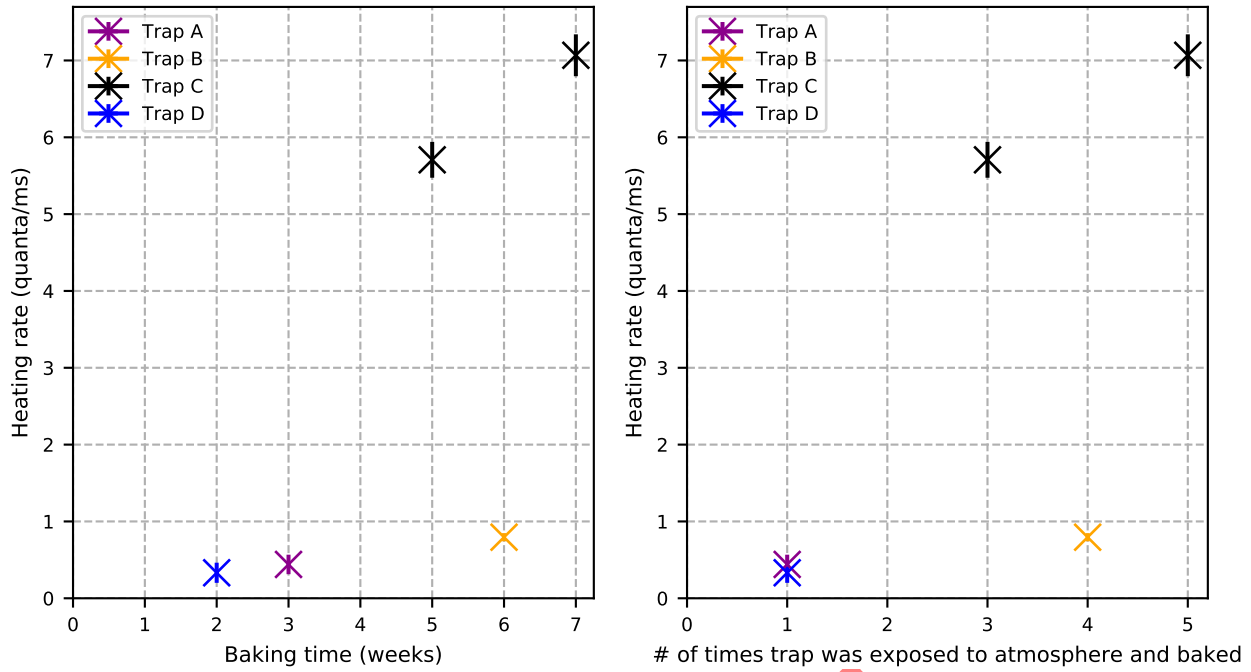
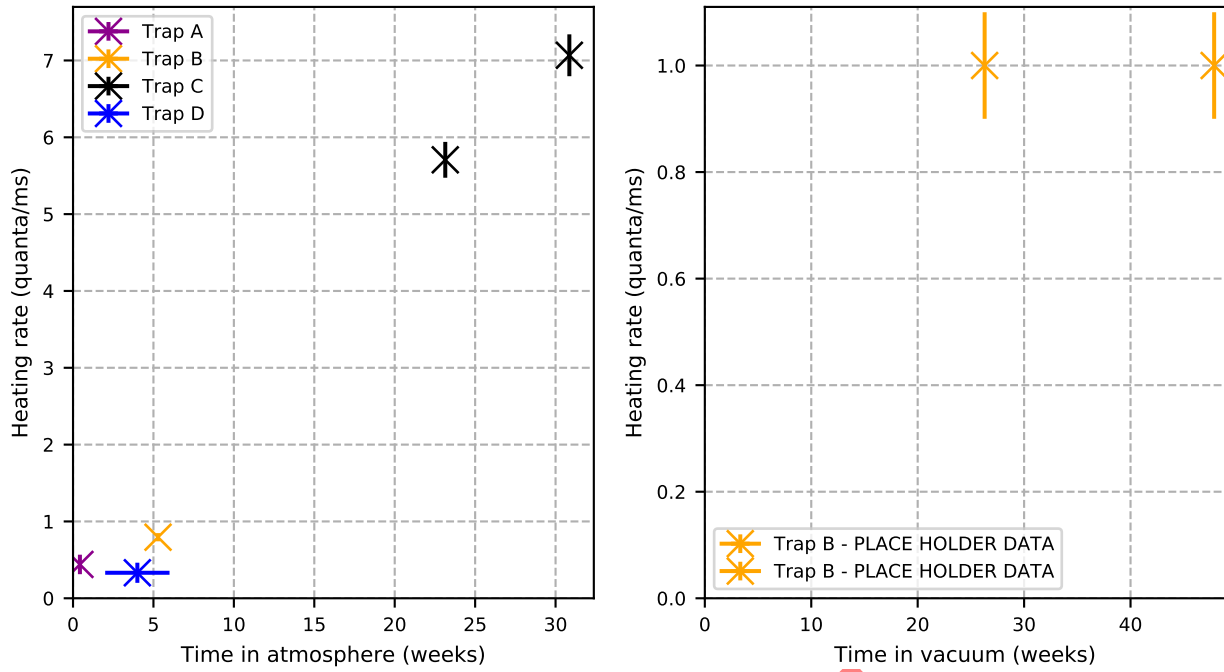


Figure 8.1

trap systems. All of the electric-field noise measurements presented here were confirmed to be limited by surface noise, not technical noise. As shown in Table 8.1, measurements of Trap A and Trap C were taken in the exact same ion trapping chamber. All three traps were measured with the same laser systems, though some upgrades and changes were made between the when Trap A was measured and when Traps B and C were measured several years later.

Of all of the process variations that we looked at, only one was correlated with electric-field noise magnitude: the amount of time that the trap was stored in atmosphere during **Step 3** (after metal deposition). This is shown in Figure 8.2a. Trap A was stored in the Class100 Berkeley Marvell Nanolab clean room for three days, then exposed to ambient air for no more than an hour before vacuum installation. Trap B was stored in the clean room for a month before initial installation, and exposed to ambient air for up to a day each time vacuum was broken, for a total ambient-air exposure-time of about four days. Before the first measurement of Trap C, the trap was stored in the cleanroom for 15 weeks, and in ambient air for 8 weeks. Between the first and second measurements of Trap C, the trap was stored in the clean room for 8 weeks, with less than 1 day of exposure to ambient air. To confirm that the traps do not simply degrade over time, we also plot measurements from Trap B taken many months apart in Figure 8.2b.

We have demonstrated that the heating rate in Trap C increased due to the trap's prolonged exposure to atmosphere. If the contaminant atoms are the primary source of electric-field noise, then the accumulation of contaminants from the air could explain why the heating



(a) Heating rates are proportional to the traps' atmosphere exposure time post metal deposition.

(b) The heating rates do not increase over time if the trap is in vacuum.

Figure 8.2

rate of Trap C was 1200% greater than the heating rate of Trap A. We can see from the data in Figure 8.3 that before milling, the fraction of air contaminants on the surface of Trap C was about 35% higher than the fraction on the surface of Trap A. A 35% increase in surface contamination does not seem consistent with the 1200% increase in heating rates between Traps A and C. This discrepancy may be explained by noise contributions from contaminants deeper in the bulk. This will be explored later in this chapter.

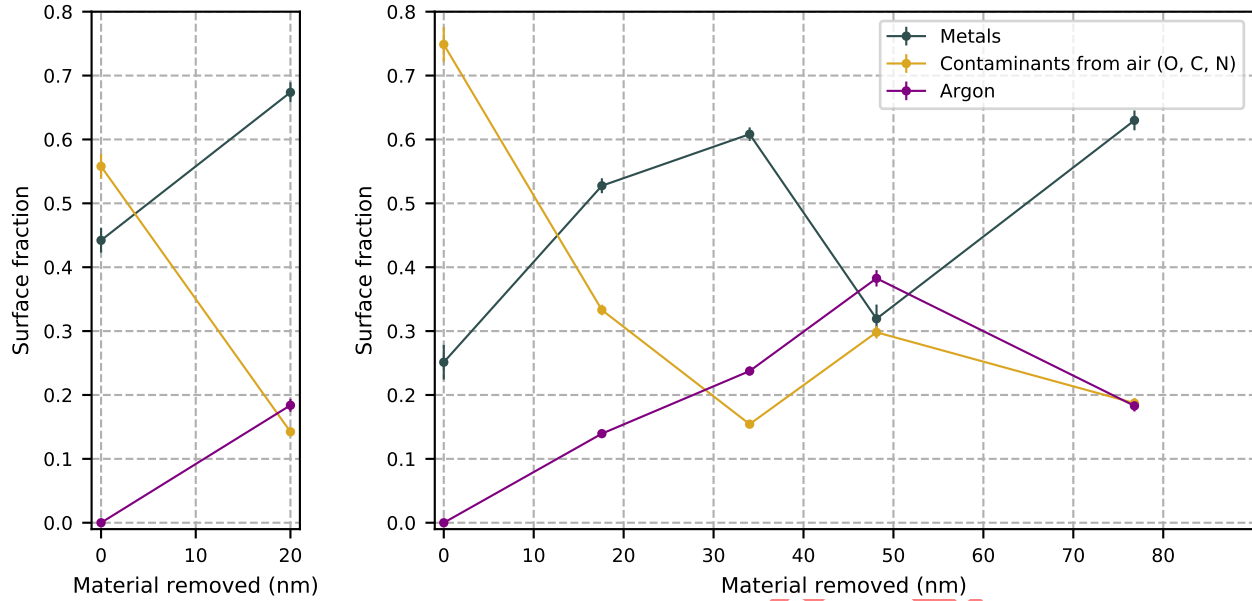
8.3 Material removal & heating-rate reductions

The data in Figure 8.1a shows no correlation between the electric-field noise magnitude and the number of baking weeks. However, the amount of time a trap has been heated may have a significant impact on how it responds to surface treatments. Heat accelerates the diffusion of contaminants from the surface into the bulk, making them far more difficult to remove by argon ion milling.

Trap A was first milled immediately following the 3 days of atmosphere exposure and 3 weeks of baking described in Section 8.2. Trap C was first milled after the 31 weeks of atmosphere exposure and 7 weeks of baking described in Section 8.2, plus an additional hour of atmosphere exposure, an additional week of baking, several months of temperature cycling between room temperature and 575 K, and surface treatment Electron 1.

We can see in Figure 8.3 that, as expected, the surfaces of both Trap A and Trap C contained high levels of air-borne contaminants before in-situ argon milling. Also as

expected, the amount of contamination on Trap A (after 3 days of atmosphere exposure) was lower than the amount of contamination on Trap C (after 30 weeks of atmosphere exposure).



(a) Trap A: data from Auger spectra taken before treatment and after two argon ion milling treatments[11].

(b) Trap C: data from Electron 1 Auger spectrum, Auger spectrum immediately following Mill 6, Auger spectrum immediately following Mill 7, Electron 2 Auger spectrum, and Auger spectrum immediately following Mill 12. See Chapter ?? for relevant Auger spectra.

Figure 8.3: Depth profiles of Trap A and Trap C.

As shown in Figure 8.3a, after 20 nm of material was removed from the surface of Trap A, the surface fraction of air-borne contaminants shrank from 0.55 to 0.14. During the argon milling process, argon was embedded into the electrode, so the argon surface fraction of Trap A rose from 0.0 to 0.18. As shown in Figure 8.3b, the surface fraction of air-borne contaminants on Trap C began at 0.75, and didn't drop to 0.16 after almost 35 nm of material was removed from the surface. Like in Trap A, the argon fraction rose as the trap was milled. The dip in argon after 75 nm of milling was likely due to a milling process change: in most milling steps the argon ions hit normal to the trap surface, but in the last milling steps in Trap C (Mill 11 and Mill 12), the argon ions hit the surface at a 45° angle.

The surface composition of Trap A after 20 nm of milling is extremely similar to the surface composition of Trap C after 35 nm of milling(8.3). The data in Figure 8.4 shows that after 20 nm of milling in Trap A, the heating rate dropped by two orders of magnitude down to 0.007 quanta/ms. Conversely, after almost 35 nm of milling in Trap C, the heating rate dropped by less than 1 order of magnitude down to 2 quanta/ms.

After 20 nm of milling on Trap A, and 35 nm of milling on Trap C, the surface compositions of the two traps are nearly identical, and yet the heating rates differ by over two orders of magnitude. If the electric-field noise from a surface is dependent primarily on the composition of that surface, then the heating rates in these two ion traps should match.

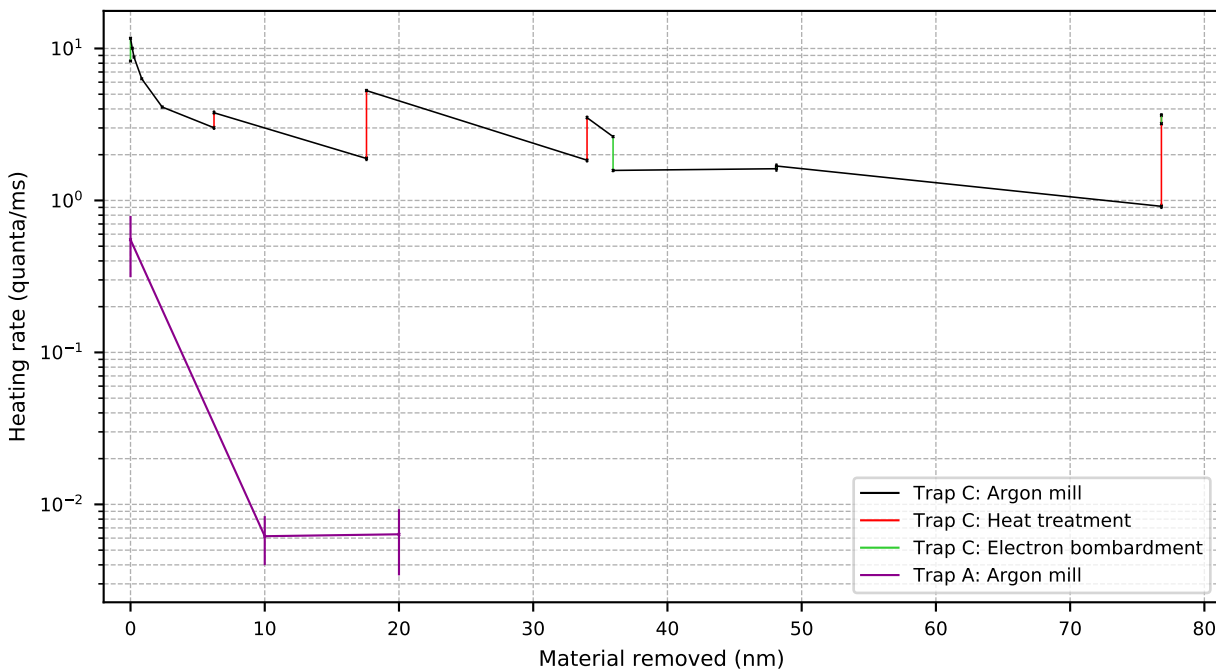


Figure 8.4: Heating rates in Traps A and C decreased as material was milled off of each surface.

The heating rates are very different, so there must be another factor, other than surface composition, driving the electric field noise in these ion traps. In Chapter 9 I will discuss the impact of surface morphology on heating rates. Surface morphology cannot explain the difference in heating rates between Trap A and Trap C immediately after milling, as they will have similar surface morphologies. In Chapter 10 I will discuss the impact of molecular contaminant structure on heating rates. Differences in surface contaminant structure cannot explain the difference in heating rates between Trap A and Trap C immediately after milling, as the argon ions will have broken up all complex molecular structures on the surface.

We can see in Figure 8.5 that nitrogen is present in Trap C and not in Trap A. N_2 from the air does not readily bind to metal surfaces, but metal-nitride films can form if nitrogen is present during e-beam evaporation or argon ion milling. However, the presence of nitrogen on the surface of Trap C cannot explain why the heating rate in Trap C is so high. If nitrogen introduced during evaporation was the primary noise source, then heating rates in Trap B would be as high as those in Trap C. They are not. If nitrogen introduced during argon milling was a major noise source, then the heating rate should have increased dramatically when the nitrogen signal rose after 48 nm of milling. It did not.

The most reasonable explanation we have found for the significant difference in heating rates between Trap A and Trap C is that electric-field noise comes not only from contaminants on the surface, but also from contaminants in the bulk. While the two traps may appear to have similar levels of carbon and oxygen on their surfaces, Trap C has significantly more of these elements buried throughout the bulk because it was exposed to extended, high-temperature heat treatments. These contaminants would have adsorbed to the surface of the trap while it sat in atmosphere. During baking and heat treatments they would have dif-

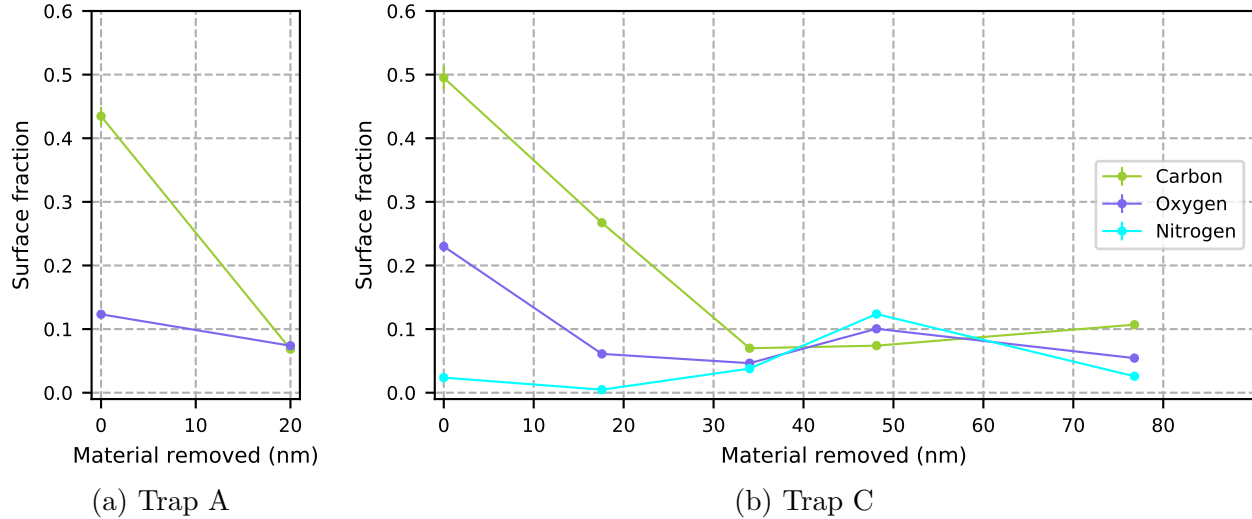


Figure 8.5: Surface fractions of all contaminants from the air. The data in these figures comes from the same Auger spectra as the data in Figure 8.5 (a) and (b).

fused through grain boundaries in the polycrystalline metal, through cavities formed during evaporation, and, at a slower rate, through the crystals themselves.

Since most contamination enters the trap through its surface, we can learn more about the contamination depth by considering how much mixing has taken place in each of the traps. Auger spectroscopy is sensitive to atoms within the top 5 nm of the surface. Since we deposit copper last, if there was no mixing of the metals, an auger spectrum would reveal only copper and contaminants from the air. If the metals were fully mixed, we would expect to see Al:Cu:Ti amplitude ratios of 35:3:1 (assuming the deposited aluminum, copper and titanium have densities of 2.7, 8.9 and 4.5 $\frac{g}{cm^3}$ respectively).

We can see in Figure 8.6a that the surface of Trap A, before milling, had an Al:Cu ratio of 4.5:1, and no titanium was present. This indicates that the metals were partially mixed, which likely took place when the trap was baking for three weeks. We can see in Figure 8.6b that the surface of Trap C, before milling, had an Al:Cu ratio of 10:1. This ratio matches the ratio of deposited metals, indicating that the metal fully mixed during the trap's 9-week baking period and 600 K heat treatments. The ratio of Ti:Cu on the pre-milled surface of Trap C is 1:1. Since titanium is deposited below copper and aluminum, we would expect a Ti/Cu ratio to be no higher than 1:3 after mixing. The excess titanium can be explained by the operation of a titanium sublimation pump after each bake of Trap C. This pump was not operated in the presence of Trap A.

On first glance, the fact that the oxygen and carbon surface fractions in the two traps look fairly similar after milling (Figure 8.5) appears inconsistent with the theory that Trap C was more deeply contaminated than Trap A. It is possible that further milling of Trap A would have revealed a pure metal surface. More likely, these plots actually do not represent true contaminant depth profiles. A portion of the the oxygen, carbon and nitrogen we see in the auger spectra were introduced during and after milling, not revealed by milling. In the study of Trap A, the trap surface built up carbon and oxygen even while stored in UHV[11]. In Trap C, outgassing of the electron filament during Auger spectroscopy was

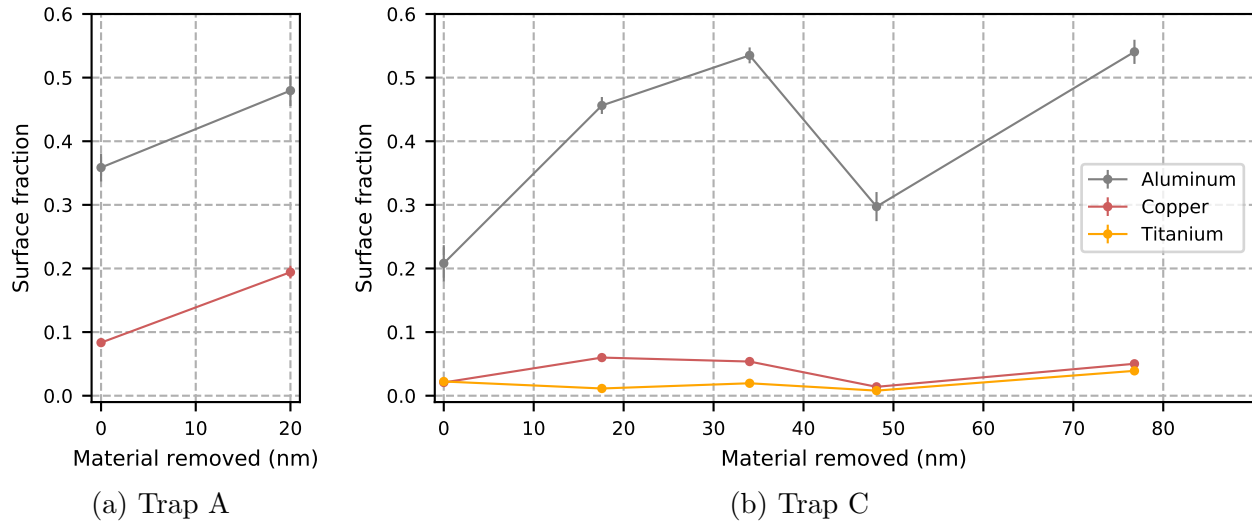


Figure 8.6: Surface fractions of all metals. The data in these figures comes from the same Auger spectra as the data in Figure 8.3 (a) and (b).

found to significantly raise the amount of carbon on the surface of the trap (see Chapter ?? for details). Rather than thinking of Figure 8.5 as true depth profiles as a contaminant depth profile, we must see it as an upper limit on the amount of contamination present in the bulk.

8.4 Summary

In summary, a large number of oxygen and carbon contaminants adsorbed onto and absorbed into the surfaces of Traps A, B and C after metal deposition while the traps were stored in atmosphere. Trap C was exposed to atmosphere the longest, so it had the highest heating rate. When each of the three traps were baked, mixing occurred between metal layers, and contaminants diffused from the surface into the bulk of the metal. Trap A was baked for a short time, and Trap C was baked for a long time, so Trap C had more mixing and diffusion than Trap A. When Trap A was milled, the majority of the contamination was removed, and the heating rates decreased by two orders of magnitude. When Trap C was milled, a significant amount of contamination remained on the surface and throughout the bulk of the electrode. For this reason, the heating rate decreased by only a single order of magnitude.

These experiments provide important considerations for those who fabricate, store and treat ion traps. Researchers should be thoughtful about whether they store their traps in atmosphere or in vacuum. Some materials build up contamination faster than others when exposed to atmosphere, and this should be considered when choosing the material of a trap that will be shipped or stored in atmosphere. For argon ion milling to be successful, the trap cannot be deeply contaminated. Aluminum is an interesting trap material in this regard, as its native oxide layer serves as a diffusion barrier to prevent extensive contamination. If this layer is milled off, the remaining surface and bulk could be very clean. Milling before baking may also be effective, as contaminants would be removed before they have had a chance to

diffuse in.

Add brownnut plot comparing our traps to traps in general

DRAFT

Chapter 9

Heat treatment experiments

This experiment began with a plan to mill away the surface of Trap C in incremental steps, stopping to measure Auger spectra and temperature scalings along the way. During each of the first few milling steps, heating rates decreased, as expected, and TAF distributions remained stable throughout the temperature scaling measurements.

It took us by surprise when, after 5 J/cm^2 of argon ion milling (Mill 5), the magnitude of the TAF distribution increased during a temperature scaling measurement. We discovered that this thermally driven transformation process saturates after a few days at high temperatures, and that we can use argon ion milling as a reset button to reactivate the surface for another thermal transformation. Armed with this information, we continued to alternate between ion milling and heat treatments. As the ion heating rates fell and rose and fell again, we gathered evidence about the underlying physical processes that cause changes in noise properties during surface treatments.

In this chapter we will describe these investigations. First we will present data on the temperature dependence and timescale of the noise transformations. We will discuss under what chemical conditions these transformations take place, how we ruled out contaminant deposition as the underlying cause of thermal transformations, and how we also (somewhat tentatively) ruled out chemical reactions. We will describe why atomic restructuring is most likely responsible for TAF distribution changes during heat treatments, and consider what we can learn from patterns in the measured TAF distributions. Gaussian fit lines are included in all TAF distribution and temperature scaling plots to guide the eye.

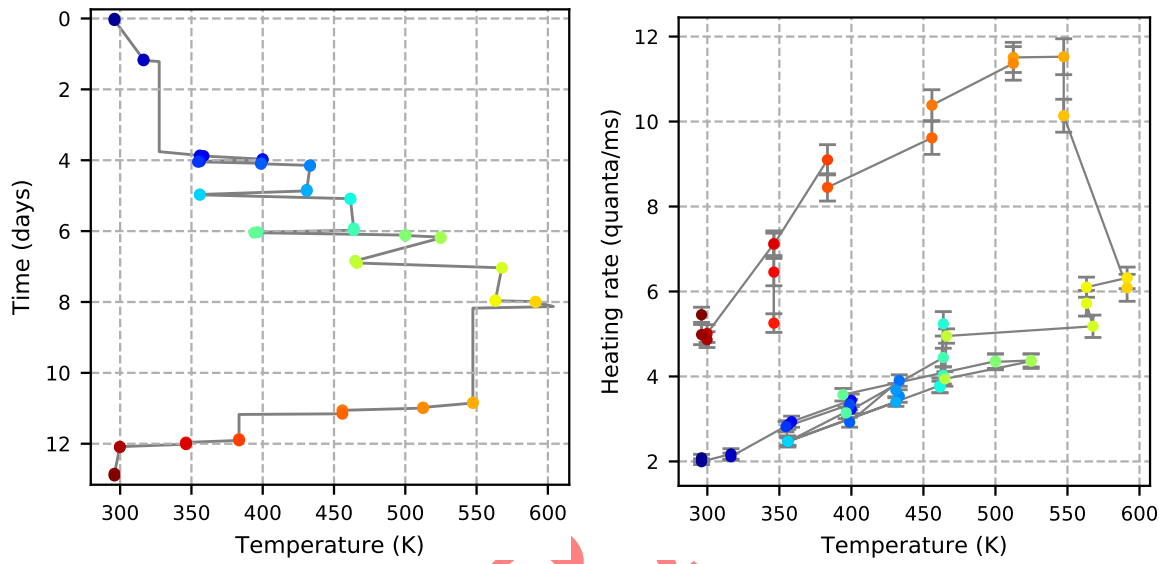
This chapter will focus solely on the noise mechanisms that are dominant at lower temperatures. We have excluded data from the 'high-temperature shoot-off', where a sharp rise in heating rates indicates that a different noise mechanism has begun to dominate.

9.1 Thermal transformation of noise sources

As we explore the impact of substrate heat on electric-field noise, we consider two categories of effects: activations and transformations. We have already discussed thermally-activated noise processes in the context of thermally activated fluctuators (TAFs) in Chapter ???. The behavior of a thermally-activated noise source is temperature-dependent, but thermal activation does not permanently alter the system. For example, in an experiment in which

the noise sources are thermally-activated but not transformed, we can measure heating rates at many different temperatures, and the results of the measurements are not affected by the order in which they were taken.

When a substrate is thermally transformed, the noise characteristics of that substrate change because the noise sources have fundamentally changed. Transformations can include the addition and subtraction of material, chemical reactions, atomic restructuring, and more. Transformations take place over time, so the effects of a heat treatment depend on both the timing and temperature of that treatment. In a thermal transformation experiment, measurements taken at the same temperature but at different stages in the heating process can produce very different results.



(a) Temperature and timing information for the heat treatment following Mill 6.

(b) Ion heating-rates measured as a function of substrate temperature. To determine the time when each measurement was taken, match the color of each heating-rate data point to the color of each point in plot (a).

Figure 9.1: During the first seven days of the heat treatment following Mill 6, the noise sources were activated by substrate heating. When the trap was held at high temperatures from Day 7 to Day 11, the noise sources were transformed.

Examples of thermal activation and thermal transformation are shown in Figure 9.1. During the first seven days of this experiment, we alternated between raising and lowering the temperature of the substrate between measurements. This is an example of heat activation because ion heating rates increased as a function of temperature, and we can see that there was no transformation during this time period because we could return to previously-measured temperatures and find the same heating rate magnitudes. The noise transformation took place while we held the substrate at or above 550 K from Day 7 to Day 11. On days 11 through 13, we took measurements at previously-explored temperatures, and we found that the ion heating rate magnitudes had increased dramatically.

From the heat treatment following Mill 6 (Figure 9.1), we learned that thermal transfor-

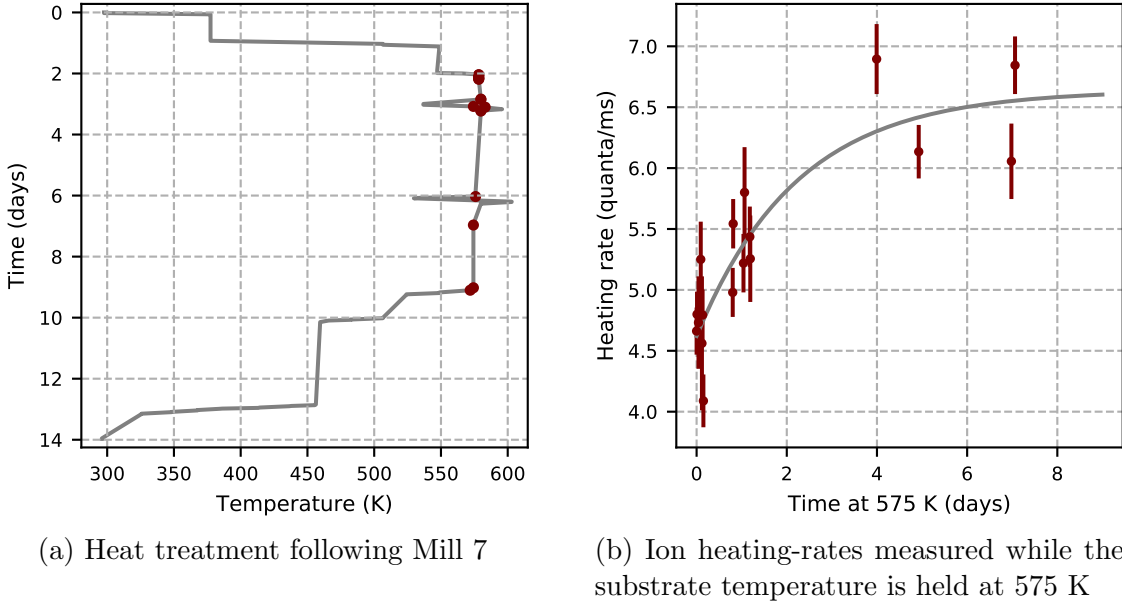


Figure 9.2: Ion heating-rates measured while the substrate temperature is held at approximately 575 K show a saturating noise transformation with a half life of 1.5 ± 0.5 days.

mation can take place on a timescale of days at temperatures above 550 K. We observed no transformation at lower temperatures over this timescale. In the heat treatment following Mill 7, we sought out additional information about the time evolution of this noise process. We raised the substrate temperature to 575 K more swiftly than before, then took measurements at 575 K repeatedly for a full week. The heat treatment process and ion heating-rate results are presented in Figure 9.2.

From the heat treatment following Mill 7 (Figure 9.2b), we learned that the noise transformation saturates. We fit the heating rate measurements to Equation 9.1

$$\Gamma = \Gamma_o + A(1 - e^{-kt}) \quad (9.1)$$

where Γ is the heating rate at 575 K, t is the amount of time spent at 575 K, and Γ_o , A and rate constant k are fit parameters. The half life λ of this transformation can be calculated directly from the rate constant k : $\lambda = \ln(2)/k$. We found that at 575 K, the noise transformation process had a half life of 1.5 ± 0.5 days. Later we will use this value to discuss the feasibility of possible underlying physical transformation processes.

In addition to providing direct insight into the underlying physics, understanding the temperature dependence and timescale of the transformation can help us identify which ion heating-rate measurements were taken during thermal transformations. This is important because when we calculate a TAF distribution from a temperature-scaling, we assume that at every temperature we are probing the same, stable distribution of fluctuators. If fluctuators are transforming while a temperature scaling is being measured, the calculated TAF distribution is not a faithful representation of the true distribution.

For this reason, when we present TAF distributions and temperature scalings in this chapter, we include only data taken before or after (but not during) noise transformations. The temperature scalings labeled as 'First' were measured quickly, and the highest-temperature

data has been excluded. The temperature scalings labeled as 'Last' were measured after we believe the noise transformation has saturated. See Chapter 7 for details on all heat treatment temperatures and timings.

9.2 Intermittent transformations

Over the course of its life in our lab, Trap C was heated dozens of times to temperatures greater than 560 K. Sometimes these heat treatments drove changes in the TAF distribution, and sometimes they did not. Determining what conditions are required for a thermal transformation to take place can help us figure out what physical changes are actually happening in this substrate when it is hot. A representative set of heat treatments are presented in Figure 9.3, including every thermal transformation that we observed.

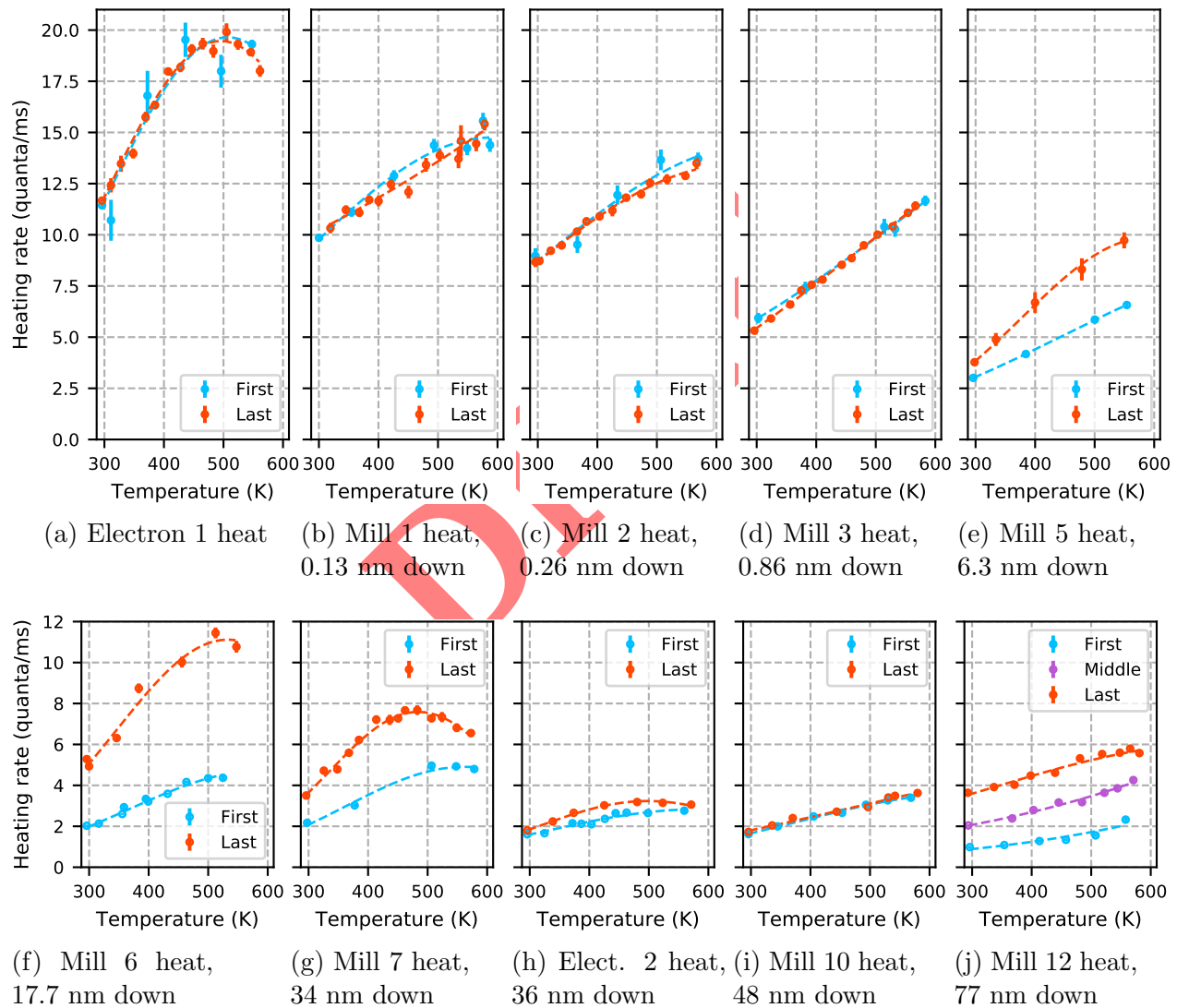


Figure 9.3: Temperature scalings measured after electron and ion bombardments show intermittent thermal transformations of noise sources.

It was after the heat treatment following Mill 10 that we first found an explanation for the intermittency of thermal transformations. By this time, the thermal transformation effect had appeared, repeated three times, and then shrunk down to nothing. We looked to our measured Auger spectra and found that changes in the line-shape of aluminum were correlated with the appearance and disappearance of thermal transformations. When the aluminum line-shape was consistent with elemental aluminum, the transformation happened. When the aluminum line-shape was consistent with aluminum oxide or aluminum nitride, the TAF distribution was unchanged by heat treatments. We correctly predicted that if we could uncover elemental aluminum with aggressive ion milling (Mill 11 and 12), we would be able to bring on another thermal transformation.

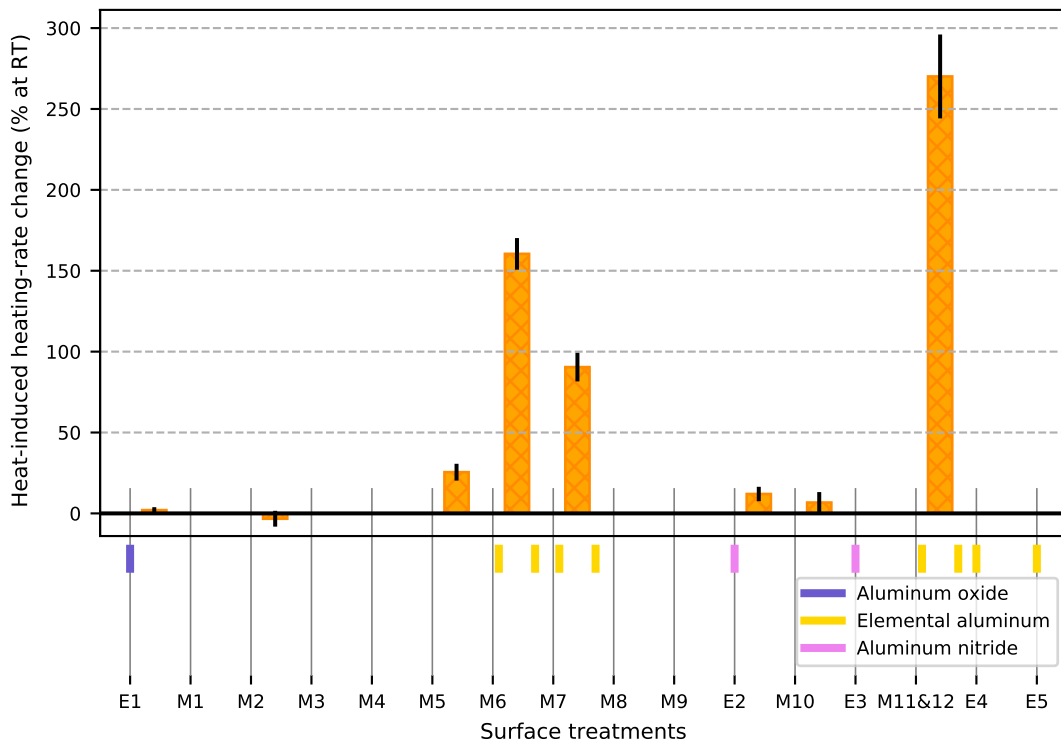
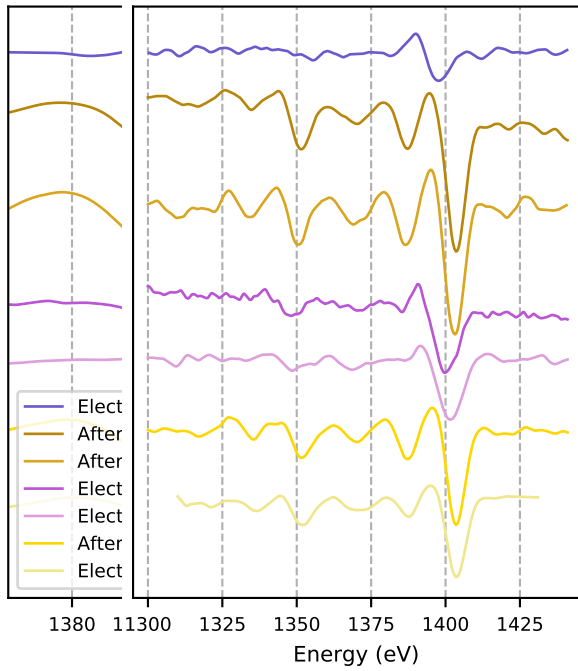


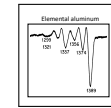
Figure 9.4: Data from heating rates measured at room temperature before and after strong heat treatments, shown in context with aluminum chemical state. Strong treatments include those in which the trap was heated to above 560 K for an extended period of time. The chemical state of the aluminum is determined from the spectra plotted in Figure ??.

The correlation between the aluminum state and the thermal transformations is shown in Figure 9.4. Orange bars indicate how much the room-temperature heating rates changed due to heat treatments. Yellow, purple and pink bars indicate the chemical state of aluminum at various times as measured with the Auger spectrometer. We have included only data taken after Electron 1, but all previously-measured Auger spectra are consistent with aluminum oxide. Data from the many temperature scalings measured before Electron 1 are consistent with no thermal transformation taking place, with the exception of one temporary spike in heating rates after an exceptionally hot heat treatment described in Section 6.5 of the Noel Thesis [26].

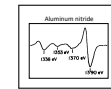


(a) Shifts in the differential line-shapes compared to the reference spectrum of elemental aluminum [45].

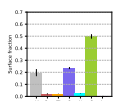
(b) The differential line-shapes of the strongest aluminum peak after each treatment are used to determine the different chemical states of aluminum after each surface treatment.



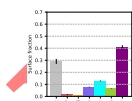
(c) Reference spectrum elemental aluminum [45]



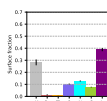
(d) Reference spectrum aluminum nitride [46]



(e) Electron 1



(f) Electron 2



(g) Electron 3

Figure 9.5: Measurements of the Auger spectrum of aluminum on the surface of our substrate reveal rich information about the chemical structure of the aluminum. Considering reference spectra, surface composition and trap history, we determined that aluminum is oxidized during Electron 1, appears to be elemental after Mill 6, Mill 7, Mill 12 and Electron 5, and is present in the form of aluminum nitride during Electron 2 and Electron 3.

When we began our surface treatment experiments, the aluminum on the surface of our chip was oxidized. Aluminum immediately oxidizes upon exposure to air, but additional native oxide growth proceeds very slowly. After hundreds of days of atmosphere exposure,

the aluminum oxide layer on our chip would have been about 5 to 10 nm thick. The presence of aluminum oxide before milling is supported by our measured Auger spectra. Elemental aluminum has its largest high-energy peak at 1396 eV (as calibrated by the manufacturers of our Auger spectrometer). When aluminum is oxidized, this peak shifts down in energy by 8 eV [47]. The largest peak in the Electron 1 aluminum spectrum is visible at 1390 eV in Figures 9.5a and 9.5b.

Thermal transformations did not happen at the beginning of the experiment when the aluminum on the surface of the trap was oxidized. They started to occur only when elemental aluminum was uncovered by milling. The transformations first appeared after Mill 5, by which point milling had removed a total of 6.3 nm from the surface and had likely broken through parts of the oxide layer. In Mill 6 we removed an additional 11 nm of material, and an Auger measurement revealed the presence of elemental aluminum. This is evidence by the large auger peak at 1395 eV in the Mill 6 and Mill 7 spectra (Figure 9.5a). This designation is further supported by the strong similarity between the line-shapes of these spectra (Figure 9.5b) and the line-shape of the full elemental aluminum reference spectrum (Figure 9.5c).

Unlike aluminum oxide, aluminum nitride does not form naturally when aluminum is exposed to air. The nitrogen found buried in the bulk of the electrode was most likely picked up by aluminum during the e-beam evaporation process. Three pieces of evidence informed our decision to classify the aluminum in Electron 2 and Electron 3 as aluminum nitride. First, the primary high-energy peak of aluminum shifts by -5 eV when aluminum is bound to nitrogen. In Figures 9.5a and 9.5b this shift is visible. Second, we found a strong similarity between the aluminum nitride reference spectrum (9.5d) and the Electron 2 and Electron 3 spectra. Third, when we look at the fractional surface compositions in Figure 9.5f and 9.5g, we see large nitrogen signals and very small copper and titanium signals. If nitrogen is present on the surface, it must be bound to one of the metals, and aluminum is the only metal available.

Now that we have measured the timescale of the thermal transformations, and we have observed that the transformations only take place when elemental aluminum is present on the surface of the trap, we can investigate the feasibility of specific physical processes that may be responsible for altering the TAF distribution during heat treatments.

9.3 Investigation of contaminant deposition

After the first thermal transformation took place (following Mill 5), we immediately suspected that contaminant deposition was the underlying cause. If something connected to the heater was starting to break down after many rounds of temperature cycling, it could outgas and deposit contaminants onto the trap surface. The timescale of this process could be anything. If the outgassed elements bind to elemental aluminum and not to aluminum oxide or nitride, then this hypothesis is consistent with the observed thermal-transformation intermittency.

Fortunately, we could test this hypothesis using the Auger spectrometer. Immediately after Mill 6 we measured the surface composition of the trap. We then heated the trap, which increased the room-temperature heating rates by 150%. After this transformation, we measured the composition of the surface again. We repeated the same surface composition

measurement process after Mill 7 and after Mill 12. When we compare the Auger spectra before and after thermal transformations, we see no evidence that contaminant deposition caused the thermal transformation of the TAF distribution.

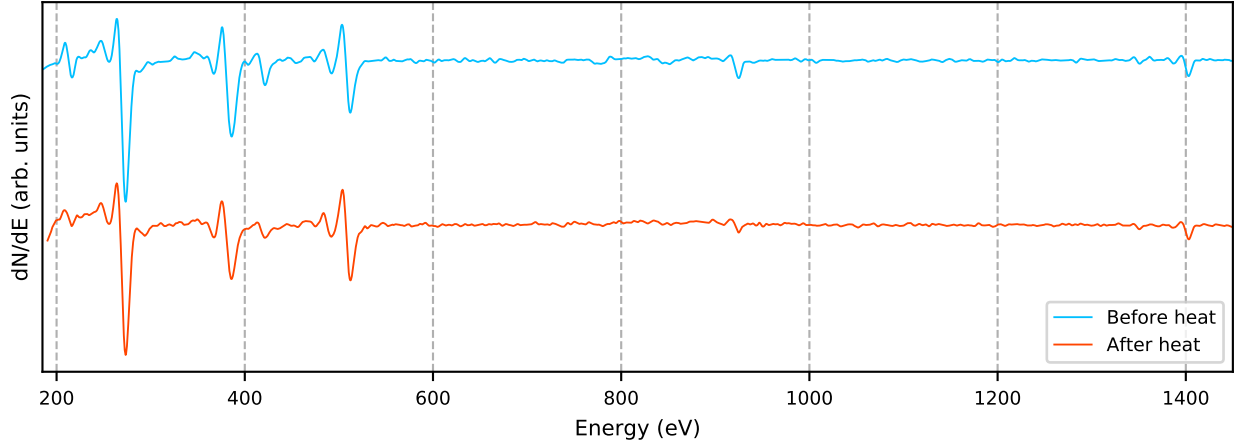


Figure 9.6: Auger spectra taken before and after the thermal transformation following Mill 7 show no new elements.

When we compare the Auger spectra in Figure 9.6 taken before and after the thermal transformation that followed Mill 7, we do not see any new elements appear on the post-heat spectrum. The spectra taken after Mill 6 and Mill 12 also showed no new elements.

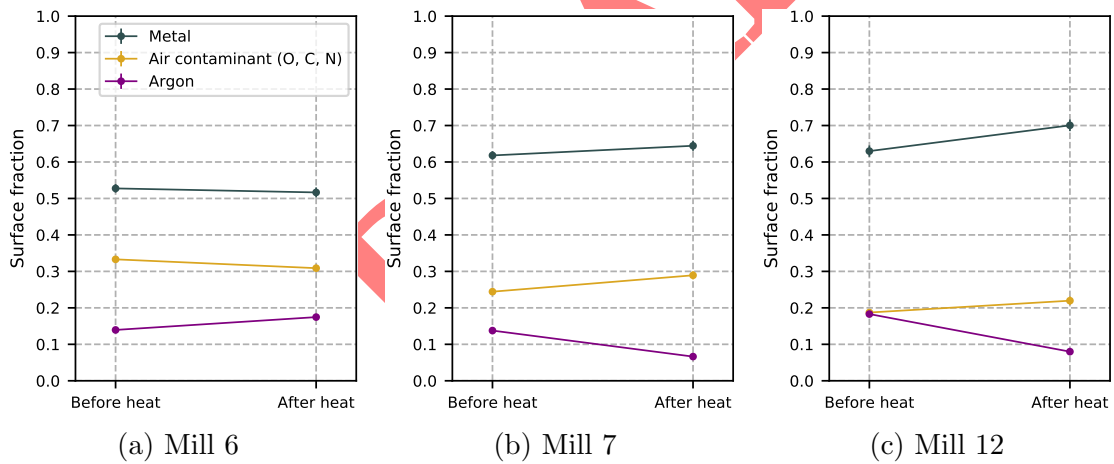


Figure 9.7: Surface fractions measured before and after thermal transformations

We can look at changes in the relative surface fractions after heating, as shown in Figure 9.7. There are no consistent trends over all three plots.

In Figure 9.8 we plot the percentage change of oxygen, carbon and argon surface fractions alongside the percent change of the room-temperature heating-rate due to each thermal transformation. We would not necessarily expect the percent increase in heating rates to match the percent increase in a specific deposited contaminant, even if deposition was the underlying cause, but there is value in noticing that the changes in heating rates are much larger than the changes in surface composition.

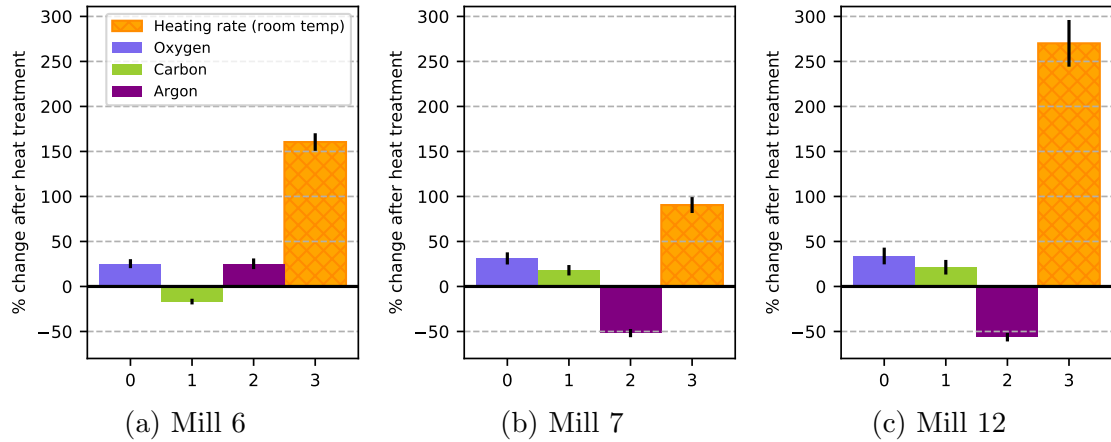


Figure 9.8: Surface fraction and room-temperature ion heating-rate changes from measurements taken before and after thermal transformations

9.4 Investigation of chemical changes

The second hypothesis we developed to explain the underlying cause of thermal noise transformations was that some sort of chemical change is taking place on the surface of the trap. We have found no evidence that any chemical changes are taking place when we heat.

The first thing we looked at when exploring this hypothesis was the line-shape of each element. As discussed in the context of aluminum in Section 9.2, the shape of the Auger spectrum can reveal information about the chemical structure of certain elements. We did not see any changes in Auger spectra to indicate that a chemical change was taking place (see Figure 9.7 and Figure 9.9)

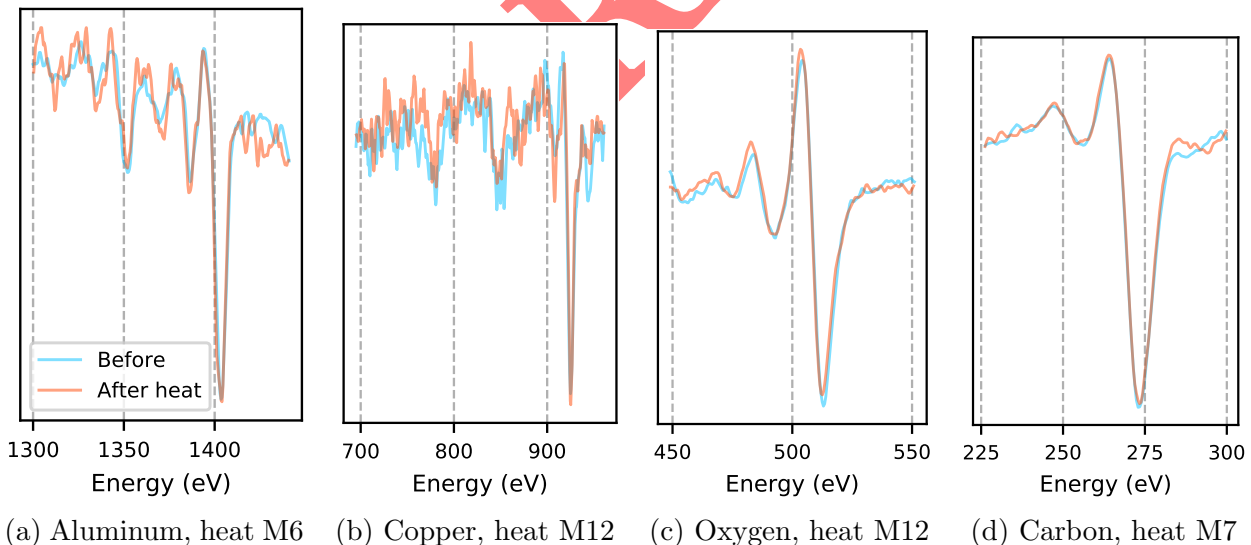
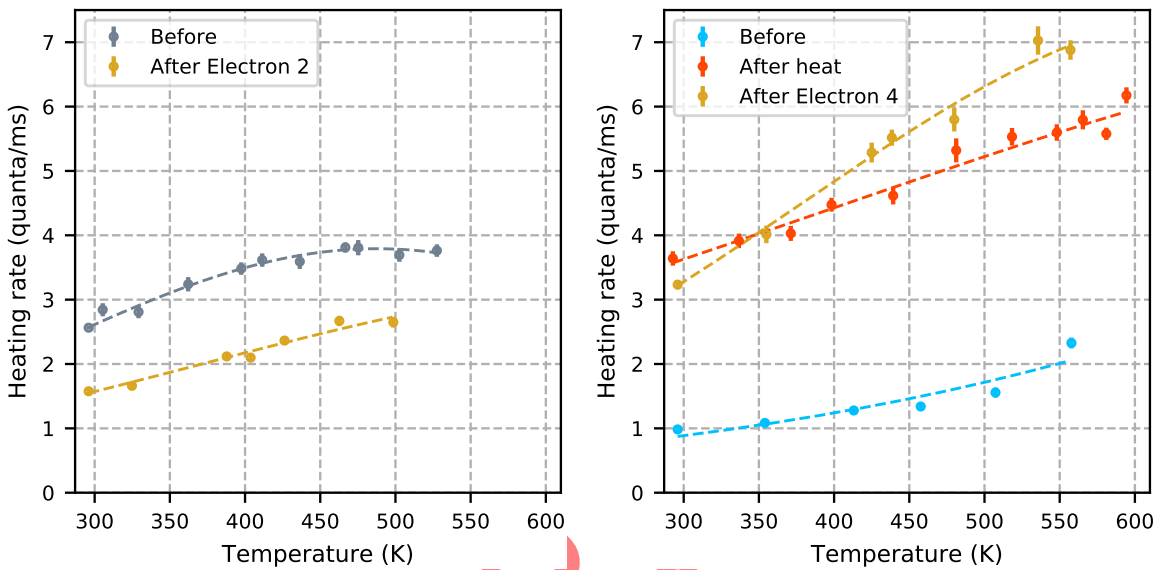


Figure 9.9: Line-shapes of aluminum, copper, oxygen and carbon measured before and after thermal transformations show no chemical changes.

Auger line-shapes cannot reveal all feasibly relevant chemical information. For example,

Auger spectroscopy depends on a steady beam of electrons bombarding the trap surface throughout the measurement process. These electrons can break up complex hydrocarbons, making these structures difficult if not impossible to detect with an Auger spectrometer (this process will be discussed in detail in Chapter 10). Complex hydrocarbons may produce noise with a completely different magnitude than individual carbon atoms, so we seriously considered the possibility that complex hydrocarbons form during heat treatments. This hypothesis is consistent with thermal transformation intermittency if elemental aluminum acts as a catalyst in the reaction. This hypothesis is also consistent with the fact that argon ion milling acts as a reset button. Perhaps the ion milling process breaks up hydrocarbons, thus lowering the noise, and when the substrate is heated the carbon atoms recombine.



(a) Heating rates at all temperatures dropped after surface treatment Electron 2 (76 kJ/cm²). (b) Heating rates rose at high temperatures after surface treatment Electron 4 (281 kJ/cm²).

Figure 9.10: Surface treatment Electron 2 showed that it is possible to lower heating rates via electron bombardment, but after Electron 4 we saw that electron bombardment does not reverse the effects of a thermal transformation.

We tested the hydrocarbon growth hypothesis by doing a thermal transformation and then an electron bombardment. If the rise in heating rates during the thermal transformation was caused by hydrocarbon growth, we would expect to see this electron treatment bring the noise back down to pre-heat levels. Instead, we saw heating rates rise at high temperatures (Figure 9.10b). We know from surface treatment Electron 2 that electron bombardment can significantly lower heating rates, possibly by breaking up carbon structures. However, thermal transformations of electric-field noise cannot be caused by hydrocarbon growth.

We cannot eliminate chemical reaction as a possible underlying cause of thermal transformations. Some chemical structures are broken up by argon ions, and not by electrons, and therefore cannot be ruled out by our experiment. However, we have not been able to find a chemical reaction that takes place on a 1.5-day timescale at 575 K, requires aluminum as

a catalyst, combines the elements present in our system, and is not broken up by electrons. For this reason, we set the chemical reaction hypothesis aside.

9.5 Investigation of atomic restructuring

The data we have collected is consistent with atomic restructuring being the underlying cause of thermal transformations. Heat-induced atomic restructuring includes the smoothing out of sharp edges, the healing of defects, and the formation of hillocks. These changes take place when the atoms have enough thermal energy to move, and they are generally driven by strain reduction.

9.5.1 Recrystallization temperatures

In Section 9.1 we presented evidence that the transformation process does not take place at low temperatures, and that it had a 1.5-day half life at 575 K. To determine whether or not this is a reasonable timescale for atomic restructuring, we look at the recrystallization temperature of aluminum.

The initial recrystallization temperature of a pure, bulk metal (the lowest temperature at which recrystallization takes place on a 1-hour timescale) is typically about half its melting temperature. Bulk aluminum, which melts at 930 K, has an initial recrystallization temperature of 470 K [48]. The addition of impurities to the metal slows down recrystallization through a process called *impurity drag* [49], where impurity atoms impede the motion of the bulk atoms due to atomic size mismatch [48].

In [48], Drits et. al. did a series of experiments measuring recrystallization temperatures of aluminum films with different impurities. They found that the addition of impurities raised the recrystallization temperature of bulk and foils of aluminum, with the effect of adding impurities saturating as the concentration was raised. Most relevant to our work was the addition of titanium, which raised the recrystallization temperature by 110 K and saturated at 0.5%. Copper had a smaller impact than titanium, and the other impurities that we are interested in (carbon, oxygen, nitrogen) were not considered.

Grain growth in metal thin films has been found to be slower than in bulk metals due to interactions at the film/substrate interface [49]. Given that our trap is an aluminum thin film with titanium and other impurities, it should have a recrystallization temperature of over 580 K (but not too far over). The fact that we measure a 1.5-day half life at 575 K is consistent with this.

Metals with impurities often have something called *secondary grain growth*, where the recrystallization process saturates at one temperature, and then restarts at a higher temperature as the metal atoms break through impurity barriers [49]. We have seen secondary thermal transformation in our system. After extensive heating at 585 K and 555 K following Mill 10, we thought the thermal transformation had saturated. When we subsequently raised the temperature of the trap to 615 K and held it at that temperature overnight, the thermal transformation effect doubled in magnitude.

Thermal transformation driven by atomic restructuring is also consistent with the transformation intermittency that we observe. We saw that no thermal transformation took place

when aluminum oxide or aluminum nitride were found on the surface instead of elemental aluminum. Aluminum oxide and aluminum nitride have melting temperatures of 2340 K and 2470 K respectively. This would set their recrystallization temperatures at around 1170 K and 1235 K. The atoms in an aluminum oxide or aluminum nitride surface would not be mobile at even our highest measurement temperature of 615 K.

9.5.2 Morphological changes: annealing

There are three types of morphological changes that commonly take place when a metal thin film is annealed: the bulk recrystallizes, atomic-scale surface roughness smoothes out, and hillocks grow.

During recrystallization, crystal grains in the bulk merge together and grow in size. This process has a significant impact on the surface roughness. Recrystallization typically raises the RMS roughness of the surface by growing large features, while simultaneously lowering the roughness frequency by incorporating small particles into larger structures. This process is illustrated in Figure 9.11.

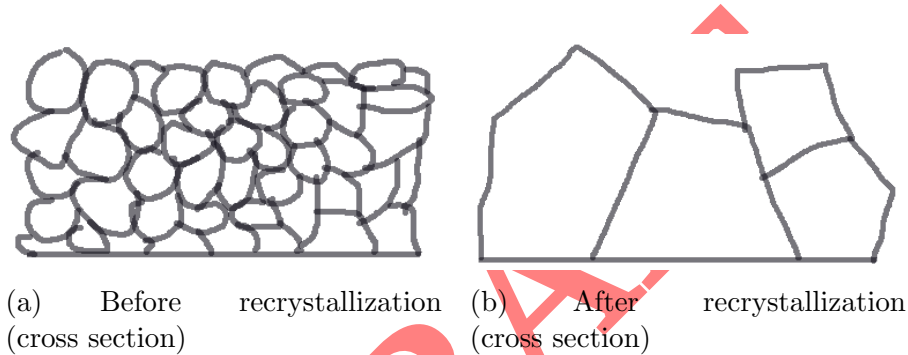


Figure 9.11: This cartoon of recrystallization (inspired by [50]) illustrates how the growth of large features increases the RMS roughness while decreasing the roughness frequency.

These topological changes have been observed experimentally. Figure 9.12 shows results from a series of experiments by Qin et. al. in which an aluminum oxide thin film was annealed at a temperature of 770 K for varying amounts of time [51]. Measurements plotted in Figure 9.12a show the RMS roughness increasing as the annealing process proceeds. Measurements plotted in Figure 9.12b show the frequency of the surface roughness decreasing throughout the annealing process.

Hillocks form on metal thin films due to strain mismatch on surfaces during heat treatments. Chang et. al. Found that pure aluminum films did not form hillocks when heated, as the aluminum atoms were free to move and reduce strain as needed [24]. Hillocks only formed during heat treatments after the aluminum film was exposed to air and formed a native oxide layer. The oxide layer locks the surface atoms in place. Strain builds up in the metal underneath the surface, and the pressure can only be reduced by the aluminum breaking through the oxide layer, spilling out and forming a hillock.

We removed Trap C from vacuum following the final surface treatment presented Chapter ???: Electron 5. Immediately before the final electron treatments, the trap underwent a major thermal transformation (the heat treatment following Mill 12). At the time when the trap

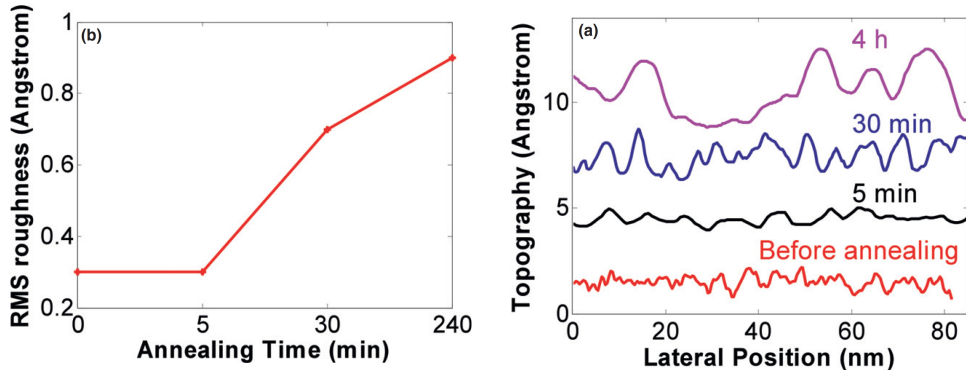


Figure 9.12: [51]

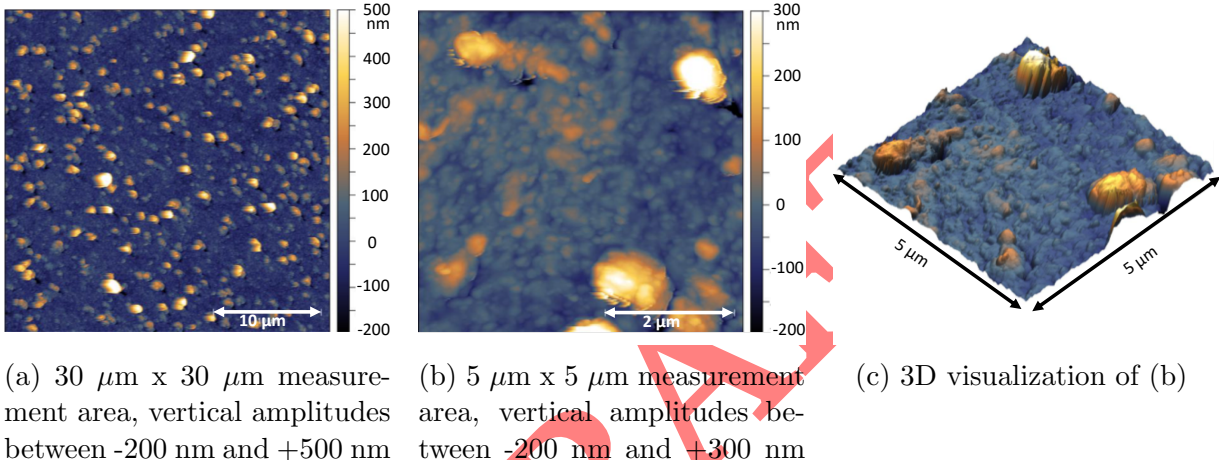


Figure 9.13: AFM measurements of Trap C, taken when the trap was removed from vacuum after surface treatment Electron 5. These bumps look like hillocks, as studied and imaged in similar systems [52].

was retired, it was in what we call the 'thermally transformed' state (as opposed to the recently-milled state). Subsequent AFM measurements, shown in Figure 9.13 revealed that there are micron-high features scattered across the surface of the trap. These features look like hillocks.

Given the extensive heat treatments that our trap went through, with and without a native oxide layer, it is unsurprising that hillocks would be present. However, this does not necessarily mean that hillock growth is the underlying cause of noise growth from heat treatments. Hillock growth is enhanced by native oxide layers, not impeded by them. This is in direct opposition to our observation the thermal noise transformations only take place when no oxide or nitride layer is present.

9.5.3 Morphological changes: milling

We have observed experimentally that argon ion milling can reset thermal transformations that have already saturated. This means that whatever heat treatments are doing to increase the noise, milling must be doing the opposite. We ran a series of simple Monte-Carlo simulations, and found that ion milling actually counteracts all of the affects of annealing: it increases atomic scale surface roughness while removing large features.

In this simulation, an aluminum atom (plotted in grey) on a smooth surface has a 40% chance of being sputtered by 200 eV argon ion incoming normal to the surface. A carbon atom (plotted in green) in the same scenario has a 3% chance of being sputtered [53]. When dislodged, atoms can move in any direction. If the atom hits a feature on its way out, it redeposits on that feature. Further simulation method details can be found in Chapter 5.

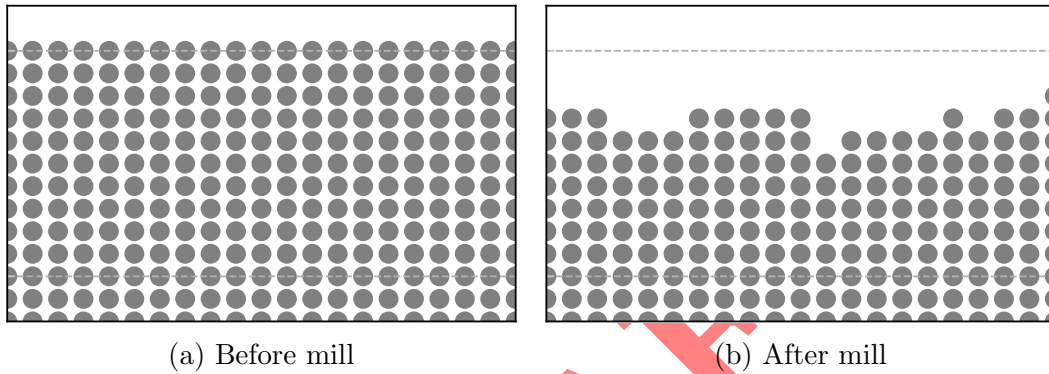


Figure 9.14: Monte-carlo simulation: 10 ions per lattice site, all aluminum atoms.

In the simulation in Figure 9.14 we begin with a flat aluminum surface, and hit each surface lattice cite with ten argon ions. Surface roughness increases.

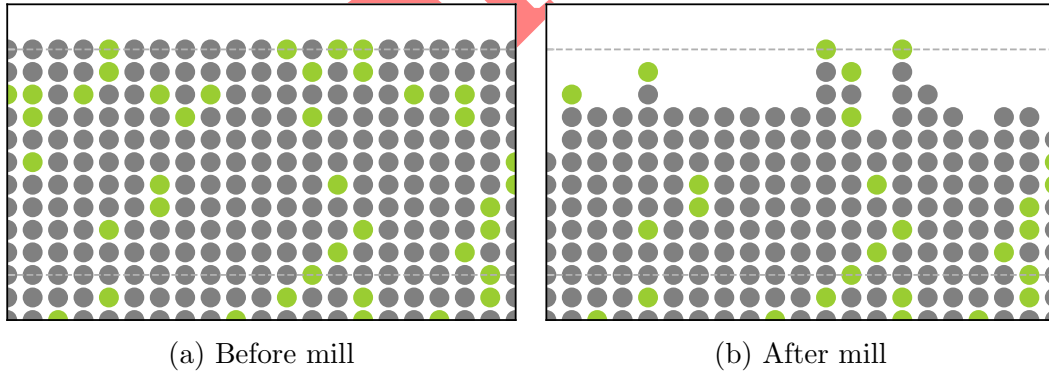


Figure 9.15: Monte-carlo simulation: 10 ions per lattice site, mix of carbon and aluminum atoms.

In the simulation in Figure 9.15 we begin again with a flat surface, but this time 20% of the atoms throughout the aluminum film are switched to carbon. Again we hit each surface lattice cite with ten argon ions. Again surface roughness increases, and we start to

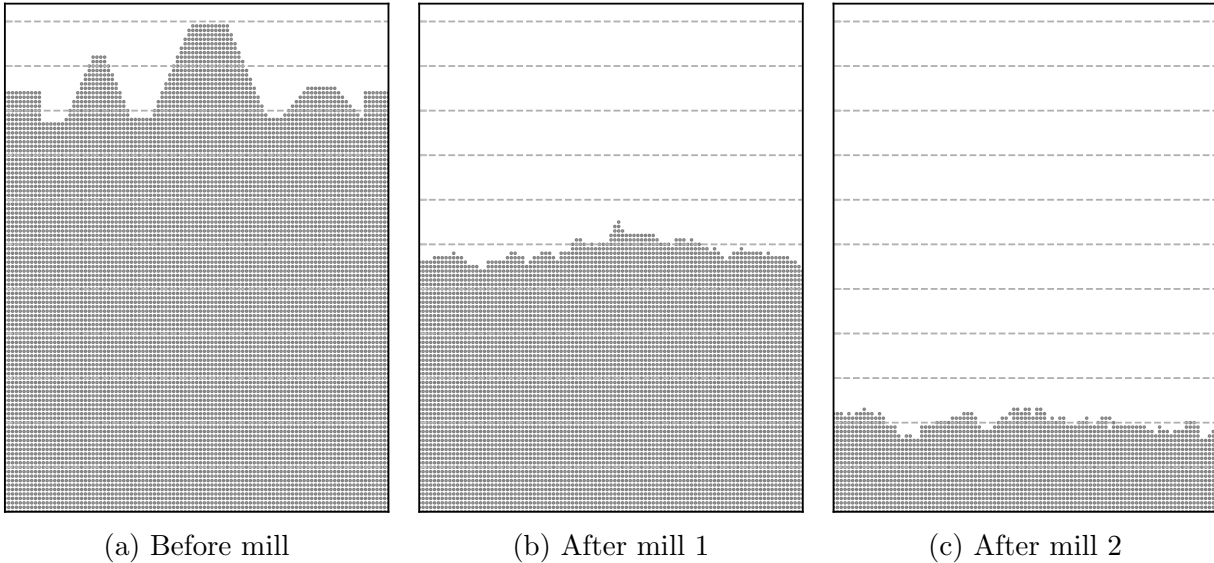


Figure 9.16: Monte-carlo simulation: 120x2 ions per lattice site, all aluminum atoms.

see needle-type structures forming in places where carbon atoms have severely impeded the sputter rate.

In the simulation in Figure 9.16, we explore the impact of milling on large, atomically smooth aluminum structures. We see that these large features are milled away by extensive milling (two rounds of 120 ions each), leaving a flat surface with atomic scale roughness.

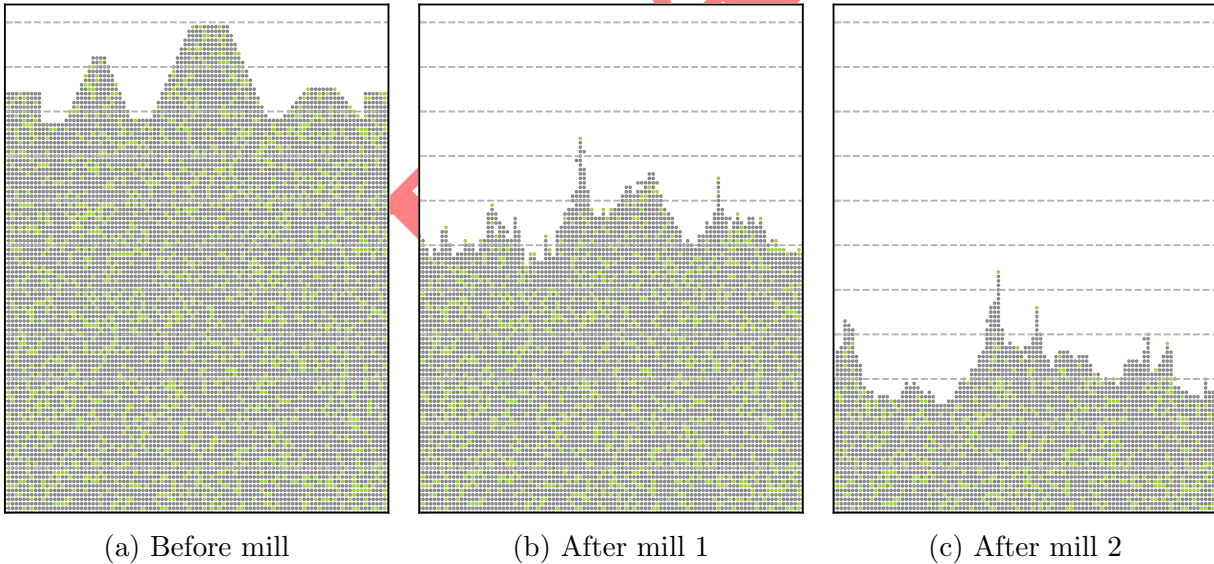


Figure 9.17: Monte-carlo simulation: 120x2 ions per lattice site, mix of carbon and aluminum atoms.

In the simulation in Figure 9.17, we investigate the combined effects of large structures and mixed substrates. This material is 80% aluminum, and 20% carbon. After 240 ions of milling, we see that the initial features are mostly milled away, and we are left with an

incredibly rough surface.

In all of our milling combined, we removed (experimentally) a total of about 75 nm of material from the surface of our trap. This is not nearly enough to remove a 300-nm tall hillocks found by the AFM. Since small milling doses can have a large impact on electric field noise, and can entirely reverse noise increases due to heating, hillocks cannot explain the thermal transformation of heating rates in our system.

The far more likely explanation is that thermal transformations of noise are caused by heat treatments smoothing out atomic surface roughness, and that milling reverses this effect by bringing atomic scale surface roughness back.

9.5.4 Correlated and uncorrelated noise sources

When heating rates in our trap increased after annealing, we were surprised. We had predicted, for a variety of reasons, that heat treatments would have the opposite effect. Heat can drive contaminant desorption, reducing the total number of noise sources. Recrystallization evens out the work function across the surface of each crystal grain, thus reducing the magnitude of dipole fluctuations as adsorbates move between binding sites. Annealing reduces nanoscale roughness, which has been found to be proportional to the resistivity of thin films [54], and a rise in resistivity corresponds to a rise in charge fluctuations in metals.

When we ran our heat treatment experiments, saw heating rates go up, and found evidence that the transformation is linked to a decrease in atomic-scale surface roughness, we had to come up with some new theories for how surface noise might work. Here we present one viable possibility.

The electric-field noise from a number (N) of independently oscillating sources on a surface, each producing noise of amplitude A , is proportional to $A*\sqrt{N}$. The noise scales with the square root of the number of noise sources because when the oscillations are independent, they will sometimes move in opposition to each other, cancelling out each other's electric fields. If all of the sources move in sync, the total noise scales as $A * N$.

Let us assume that electric-field noise in ion traps is dominated by interactions between the metal substrate and its non-metal contaminants (this is not a new idea). On a surface with atomic-scale roughness, there would be large variations in adsorbate-metal binding energies[43]. Conversely, on a single facet of a crystal, all identical adsorbates will have very similar binding configurations.

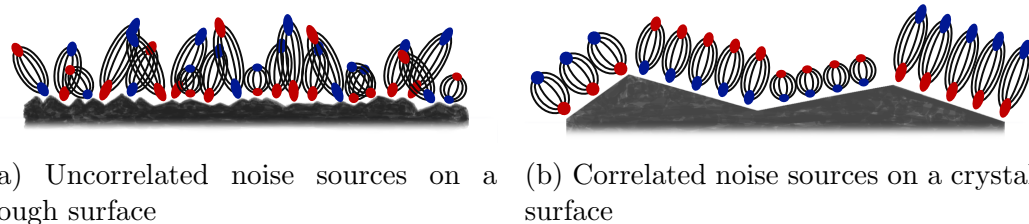


Figure 9.18

As illustrated in Figure 9.18, we imagine that atoms bound to a single crystal facet, all with identical binding configurations, may start to oscillate in sync. We imagine that this is less likely to happen on an atomically-rough surface where binding energies vary.

Let us consider a system of independent noise sources that has been heated, raising the noise-source correlation number by a factor of ten. Before treatment, the total noise amplitude is equal to $A * \sqrt{N}$. After treatment, the amplitude of each coordinated set is equal to $10 * A$, and there are $N/10$ independent sets. The total noise is now equal to $10 * A * \sqrt{N/10}$, and the noise has gone up by a factor of 3.2. This is similar to the increase in ion heating rates that we observed after the heat treatment following Mill 12.

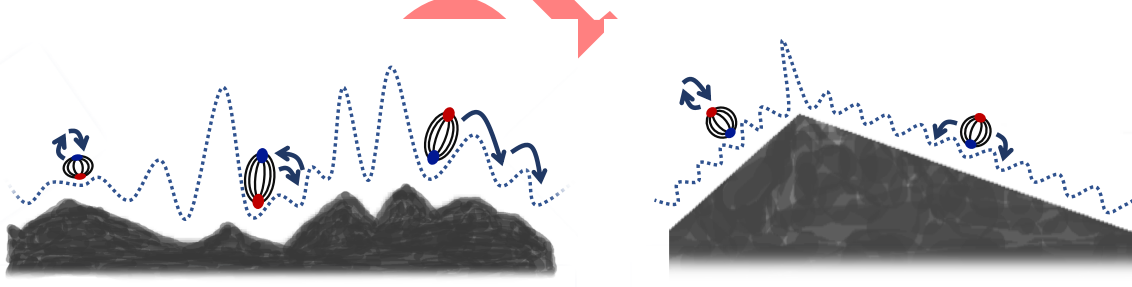
We will not present a physical noise model to explain how noise sources become correlated, and we do not know if a 10-fold increase in correlation number is reasonable after heat treatment. Further theoretical work in this area will be critical to determining the feasibility of this theory.

9.5.5 TAF distributions and surface binding energies

In previous sections, we discussed the significance of surface treatments that raised and lowered the magnitude of the electric-field noise measured in our system. These treatments also shifted and re-shaped the measured TAF distribution. It is interesting to consider the significance of these TAF changes in the context of surface roughness.

In applying the TAF model, we state that the noise in our system is generated by a distribution of thermally activated fluctuators with a range of energy barriers. The TAF model is agnostic to the physical form of the fluctuators, and to the source of the energy barriers, but for the purpose of this section we consider a specific physical TAF manifestation.

Suppose that each adsorbate is a fluctuator. Suppose also that the energy barrier of each fluctuator is equal to the binding energy between the adsorbate and the metal surface. The potential landscapes of rough and smooth surfaces are illustrated by the blue dotted lines in Figure 9.19. Adsorbates can fluctuate by moving between lattice sites, or by binding and unbinding at a single site. Electric-field noise is generated when the dipole moment of the adsorbate changes along with the adsorbate-surface binding configuration.



(a) Adsorbate TAFs on a rough surface

(b) Adsorbate TAFs on a crystallized surface

Figure 9.19: Cartoon illustration of the potential landscape of surface binding energies on rough and crystallized surfaces. Variations between adjacent sites are much larger on the rough surface.

Adsorbate-surface binding energies are stronger in areas of locally positive curvature than in areas of locally negative curvature [43]. (add order of magnitude estimate) As a result, adsorbates on an atomically rough surface interact with a wide range of different energy barriers. Conversely, on a single crystal facet, lattice sites are periodic and identical.

Therefore, on a recrystallized surface, adsorbates interact with a fairly uniform distribution of energy barriers.

If TAF energy barriers correspond directly to surface-adsorbate binding energies, then the TAF distribution of a crystallized surface should be strongly peaked, and the distribution of a rough surface should be wider and flatter. This is a direct consequence of rough surfaces providing a wider variety of surface binding sites.

Consider the TAF distributions presented in Figure 9.20. In Plot (a), we see that before milling the distribution was strongly peaked, with the peak centered at an energy of around 0.6 eV. In each of the first four thermal transformations (Mill 5, Mill 6, Mill 7, and Electron 2), the TAF distribution narrowed, grew, and re-centered to an energy between 0.5 and 0.6 eV. These transformations are consistent with an atomic-scale smoothing process that lowers the variety of surface bonding energies.

If the gaussian fit lines are extended, it appears that these heat treatments may significantly lower the magnitude of low-energy TAFs. This would be incredibly useful in cryogenic ion-trap systems, where ion heating rates are dominated by low-energy TAFs. Our extrapolated trend is consistent with the results from a previous experiment, where traps annealed at high temperatures during fabrication were found to have significantly lower heating rates than traps annealed at lower temperatures (note: there is some uncertainty in the appropriate interpretation of these results due to evidence of technical noise)[55].

The two heat treatments following Mill 12 do not fit the same pattern. Mill 11 and Mill 12 were the only milling steps in which we milled at a 45° angle rather than straight on. It is possible that the angled milling had a qualitatively different impact on the surface morphology, and that subsequent annealing was also somehow qualitatively different. There may also be other factors at play that we have not considered.

Ion milling not only flattens the TAF distribution, but also shifts the energy peak. We did two rounds of low-dose milling and heating experiments to study the qualitative effects of milling on the TAF distribution. The first round included Mill 1, 2, 3, and 4. The second round took place after the thermal transformation following Mill 7 brought back a strongly-peaked TAF distribution, and included Mill 8 and Mill 9. These TAF distributions are presented in Figure 9.21.

In both rounds of low-dose milling, the first dose flattened out the TAF distribution and appears to shift its peak to the left. Additional milling shifts the peak far to the right, while maintaining its flattened shape. If the gaussian fit lines are extended, it appears that the first dose in each round may actually raise the amplitude of lower-energy TAFs, while high-dose milling lowers the amplitude of these same TAFs. Measurements of ion-milled surface at cryogenic temperatures have found that for some materials ion heating rates rise after ex-situ milling, and for others they fall [14].

It is interesting to observe these patterns, and to see them repeated. However, we have not come up with an elegant explanation for why the TAF peak shifts first to the left and then right during the milling process.

9.5.6 Ex-situ surface treatment and characterization experiments

We have discussed a set of simulations and a literature review that gives us confidence that our observed noise transformations are caused by changes in the surface roughness of our

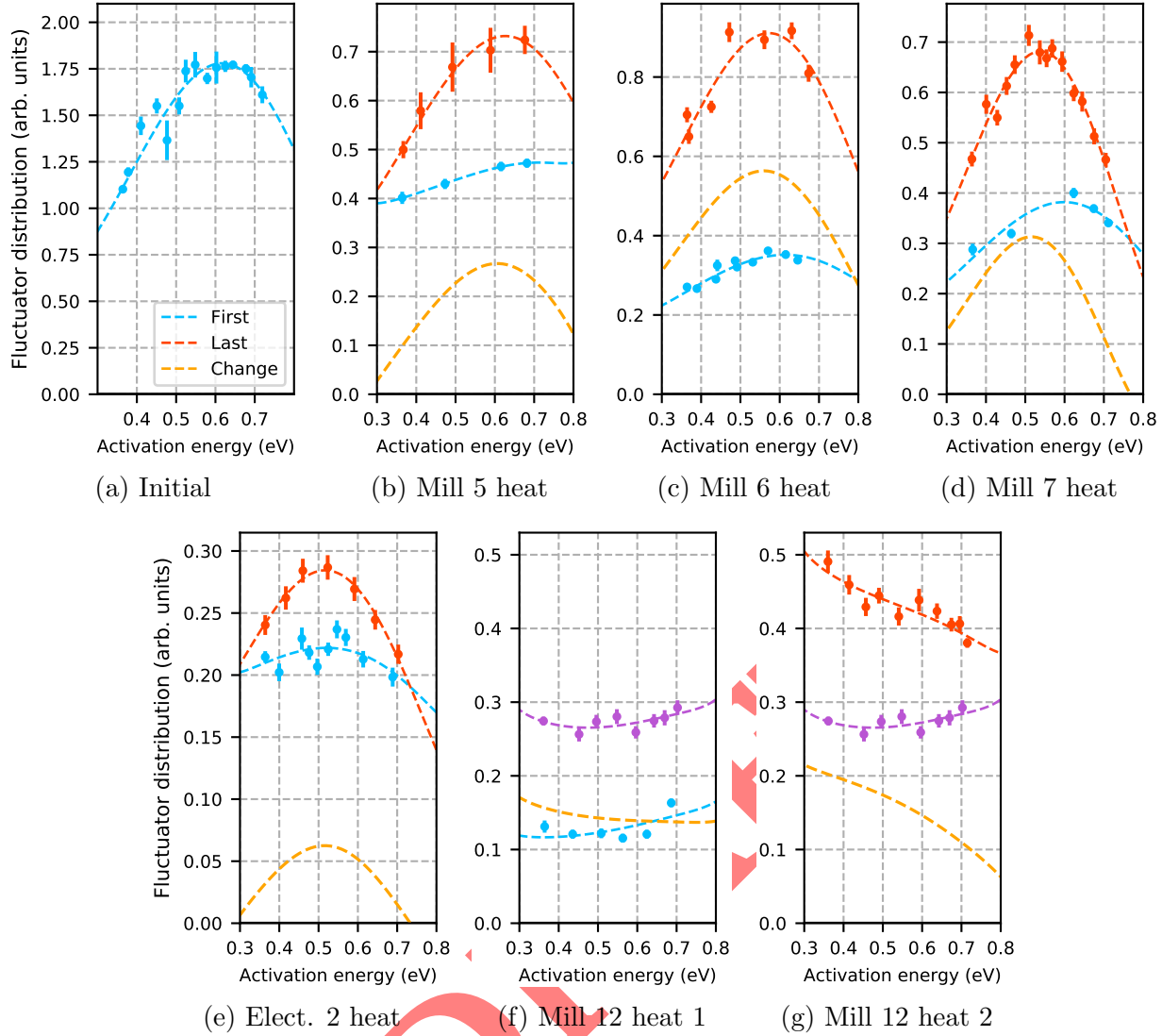
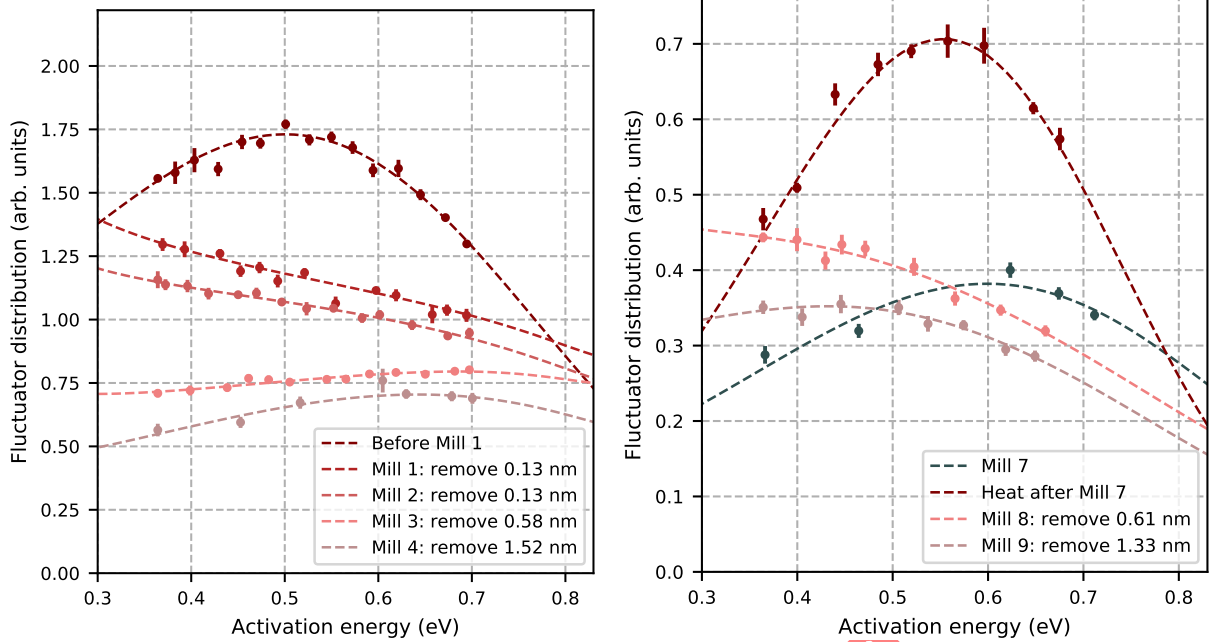


Figure 9.20: TAF distribution changes due to every observed thermal transformation

ion trap. This work would benefit from an additional series of experiments that directly correlates electric field noise with surface roughness and surface morphology.

If we had unlimited resources, we would run parallel experiments in which we execute identical surface treatments in two separate vacuum chambers. The first setup would be our standard ion-trapping chamber, where we have our Auger spectrometer, ion-trapping tools, button heater and argon ion gun. The second setup would be an ex-situ characterization chamber, where we would have identical surface treatment tools, a second Auger spectrometer (for a direct comparison of the substrates and surface treatments), an AFM, an SEM, and an XPS.

At this time, we have access to all of these tools through the Berkeley Marvell Nanolab and through our collaboration with scientists at Lawrence Livermore National Laboratory. However, there is no single vacuum chamber containing everything we need for ex-situ characterization. As a result, the trap must be exposed to atmosphere between treatments



(a) TAF distributions from initial small milling steps

(b) TAF distributions from small milling steps following the Mill 7 heat treatment distribution

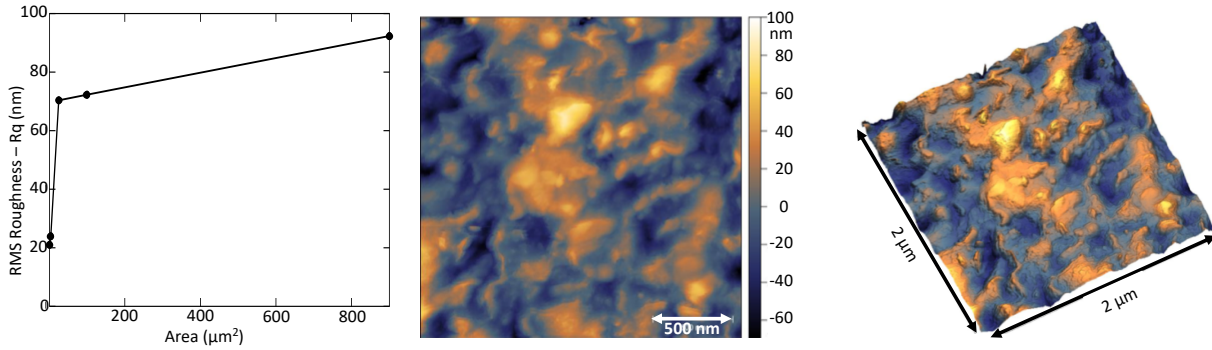
Figure 9.21: Milling appears to widen the TAF distribution, and it reduces high-energy TAFs before low-energy TAFs.

and measurements, which means that the ex-situ experiments cannot exactly mirror the ion-trapping experiments. As long as atmosphere exposure does not dramatically alter the atomic-scale surface roughness, we should still be able to gain valuable information from these types of experiments.

In our first attempt, a series of ex-situ experiments were done with an entirely different set of surface treatment and characterization tools than were used in the original ion trapping experiments. We have found that it is very difficult to directly compare and sync up those ex-situ results with the in-situ results presented in this manuscript. At Berkeley we have built a vacuum chamber with a milling, heating and substrate-mounting setup almost identical to the one in the ion-trapping chamber. This will be a valuable system moving forward.

After Trap C underwent a long series of surface treatments and measurement experiments, as presented in Section 7, we retired the trap and brought it to an AFM for further analysis. Evidence of hillocks found in these measurements was already presented in Figure 9.13. Additional measurements can be found in Figure 9.22, including and RMS roughness analysis and a topological map of the smoothest area of the trap surface.

Although it is interesting to see features at the 20 nm scale, all of these large features prevent us from measuring the atomic-scale features that we are most interested in. Some of the large features were likely brought on by heat treatments and ion milling, but we also know that the originally-fabricated surface was incredibly rough. In Figure 9.23, we present an SEM image of an ion trap at the intersection of the metal surface and one of the trenches. Before this image was taken, this trap was baked in vacuum at 430 K for a total of 9 weeks,



(a) RMS roughness versus area (b) $2 \mu\text{m} \times 2 \mu\text{m}$ measurement area, vertical amplitudes between -70 nm and +100 nm (c) 3D visualization of (e)

Figure 9.22: AFM measurements of Trap C, taken when the trap was removed from vacuum after surface treatment Electron 5.

and underwent no further surface treatment. Large, μm -scale features are visible.

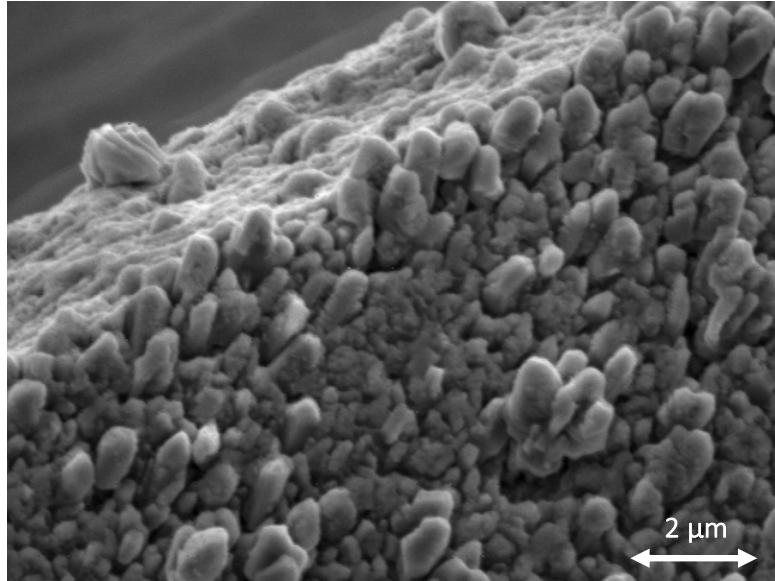


Figure 9.23: SEM of ion trap surface at edge of trench. Trap was baked for 9 weeks at 430 K under $5\text{e-}8$ Torr vacuum.

Our ion-trap fabrication process, as it is currently implemented, is not conducive to the formation of a smooth metal film. We evaporate at a 45° angle, which has been known to enhance shadowing effects and grow bumpy surfaces [23]. The background pressure in the evaporation chamber during our deposition process is around $5\text{e-}7$ Torr. Experiments by Chang et. al. showed that hillocks form during evaporation if the chamber pressure is

higher than 1e-7 Torr [24]. To get the best-possible measurements of atomic-scale surface roughness, we would have to alter our metal deposition process to produce a much smoother film.

In addition to continuing with ex-situ experiments, it might be fairly simple to integrate a morphology measurement into our in-situ experimental process. A laser-scattering measurement would allow us to measure changes in some of the larger features. We could measure heating rates on these exact surfaces, and determine whether or not heating rate transformations correspond to measurable changes in surface morphology. One thing to be wary of is that hillock growth would likely dominate these measurements, and atomic-scale surface roughness would not be visible. This could lead to a set of results that is irrelevant or even highly misleading.

9.6 Summary

(this section will be re-written later)

Observation: TAF distributions sometimes change shape and increase in magnitude when the trap is heated.

Observation: this transformation saturates with a half life of 1.5 days at 575 K.

Observation: this transformation only took place when the aluminum on the surface was elemental (not aluminum oxide or nitride)

Observation: ion milling can reset the thermal transformation

Rejected hypothesis: new contaminants are deposited during heat treatment

Rejected hypothesis: the chemical form of contaminants changes during heat treatment

Rejected hypothesis: noise goes up because hillocks grow during heat treatment

We found evidence to support one hypothesis:

Hypothesis: noise goes up when we heat because atomic-scale surface roughness decreases

Evidence: Annealing lowers atomic-scale surface roughness as thin film recrystallizes

Evidence: Milling increases atomic-scale surface roughness

Evidence: Recrystallization temperatures of aluminum is consistent with our film recrystallizing at 575 K

Evidence: Recrystallization temperatures of aluminum oxide and nitride are consistent with our film not recrystallizing at 575 K

We discuss a few other things, including:

Speculation: smoothing makes noise go up because sources on smooth surfaces become correlated

TAF distributions: have some interesting patterns in them

Ex-situ experiments: are difficult, but potentially useful moving forward

DRAFT

Chapter 10

Electron bombardment experiments

Over the course of this project we did five electron-treatment experiments, and each treatment affected ion heating rates in a different way. Sometimes heating rates went up, sometimes they went down, and sometimes they went up at some temperatures and down at others. To our knowledge, this is the first systematic study of electron bombardment as an ion-trap surface treatment.

In this chapter, we will first describe treatment parameters and measurement results from five electron bombardment experiments. This includes ion heating rate data, measured Auger spectra, and insights drawn from non-electron surface treatments.

Next, we review literature that explores interactions between energetic electrons and materials such as metals, oxides, and organic molecules. Considering our specific materials and electron-beam parameters, we determine that radiolysis is the dominant damage mechanism in our system.

We then discuss various dynamic processes that take place in solid-state systems and can be modeled as thermally activated fluctuations (TAFs). Adsorbate diffusion, contaminant desorption, and defect motion all have energy barriers in our measurement regime.

Using the TAF model as a link between ion heating rate measurements, electron damage in various materials, and atomic dynamics in solid state systems, we draw conclusions about the underlying physics taking place in each electron treatment experiment.

Finally, we propose future experiments to further investigate links between material dynamics and electric-field noise.

10.1 Overview of experimental results

We executed five electron-bombardment experiments in Trap C. This section will include details of treatment parameters, ion-heating-rate data taken before and after electron bombardment, and a description of the physical state of the substrate at the beginning of each treatment. This will serve to focus the investigation of electron-material interactions in Section 10.2. The in-depth discussion and interpretation of these results will be reserved for Section 10.3.

10.1.1 Treatment parameters

The electron-bombardment experiment procedure went as follows, with a slight variation in treatment Electron 1:

1. Measure ion heating rates as a function of trap substrate temperature
2. Generate a 2 keV electron beam by passing a current though a filament
3. Align the beam to the ion-heating-rate measurement region of the trap
4. Bombard the substrate with electrons while recording the Auger spectrum
5. Measure ion heating rates as a function of trap substrate temperature

In treatment Electron 1, the electron beam bombarded the ion-heating-rate measurement region of the trap for approximately six minutes, and was then redirected to a new location on the substrate for the duration of the three-hour Auger measurement.

Table 10.1: Electron bombardment surface treatment parameters

Treatment	Energy deposited (kJ/cm ²)	Duration (hr)	Current density (mA/cm ²)	Beam energy (keV)
Electron 1	2	0.1	2.8	2
Electron 2	76	3.0	3.5	2
Electron 3	176	3.2	7.6	2
Electron 4	281	3.2	12.2	2
Electron 5	2130	23.0	12.9	2

When the electron beam in the Auger spectrometer is turned on, the pressure in the vacuum chamber rises from 1e-10 Torr to 1e-8 Torr. In Figure 10.1 we present typical RGA spectra showing a rise in peaks at 2, 12, 15, 16, and 28 amu as the electron filament is beginning to heat up. This rise in pressure is likely caused by outgassing of the electron filament, in combination with electron induced desorption.

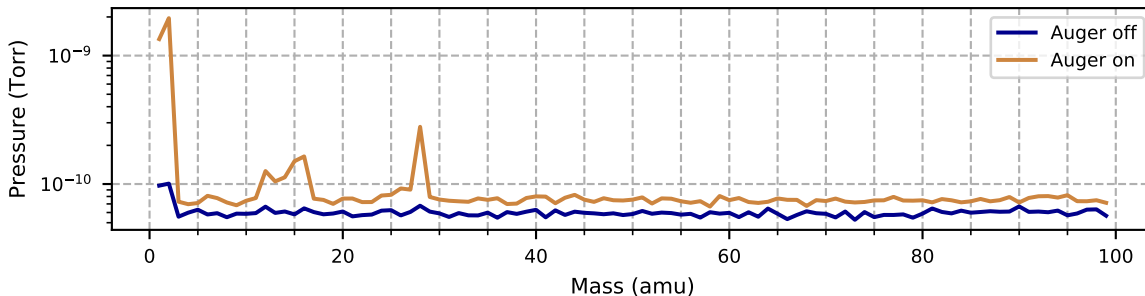


Figure 10.1: Turning on the electron beam in the Auger spectrometer releases compounds of mass 2, 12, 15, 16, and 28 amu.

10.1.2 Substrate properties

The five electron-bombardment experiments executed on Trap C were interspersed with other surface treatments. As a result, at the beginning of each electron treatment, the substrate had a unique set of physical properties. This section will describe the methods we used to determine those properties, which are summarized in Table ??.

Table 10.2: Surface properties of the substrate during electron treatments

Treatment	Carbon at surface	Aluminum at surface	Primary surface material type	Topology
Electron 1	Graphite	Oxide	Hydrocarbon adsorbates	Smooth
Electron 2	Carbide	Nitride & oxide	Insulator	Mixed
Electron 3	Carbide	Nitride & oxide	Insulator	Rough
Electron 4	Carbide	Elemental	Conductor	Smooth
Electron 5	Carbide	Elemental to Carbide	Conductor to insulator	Smooth

The chemical state of carbon at the surface is determined by comparing measured carbon Auger line-shapes to reference spectra, as shown in Figure 10.2. The Electron 1 Auger matches graphitic carbon, which is consistent with the presence of a thick layer of hydrocarbon contamination on the surface of the trap. Between treatments Electron 1 and Electron 2, the graphitic carbon was milled away from the surface, leaving behind a small amount of carbidic carbon. This is evidenced by the relative surface fractions in Figure 10.3, and by the Auger line-shapes in Figure 10.2.

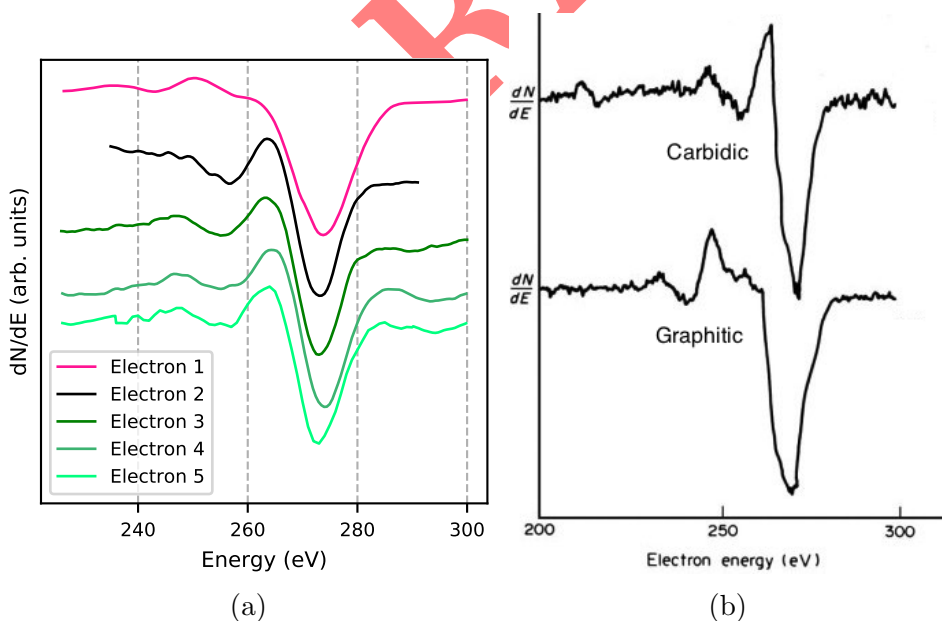


Figure 10.2: (a) Auger spectra of carbon measured during electron treatments (normalized)
(b) Reference spectra of graphitic and carbidic carbon [56]

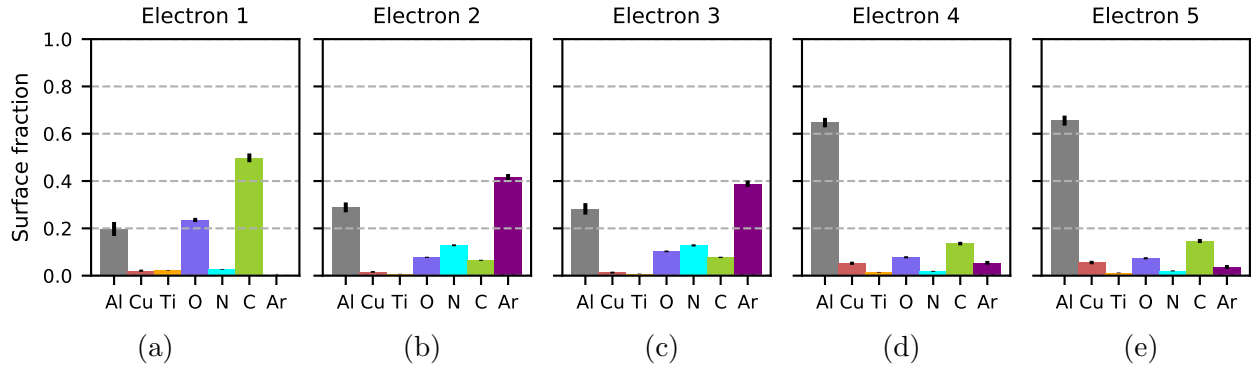


Figure 10.3: Elemental composition of the trap surface at the start of each electron treatment

The chemical state of aluminum is determined through consideration of the shape of the measured Auger spectra (Figure 10.4a-c), the shifts in the energy of the largest aluminum peak (Figure 10.4d), and the elemental compositions of the trap surface (Figure 10.3).

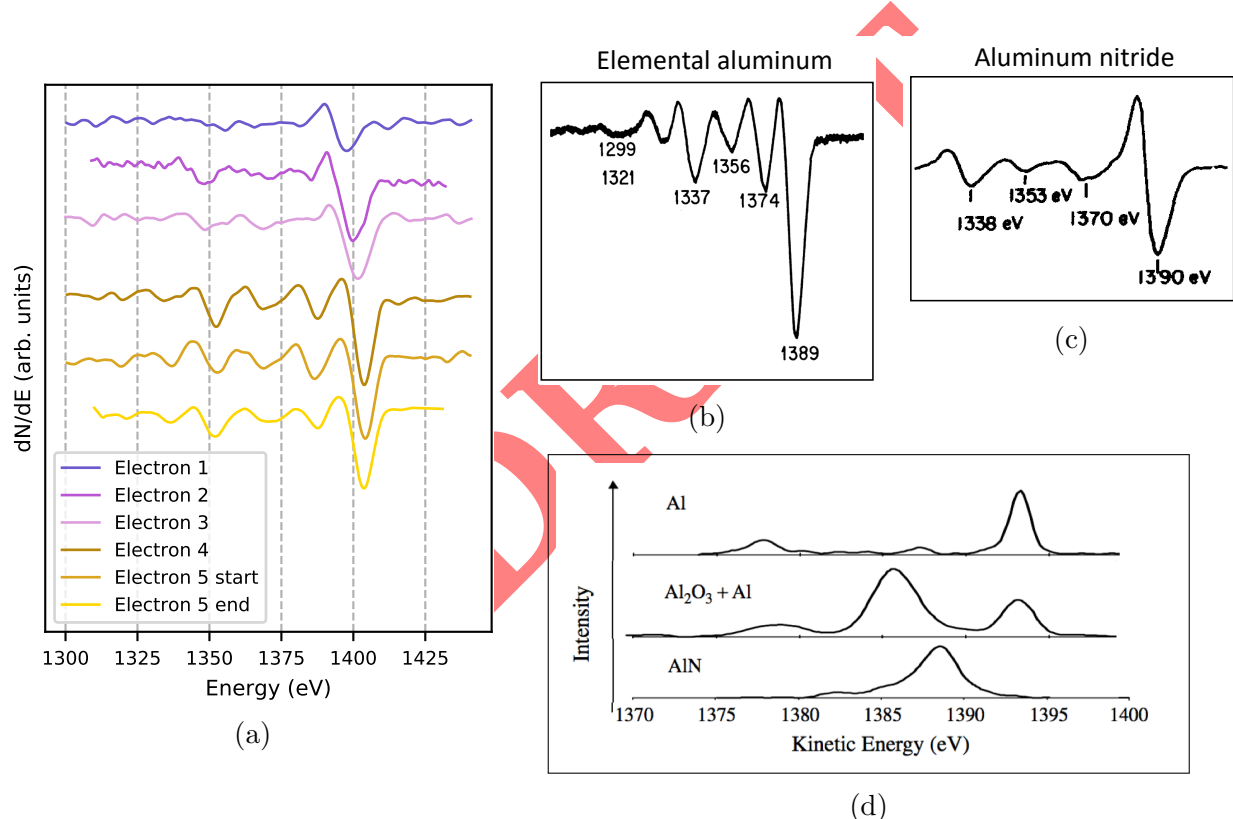


Figure 10.4: (a) Measured aluminum auger spectra (b) Reference spectrum of elemental aluminum [45] (c) Reference spectrum of aluminum nitride [46] (d) Reference showing relative peak positions of aluminum, aluminum oxide, and aluminum nitride [47]

chemical info: peak shifts due to charging by 15 eV [Pantano1980].

During treatment Electron 1, the aluminum peak was shifted down in energy and there was a large concentration of oxygen on the surface, indicating that the aluminum was oxi-

dized. During treatments Electron 2 and Electron 3, the aluminum line-shapes matched the reference spectrum of aluminum nitride (Figure 10.4a,c). There were significant fractions of both nitrogen and oxygen present on the trap, and no other metals for them to bind to (Figure 10.3b,c). It follows that during these treatments the aluminum was bound with both nitrogen and oxygen.

The aluminum spectra measured during treatments Electron 4 and Electron 5 match the elemental aluminum reference spectrum (Figure 10.4a,b). The presence of elemental aluminum is consistent with surface compositions presented in Figure 10.3d,e, as they indicate that the contaminant fractions were low at the start of both of these electron treatment experiments. However, during treatment Electron 5, the top monolayer of aluminum was transformed into aluminum carbide.

In Figure 10.5, we present surface fractions of aluminum, argon, carbon and oxygen as they evolve due to heat treatments and electron bombardment experiments. This data begins with the Auger spectrum measured immediately after the final argon milling treatment (Mill 12), and ends with the final measurement of treatment Electron 5. The oxygen fraction remains constant throughout all of these experiments, the argon fraction decreases during heat treatments, and the carbon fraction rises steadily as a function of electron bombardment time.

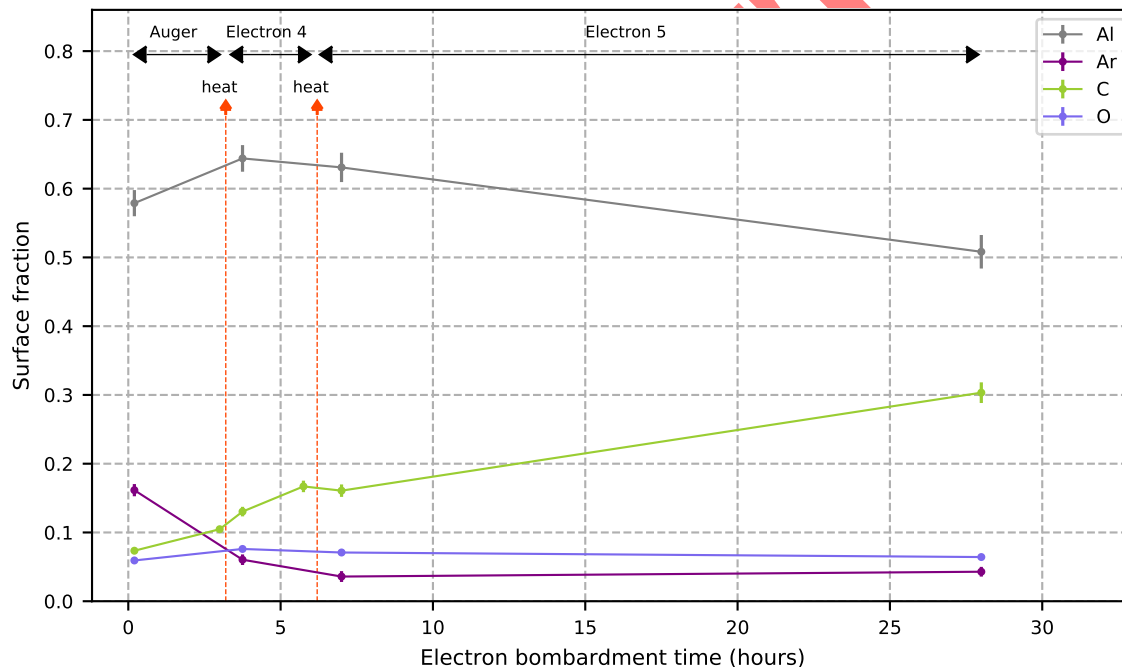


Figure 10.5: Surface fractions of the dominant materials on the trap surface, plotting as a function of electron bombardment time.

Auger electrons from aluminum and carbon are able to escape from depths of five and ten monolayers respectively [30]. From the beginning of Electron 4 to the end of Electron 5, the aluminum fraction dropped by 25%, and the carbon fraction rose from 0.1 to 0.3. From these numbers, we estimate that between one and two monolayers of carbon were deposited. As the carbon detected by the Auger was carbidic, the top surface of the aluminum must

have transformed into aluminum carbide.

It is not unusual for electron beams to deposit carbon onto metal surfaces. This phenomenon, commonly referred to as *electron beam induced deposition* (EBID), will be discussed in detail in Section 10.2.

In addition to determining the chemical state of the trap surface during each electron treatment, we also characterize its topology. In Chapter 9, we presented evidence that argon milling reduced ion heating rates in part by increasing atomic-scale surface roughness, and that heat treatments raised ion heating rates by smoothing out the surface. To determine the topological state of the surface during each electron treatment, we consider the effects of the heating and milling experiments that proceeded it. The context in which each electron treatment took place can be found in Chapter 7, and is simplified and summarized here in Figure 10.6.

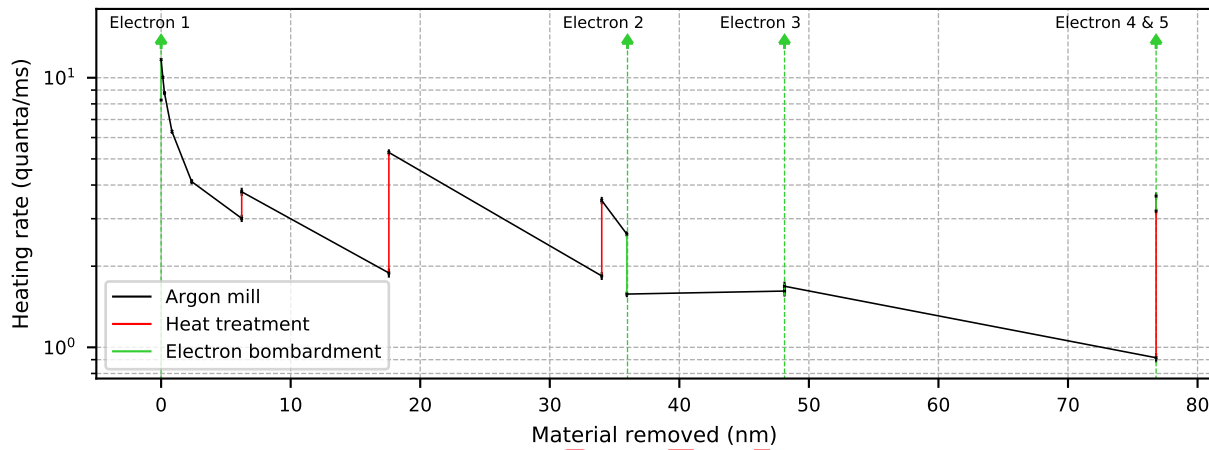


Figure 10.6: Heating rates measured at room temperature as the trap was treated

The strongly peaked TAF distribution measured before treatment Electron 1, and the fact that the trap had been extensively heated and never milled, indicate that the surface was smooth before Electron 1. The trap was milled before Electron 2, but the milling only partially removed the smoothing effects of the previous heat treatment. For this reason, we designate the topology at the start of Electron 2 as a mix between rough and smooth. Electron 3 took place after extensive milling, and a heat treatment that had no impact on ion heating rates, so the trap surface would have been rough. Electron 4 and 5 followed a heat treatment in which the ion heating rates rose by a factor of three, indicating that the trap had smoothed out.

10.1.3 Heating rate measurements

We have discussed the wide variety of conditions under which electron treatments took place. In Figure 10.7, we present heating rate measurements taken before and after these treatments.

In each case, the electron treatment had a different effect on the temperature scaling. In treatment Electron 1, room-temperature heating rates rose, and high-temperature heating rates fell. Treatment Electron 2 caused heating rates at all temperatures to fall by 40%.

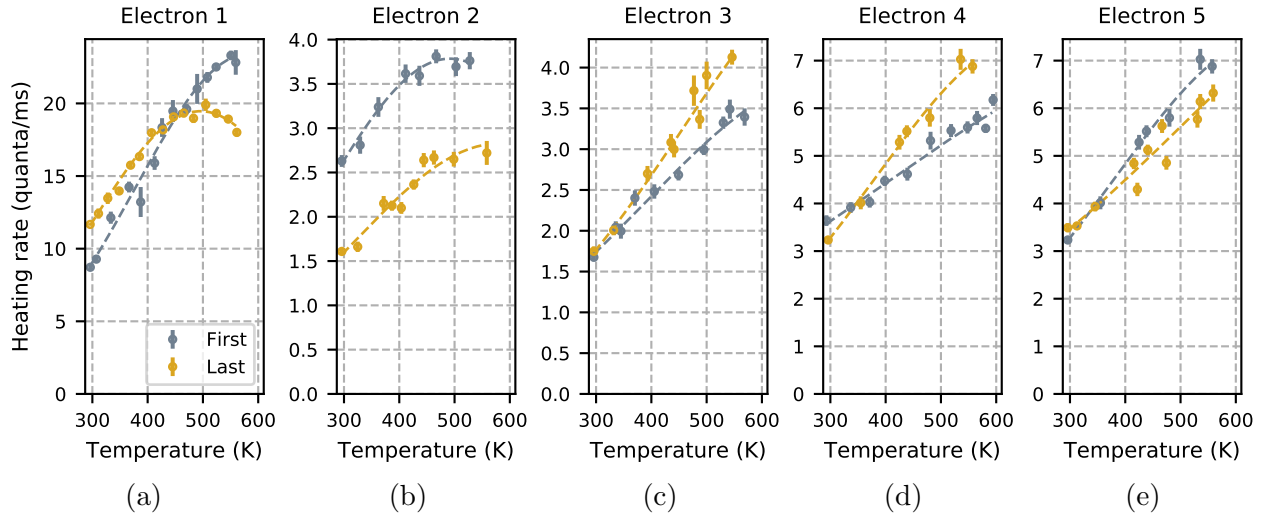


Figure 10.7: Temperature scalings measured before and after electron bombardment

The effects of Electron 3 and Electron 4 were similar, raising heating rates only at high temperatures, but Electron 5 had the opposite effect, lowering heating rates slightly at high temperatures.

Figure 10.8 combines data from Figures 10.7 and 10.5 to draw attention to the fact that as carbon built up on the surface of the substrate, the ion heating rate at room temperature did not change.

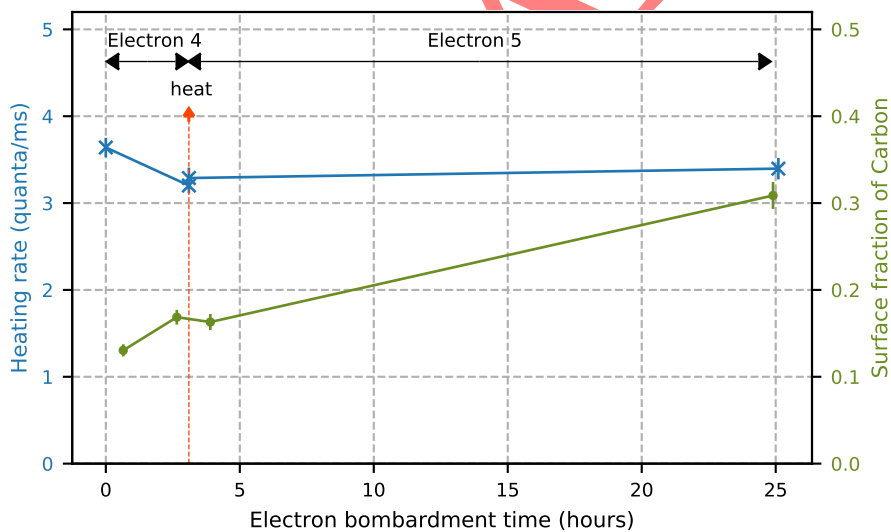


Figure 10.8: heating rate and carbon fraction v time

In this section, we have presented a richly diverse set of experiments and data. In order to use these results to develop insight into the nature of electric-field noise in ion traps, we must determine what types of physical changes took place in the substrate as it was repeatedly bombarded with electrons.

10.2 Materials interacting with energetic electrons

When a beam of energetic electrons bombards the surface of a material, three types of damage take place: knock-on damage, radiolysis damage, and damage by induced electric fields [57]. Knock-on damage is the direct transfer of momentum from an electron to an atom. This momentum knocks the atom out of its place in the lattice. In contrast, radiolysis damage is driven by electron-electron interactions. The incoming electrons excite and ionize atoms, breaking bonds and leaving behind volatile fragments that reform into new chemical structures. Unlike knock-on and radiolysis damage, which take place on the atomic scale, damage by induced electric fields (DIEF) can drive large-scale transformations. If the electron beam charges up the material at its point of impact, an electric-field gradient forms in the material. This gradient drives the collective motion of atoms towards or away from the electron beam.

Our ultimate goal is to determine how our electron beam drives changes in electric-field noise in our system. In order to do this, we must first narrow down which damage processes are taking place. We consider separately how an electron beam such as ours interacts with the three primary material types present in our substrate: conductors, insulators, and organic contaminants. We also discuss electron beam induced deposition, which is a consequence of energetic electrons interacting with gas molecules.

10.2.1 Conductors

A 2 keV electron beam cannot directly damage a conductive metal substrate.

Radiolysis damage takes place when electrons excite and ionize atoms, making them mobile and chemically volatile. In order for this to damage a material, the atoms must remain ionized for an extended period of time. Displacement takes place on a timescale of picoseconds. In a good conductor such as aluminum, ionization relaxation takes place on a femtosecond timescale. This does not leave enough time for displacement, so the material remains undamaged [57]. This also means that DIEF is not a problem in conductors. A damage-inducing electric-field gradient cannot form if ionized atoms relax on a picosecond timescale.

Knock-on damage does not require sustained ionization, but it only takes place if the electron energy exceeds a material-dependent threshold. This threshold can be calculated from the atomic displacement energy. Aluminum atoms have a displacement energy of 25 eV in the bulk [58], and about 5 eV at the surface [57]. From the surface displacement energy, and equations from reference [57], we calculate a knock-on threshold energy of 60 keV. As this is 58 keV greater than the energy of our electron beam, no knock-on damage of metals can take place in our system.

10.2.2 Insulators

In insulators such as aluminum oxide and aluminum nitride, the dominant effect of a 2 keV, 10 mA/cm² electron beam is radiolysis damage. Insulators have long ionization relaxation times. For example, aluminum oxide relaxes on the timescale of minutes [57]. This is many of orders of magnitude greater than the picoseconds required for radiolysis damage.

Both DIEF and the thermal effects of radiolysis have been known to bring on collective atomic transformations such as phase changes, phase decomposition, and nanocrystal precipitation. However, since we use an electron beam with a current density of 10 mA/cm^2 , we will not see any of these collective effects. In order to drive collective motion, the current density would need to be at least two orders of magnitude higher [57].

When radiolysis breaks bonds between atoms in the bulk of a material, new bonds quickly form, leaving little lasting damage. In contrast, bond-breaking at the surface of a material can lead to significant mass loss through electron stimulated desorption [59]. Electron stimulated desorption is distinctly different from electron sputtering. Electron sputtering refers to the removal of surface atoms through knock-on damage, and it can only be caused by high-energy electrons. In contrast, the typical threshold energies for electron stimulated mass loss are between 10 and 40 eV [60].

Electron stimulated mass loss takes place after the bonds between an atom and the substrate are broken by radiolysis. Most neutral atoms will re-bond, but many ionized atoms will be repelled from the substrate by the charged-up surface. Low-mass atoms such as hydrogen, oxygen and nitrogen are preferentially removed by this process [59]. This can lead to an increase in atomic-scale surface roughness, as well as changes in the chemical composition of the surface. Electron decomposition of metal oxides takes place on the timescale of a few hours in experiments like ours [60].

10.2.3 Organic contaminants

Hydrocarbon contaminants are ubiquitous in unmilled ion trap surfaces. These molecules are deposited during atmosphere exposure, during imperfect handling, and during baking as oils outgas from vacuum-chamber components. Hydrocarbon molecules are strongly affected by radiolysis damage. This damage can manifest in a system such as ours through processes such as bond cleavage, cross linking, and mass loss.

Electrons cleave bonds and break down hydrocarbons through dissociative electron attachment, dipolar dissociation, and dissociation ionization. In other words, a hydrocarbon can fragment when it absorbs an electron, when it absorbs energy from an electron, and when one of its electrons is knocked out by another electron. From the discussion of damage thresholds in reference [60], we estimate that a 2 keV, 10 mA/cm^2 electron beam will take about five minutes to do significant damage to a monolayer of adsorbates.

Hydrogen desorption is the primary hydrocarbon damage mechanism, as it leaves behind chemically reactive, unsaturated hydrocarbons. Electron bombardment can cause a set of distinctly independent structures on the surface of a substrate to form a single, tangled, cross-linked web [61]. Some unsaturated hydrocarbon fragments bond to the metal substrate directly and form carbidic surface layers. Others break off and desorb from the surface.

A hydrocarbon adsorbed to a metal surface has a hydrogen desorption resonance at 10 eV [62]. This is the energy at which electrons can most efficiently cleave carbon-hydrogen bonds. Electrons from our 2 keV beam are not in this energy regime. However, during an electron treatment, Auger electrons and inelastically scattered electrons with energies close to 10 eV can easily break apart carbon-hydrogen bonds throughout the substrate. In some cases, higher energy electrons may also affect hydrocarbon structures directly [63].

Hydrocarbon contaminants are generally thought to be at least partially, if not entirely,

responsible for electric-field noise in ion traps [1]. Given how easily our 2 keV, 10 mA/cm² electron beam can affect the chemical structure of organic contaminants in our substrate, it is very likely that this type of damage is one of the primary mechanisms driving changes in electric-field noise during our electron-bombardment experiments.

10.2.4 Electron beam induced deposition

In the absence of energetic electrons, an aluminum substrate stored in UHV will build up a small native oxide and a thin coating of saturated hydrocarbons. After about a monolayer of coverage, additional contamination will slow dramatically as there will be no unterminated bonding sites for new contaminants to attach to. In contrast, when energetic electrons are introduced to this system, a thick layer of carbon contamination can form through a process called electron beam induced deposition (EBID).

Hydrocarbons in the gas phase have a dissociative ionization cross-section peak at about 100 eV [64], and have significant interaction cross sections at higher energies as well. When a 2 keV electron beam passes through the background gas in a vacuum chamber, the gas molecules break apart into chemically reactive fragments. After passing through the gas and reaching the substrate, electrons activate bonding sites by breaking chemical bonds and removing hydrogen atoms. Ultimately, when the gas-state fragments hit the electron-activated substrate, they stick quickly and easily, and a thick contamination layer builds up. Layers of carbon formed through EBID are commonly found in electron microscopy experiments [63].

In our system, when the electron filament in the Auger spectrometer is turned on, the pressure in the chamber rises from 1E-10 to 1E-8 Torr. The electron beam deposits the newly-available gas molecules onto the surface of the ion trap. Evidence of deposition can be found in Auger spectra measured at different stages of treatments Electron 4 and Electron 5, as presented in Figure 10.5. During 28 hours of electron bombardment, EBID deposited between 1 and 2 monolayers of carbon onto the surface of the trap, as discussed in Section 10.1.2.

10.3 The underlying physics of five electron treatments

In the previous two sections, we presented the results of five electron bombardment experiments, determined the state of the substrate during each experiment, and discussed the different types of damage that take place when materials interact with energetic electrons. In this section we consider each treatment independently. We use all of the previously-gathered information to make a statement about how the physical properties of the substrate changed during each treatment.

We also reframe all temperature scaling measurements taken before and after electron treatments in the context of the TAF model. We compare the physical changes in the substrate to the measured TAF distribution changes. With these comparisons, we gain new insight into what the TAFs are made out of, and how they generate electric-field noise in ion traps.

To calculate the TAF distribution from a temperature scaling measurement, we must choose an appropriate attempt time τ_0 . In Chapter 6, we demonstrated how the choice of τ_0 affects the energy range of an extracted TAF distribution, and we discussed how different physical systems may have different attempt times. Our measurements indicate that both surface adsorbates and sub-surface contaminants may affect the electric-field noise in TRAP C. In this section, we will be directly comparing extracted TAF energies to energy barriers found in literature. Choosing a single value of τ_0 with which to analyze all of our data would introduce an unfounded restriction as to which physical processes could be relevant. For this reason, we plot all TAF distributions twice: once with an attempt time of 10^{-13} s, and once with an attempt time of 10^{-10} s.

10.3.1 Electron 1

Treatment Electron 1 was five minutes long. Before treatment, the trap was atomically smooth, the aluminum was oxidized, and the surface was coated with a thick layer of hydrocarbon adsorbates.

Physical changes in the substrate

The aluminum oxide was not damaged by this treatment. Damage to oxides takes place on a timescale of hours, and therefore would not have had time to develop.

Radiolysis damage to hydrocarbons takes place on a timescale of minutes. After five minutes of electron bombardment, the hydrocarbon layer would have been measurably altered, but not completely transformed. Electron stimulated desorption of hydrogen would have opened bonding sites on hydrocarbon molecules. Some molecules would have formed cross-links, some would have fragmented, and others would have been quickly re-terminated by hydrogen. Some molecular fragments would also have desorbed or bonded directly to the metal substrate.

Measured changes in the TAF distribution

As a result of this treatment, the TAF peak shifted down in energy by 0.1 eV, while maintaining roughly the same magnitude (Figure 10.9).

Insights into fluctuator physics

In this experiment, we observed a shift in the TAF distribution after we used electrons to alter the chemical structure of hydrocarbon adsorbates. This is evidence that hydrocarbon adsorbates generate electric-field noise. This also shows that the chemical form of the hydrocarbon affects the noise that it creates.

In Section 6.3 we discussed how a molecular adsorbate hopping between binding sites on a surface could generate electric-field noise via dipole moment fluctuations. A attempt time of $\tau_0 = 10^{-10}$ s is realistic for hydrocarbon diffusion on metals [39], so we consider the fluctuator distribution in Figure 10.9b. If electric field noise is generated when adsorbates move between binding sites, then the TAF activation energies would correspond to the migration barriers of the adsorbates. After reviewing literature on migration barriers of carbon adsorbates on

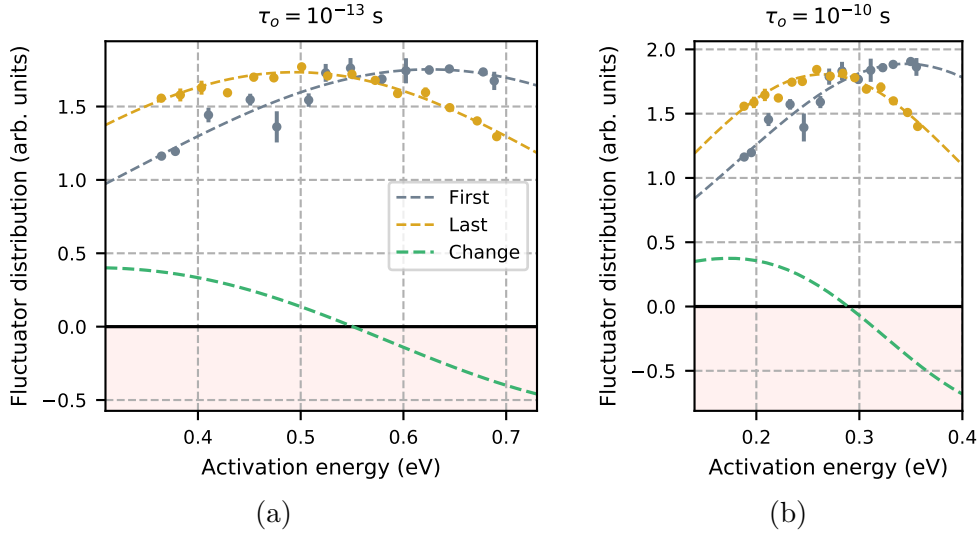


Figure 10.9: Changes in the TAF distribution as a result of treatment Electron 1

metal and aluminum oxide substrates, we find that TAF energy barriers we observe in Figure 10.9b could feasibly correspond to migration barriers in our system [38, 40].

In some comparisons of similarly-sized hydrocarbon compounds, the slightly larger structures were found to have higher migration barriers [38]. This may be related to the fact that each C-H group adds about 0.1 eV of Van der Waals attraction between the adsorbate and the metal [65]. With this information, the shift in TAF energies observed during Electron 1 can reasonably be explained by the loss of C-H groups from hydrocarbon compounds due to radiolysis damage. In short, hydrocarbon compounds break up, and diffusion barriers go down.

10.3.2 Electron 2

Treatment Electron 2 was three hours long. Before treatment, the trap was partially smooth. The surface was primarily composed of insulators aluminum nitride and aluminum oxide, and contained a small amount of carbidic carbon contamination. A large number of argon atoms were embedded near the surface.

Physical changes in the substrate

Three hours of electron bombardment can do measurable damage to aluminum oxide and aluminum nitride through electron stimulated desorption. Preferential desorption of oxygen and nitrogen increases atomic-scale surface roughness and alters the chemical composition of the surface. Auger spectra taken 1.5 hours apart during treatment Electron 2 revealed a 20% decrease in the oxygen fraction, and no change in the nitrogen fraction (Figure 10.10). This is evidence that preferential desorption of oxygen may have taken place.

Between treatments Electron 1 and Electron 2, the thick layer of hydrocarbon contamination on the surface of the trap was broken apart and removed by argon ion milling. However, some contaminants in the substrate were protected from argon damage. According to our

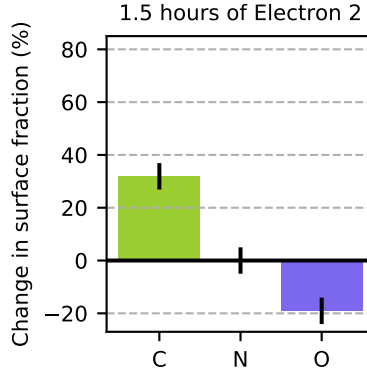


Figure 10.10: heating rate and carbon fraction v time

simulations, a 200 keV argon ion beam only penetrates 1.5 nm into the substrate. Organic contaminants present in caverns or defects throughout the bulk of the film, or bound to the surface behind large morphological features, would not have been affected by the argon beam. In contrast, 2 keV electrons can penetrate 100 nm into an aluminum substrate [66]. Electron 2 was the first large electron treatment, and could have broken apart a large number of organic compounds that had been left intact by previous treatments.

Electron beam induced deposition also took place, as evidenced by the rise in carbon shown in Figure 10.10. Three hours of electron bombardment would have deposited about a quarter of a monolayer of carbon onto the trap surface.

Measured changes in the TAF distribution

As a result of this treatment, the amplitude of TAFs decreased at all activation energies that we have access to (Figure 10.11). The decrease was most prominent at lower energies.

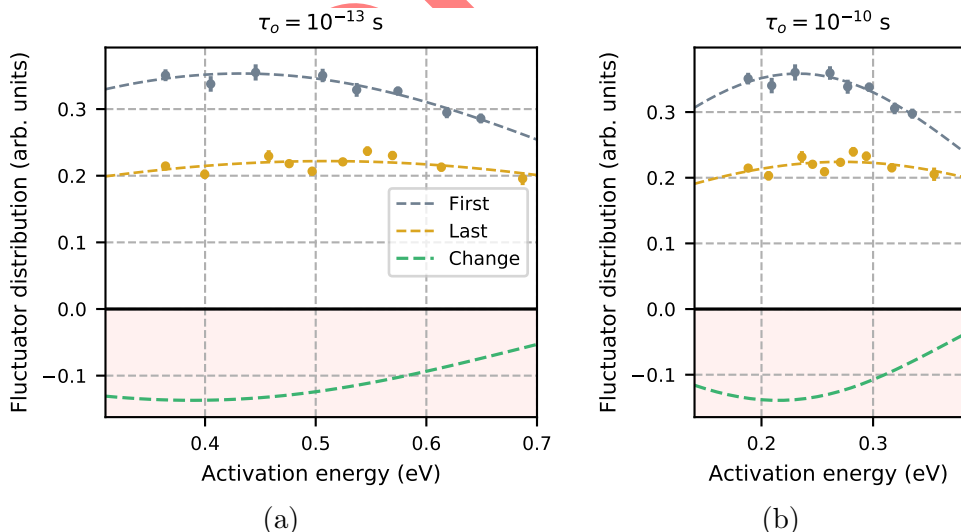


Figure 10.11: Changes in the TAF distribution as a result of treatment Electron 2

Insights into fluctuator physics

Treatment Electron 2 lowered the magnitude of the TAF distribution in large part by increasing the atomic-scale surface roughness of the substrate.

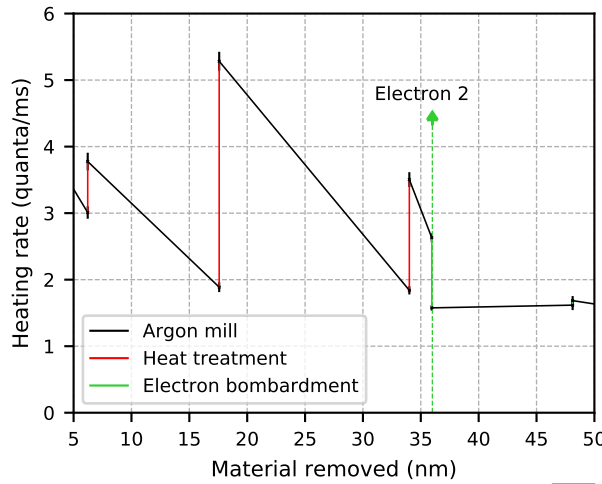


Figure 10.12: context

In Chapter 9, we established that ion heating rates are lower when the substrate is atomically rough. This was determined in large part by experiments in which annealing raised the ion heating rate by smoothing out the surface, and argon ion milling subsequently lowered rates back down by roughing the surface up. As shown in Figure 10.12, treatment Electron 2 took place after the effects of a heat treatment had only partially been undone by argon milling. After electron bombardment finished roughing up the surface, the subsequent argon milling had very little affect on the ion heating rate. If the electron treatment had not roughed up the surface, then the argon milling that followed it would have continued to remove the effects of annealing, thus lowering the heating rate by an additional quanta/ms.

From the data plotted in Figure 10.12, it is evident that treatment Electron 2 not only counteracted the effects of the previous heat treatment, but also brought the ion heating rates lower than they ever had been before. This could potentially be explained by the electron-induced breakdown of organic contaminants that had been shielded from argon milling damage.

Unlike in treatment Electron 1, there were no complex hydrocarbon adsorbates present on the trap surface after treatment Electron 2. With this in mind, we consider whether defect motion in the substrate could feasibly explain the electric-field fluctuations that we observe. Solid-state defects have an attempt time of $\tau_o = 10^{-13}$ s, so we consider the TAF distributions plotted in Figure 10.11a. Defects in polycrystalline aluminum and Al/Cu films have been observed to fluctuate with activation energies between 0.4 and 1 eV [36, 37, 35], which is reasonably consistent with the TAF distribution that we observe.

The effects of electron-induced carbon deposition will be explored in detail in the discussion of Electron 3, as there were fewer physical changes taking place during that treatment. In short, we find that EBID can raise the the amplitude of high-energy TAFs by a small amount. This may partially explain why treatment Electron 2 reduced the amplitude of low-energy TAFs more than high-energy TAFs.

10.3.3 Electron 3

Treatment Electron 3 was three hours long. Before treatment, the trap was atomically rough. The surface was primarily composed of insulators aluminum nitride and aluminum oxide, and contained a small amount of carbide carbon contamination. A large number of argon atoms were embedded near the surface.

Physical changes in the substrate

As described in the context of treatment Electron 2, aluminum nitride and aluminum oxide surfaces can be damaged by electron bombardment via electron induced desorption. Preferential desorption of oxygen and nitrogen can change the chemical composition of the surface, and increase atomic-scale surface roughness. As the surface was already atomically rough at the start of the Electron 3, changes to topology during this treatment would have been minimal.

Only 12 nm of material was milled off of the substrate between treatments Electron 2 and Electron 3, so Electron 3 would not have had much additional impact on any embedded or shielded organic compounds.

Three hours of electron bombardment would have again deposited about a quarter of a monolayer of carbon onto the surface of the trap.

Measured changes in the TAF distribution

As a result of this treatment, the amplitudes of TAFs with activation energies on the high end of our measurement range increased (Figure 10.13).

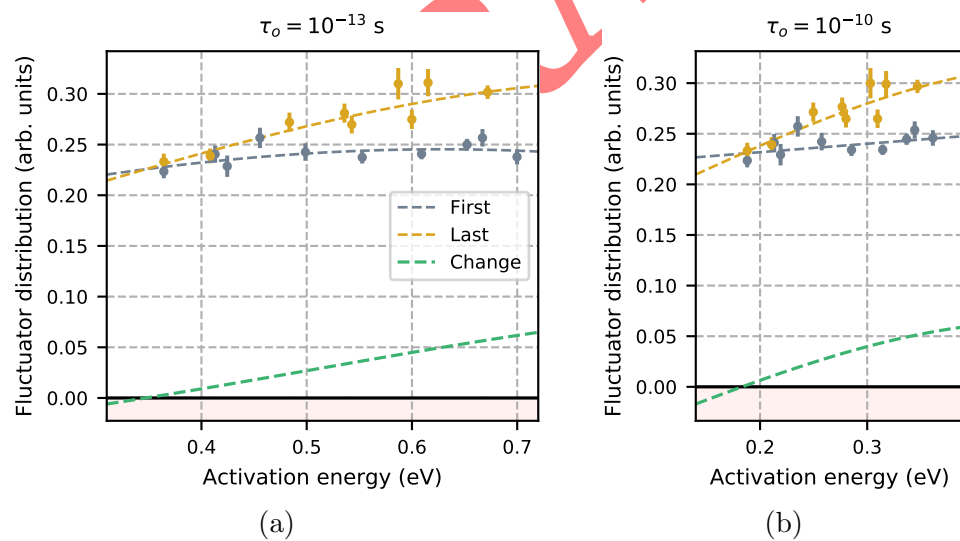


Figure 10.13: Changes in the TAF distribution as a result of treatment Electron 3

Insights into fluctuator physics

At the start treatment Electron 3, the effects of electron bombardment on shielded hydrocarbons and surface roughness had already been saturated. The only process that could have altered the TAF distribution at this time was the electron beam induced deposition of carbon on to the surface of the trap. EBID breaks up gas-state hydrocarbons in the vacuum chamber, depositing carbon adatoms onto the surface of the trap.

Carbon adatoms bond more strongly to metal substrates than complex hydrocarbon molecules do [38]. Single, double and triple bonds between carbon atoms and aluminum substrates have binding energies of 3, 3.3 and 3.8 eV respectively [41]. Migration barriers of adatom adsorbates are typically about 20% of the binding energy [38], which means that the activation energy of a carbon adatom on aluminum is between 0.6 and 0.8 eV. This is consistent with the TAF changes observed in Figure 10.13a.

As shown in Figure 10.13, we observe a small rise in high-energy TAFs after the electron beam deposits about a quarter of a monolayer of carbon onto the trap surface. This indicates that carbon adatoms can generate electric-field noise at 1 MHz, but only when the temperature of the substrate is elevated. At room temperature, carbon adatoms do not have a significant impact on ion heating rates.

10.3.4 Electron 4

Treatment Electron 4 was three hours long. Before treatment, the trap was atomically smooth. The surface was conductive, as it was primarily composed of elemental aluminum. A small amount of oxygen and carbidic carbon contamination was also present.

Physical changes in the substrate

The conductive metal could not have been damaged by the electron beam, so the smooth surface topology would have remained intact throughout this treatment. After three hours of electron bombardment, about a quarter of a monolayer of carbon was deposited on the surface, as evidenced by the rise in the carbon fraction shown in Figure 10.5.

Measured changes in the TAF distribution

As a result of this treatment, the amplitudes of TAFs with activation energies on the high end of our measurement range increased (Figure 10.13).

Insights into fluctuator physics

Like in treatment Electron 3, in treatment Electron 4 EBID was the only process that could have affected the TAF distribution. In both treatments, about a quarter of a monolayer of carbon was deposited, and in both treatments, the magnitude of high-energy TAFs increased.

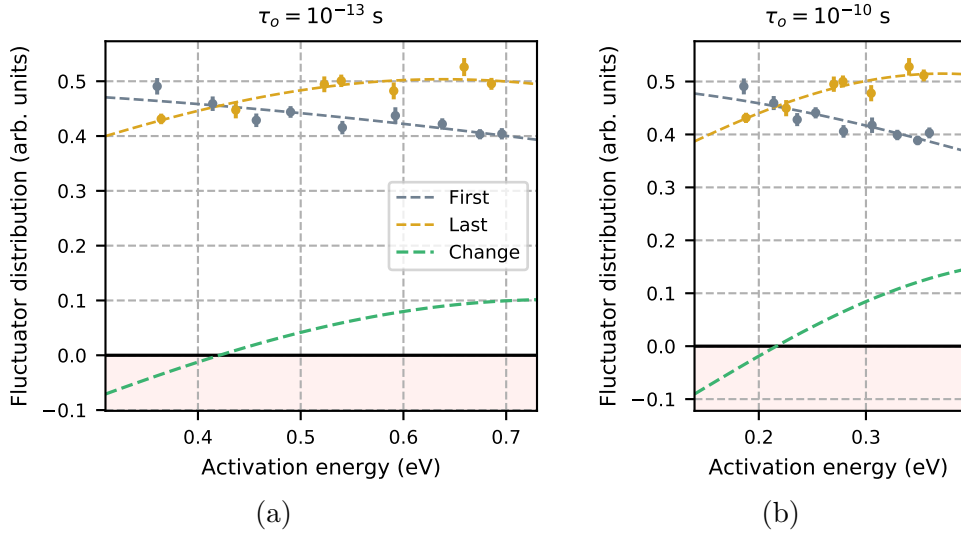


Figure 10.14: Changes in the TAF distribution as a result of treatment Electron 4

10.3.5 Electron 5

As a result of this treatment, treatment Electron 5 was twenty-three hours long. Before treatment, the trap was atomically smooth. The surface was conductive, as it was primarily composed of elemental aluminum. A small amount of oxygen and carbide carbon contamination was also present.

Physical changes in the substrate

The conductive metal could not have been damaged by the electron beam, so the smooth surface topology would have remained intact throughout this treatment. As shown in Figure 10.15, the surface fractions of nitrogen and oxygen did not change during this treatment, thus confirming that preferential electron-induced desorption did not take place.

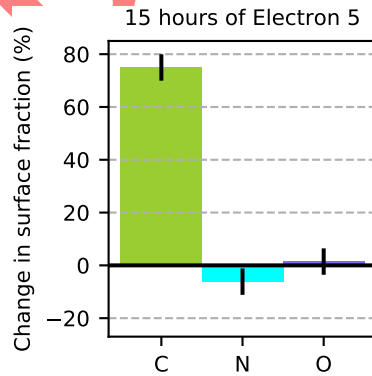


Figure 10.15: heating rate and carbon fraction v time

After twenty-three hours of electron bombardment, at least one and possibly two full monolayers of carbon were deposited onto the surface, as evidenced by the rise in the carbon fraction shown in Figure 10.5.

Measured changes in the TAF distribution

The amplitudes of TAFs with activation energies on the high end of our measurement range decreased by a small amount (Figure 10.13). There may also have been a small increase in low-energy TAFs.

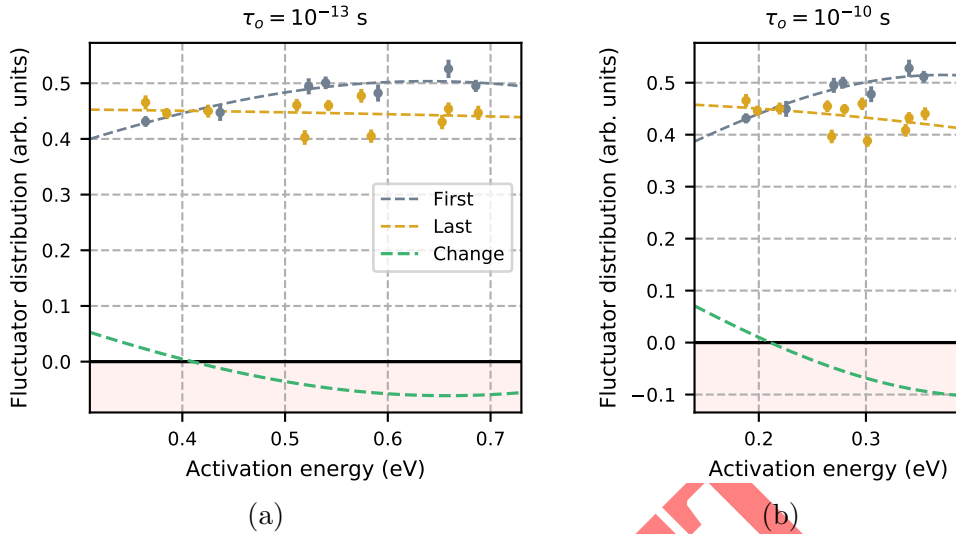


Figure 10.16: Changes in the TAF distribution as a result of treatment Electron 5

Insights into fluctuator physics

Like in treatments Electron 3 and 4, in treatment Electron 5 EBID was the only process that could have affected the TAF distribution. However, the effect on the TAF distribution was different this time. Instead of raising the magnitude of TAFs at high energies, this treatment lowered the magnitude of TAFs at high energies.

The key difference between these treatments may be the amount of carbon that was present on the trap surface during each treatment. Suppose that each carbon atom is a thermally-activated fluctuator. During the entirety of treatments Electron 3 and 4, less than a monolayer of carbon was present on the surface. As a result, each deposited carbon atom was able to move between aluminum bonding sites and generate electric-field noise.

In contrast, by the end of treatment Electron 5, well over a monolayer of carbon had been deposited. This means that the surface could no longer be described as an aluminum surface with carbon adatoms diffusing around. Instead, it had become an aluminum substrate with a solid layer of aluminum carbide. It is not unreasonable that carbon atoms incorporated into a full monolayer of aluminum carbide would follow different dynamics than individual carbon adatoms on an unsaturated aluminum surface.

10.4 Summary and plans for future work

(to be revised later)

After presenting data from five electron bombardment experiments, and reviewing all of the many ways in which an electron beam can damage a substrate such as ours, we made several bold statements about electric-field noise in ion traps:

- Molecular hydrocarbon adsorbates can make lots of electric-field noise. However, once they're gone, there is still a lot of noise left over.
- The electric-field noise from a hydrocarbon molecule depends on its chemical structure
- Electrons can reduce ion heating rates in traps with oxidized metal surfaces by increasing surface roughness
- Carbon surface adatoms are not relevant noise sources in ion traps, as they do not generate noise at 1 MHz at room temperature

It could be interesting to test the impact of chemistry on hydrocarbon noise by depositing hydrocarbons and hitting them with electrons. We could also test our understanding of electron bombardment by trying to repeat these results and make predictions. We would create smooth and rough surfaces, both oxidized and unoxidized, and predict how they would respond to electron treatments. Then we would run the experiments and see if we were right.

It's a good thing we don't have a quantum computer, or else we would just model our substrate in all its complex glory and miss out on all of these fun experiments.

DRAFT

Chapter 11

High-temperature shoot off

- there isn't a spike in pressure
- there isn't a current dependence
- it's too consistent for recrystallization
- it isn't TAF
- the temperature is wrong for a phase transition
- there is ion loss, but that happened at lower temperatures as well
- it did happen at another electrode
- when we tried to sit on it, it kind-of went away
- but the first few times we measured it, it was repeatable
- It seems to be changing over time/in response to surface treatments, shifting up in temperature and alpha

Chapter 12

Conclusion

DRAFT

Bibliography

- [1] M. Brownnutt et al. “Ion-trap measurements of electric-field noise near surfaces”. In: *Reviews of Modern Physics* 87.4 (Dec. 2015), pp. 1419–1482. ISSN: 0034-6861. DOI: [10.1103/RevModPhys.87.1419](https://doi.org/10.1103/RevModPhys.87.1419). arXiv: [1409.6572v1](https://arxiv.org/abs/1409.6572v1). URL: <http://link.aps.org/doi/10.1103/RevModPhys.87.1419>.
- [2] Colin D. Bruzewicz et al. “Trapped-ion quantum computing: Progress and challenges”. In: *Applied Physics Reviews* 6.2 (June 2019), p. 021314. ISSN: 19319401. DOI: [10.1063/1.5088164](https://doi.org/10.1063/1.5088164). arXiv: [1904.04178](https://arxiv.org/abs/1904.04178).
- [3] V. M. Schäfer et al. “Fast quantum logic gates with trapped-ion qubits”. In: *Nature* 555.7694 (Feb. 2018), pp. 75–78. ISSN: 14764687. DOI: [10.1038/nature25737](https://doi.org/10.1038/nature25737). arXiv: [1709.06952](https://arxiv.org/abs/1709.06952).
- [4] Crystal Noel et al. “Electric-field noise from thermally activated fluctuators in a surface ion trap”. In: *Physical Review A* 99.6 (June 2019), p. 063427. ISSN: 24699934. DOI: [10.1103/PhysRevA.99.063427](https://doi.org/10.1103/PhysRevA.99.063427). arXiv: [1809.05624](https://arxiv.org/abs/1809.05624). URL: <https://link.aps.org/doi/10.1103/PhysRevA.99.063427>.
- [5] D. An et al. “Distance scaling and polarization of electric-field noise in a surface ion trap”. In: *arxiv:1906:06489* (2019).
- [6] J. A. Sedlacek et al. “Distance scaling of electric-field noise in a surface-electrode ion trap”. In: *Physical Review A* 97 (2018), 020302(R). DOI: [10.1103/PhysRevA.97.020302](https://doi.org/10.1103/PhysRevA.97.020302). arXiv: [1712.00188](https://arxiv.org/abs/1712.00188).
- [7] C. D. Bruzewicz, J. M. Sage, and J. Chiaverini. “Measurement of ion motional heating rates over a range of trap frequencies and temperatures”. In: *Physical Review A - Atomic, Molecular, and Optical Physics* 91 (2015), p. 041402. ISSN: 10941622. DOI: [10.1103/PhysRevA.91.041402](https://doi.org/10.1103/PhysRevA.91.041402). arXiv: [1412.5119](https://arxiv.org/abs/1412.5119).
- [8] Jaroslaw Labaziewicz et al. “Temperature Dependence of Electric Field Noise Above Gold Surfaces”. In: *Physical Review Letters* 101 (2008), p. 180602. URL: <http://journals.aps.org/prl/abstract/10.1103/PhysRevLett.101.180602>.
- [9] J. Chiaverini and J. M. Sage. “Insensitivity of the rate of ion motional heating to trap-electrode material over a large temperature range”. In: *Physical Review A* 89.1 (Jan. 2014), p. 012318. ISSN: 1050-2947. DOI: [10.1103/PhysRevA.89.012318](https://doi.org/10.1103/PhysRevA.89.012318). arXiv: [1310.4385](https://arxiv.org/abs/1310.4385). URL: <http://link.aps.org/doi/10.1103/PhysRevA.89.012318>.
- [10] D. T.C. Allcock et al. “Reduction of heating rate in a microfabricated ion trap by pulsed-laser cleaning”. In: *New Journal of Physics* 13 (2011). ISSN: 13672630. DOI: [10.1088/1367-2630/13/12/123023](https://doi.org/10.1088/1367-2630/13/12/123023). arXiv: [1110.1486](https://arxiv.org/abs/1110.1486). URL: <http://www.njp.org/>.

- [11] N. Daniilidis et al. “Surface noise analysis using a single-ion sensor”. In: *Physical Review B* 89.24 (June 2014), p. 245435. ISSN: 1098-0121. DOI: [10.1103/PhysRevB.89.245435](https://doi.org/10.1103/PhysRevB.89.245435). URL: <http://link.aps.org/doi/10.1103/PhysRevB.89.245435>.
- [12] D. A. Hite et al. “100-Fold Reduction of Electric-Field Noise in an Ion Trap Cleaned with In Situ Argon-Ion-Beam Bombardment”. In: *Physical Review Letters* 109.10 (Sept. 2012), p. 103001. DOI: [10.1103/PhysRevLett.109.103001](https://doi.org/10.1103/PhysRevLett.109.103001). arXiv: [arXiv:1112.5419v1](https://arxiv.org/abs/1112.5419v1). URL: <http://link.aps.org/doi/10.1103/PhysRevLett.109.103001>.
- [13] Robert McConnell et al. “Reduction of trapped-ion anomalous heating by in situ surface plasma cleaning”. In: *Physical Review A - Atomic, Molecular, and Optical Physics* 92.2 (Aug. 2015), p. 020302. ISSN: 10941622. DOI: [10.1103/PhysRevA.92.020302](https://doi.org/10.1103/PhysRevA.92.020302). arXiv: [1505.03844](https://arxiv.org/abs/1505.03844).
- [14] J A Sedlacek et al. “Evidence for multiple mechanisms underlying surface electric-field noise in ion traps”. In: *Physical Review A* 98 (2018), p. 63430. ISSN: 24699934. DOI: [10.1103/PhysRevA.98.063430](https://doi.org/10.1103/PhysRevA.98.063430). arXiv: [1809.07761](https://arxiv.org/abs/1809.07761). URL: <https://journals.aps.org/prb/pdf/10.1103/PhysRevA.98.063430>.
- [15] Keith G Ray et al. “Van Der Waals-corrected density functional study of electric field noise heating in ion traps caused by electrode surface adsorbates”. In: *New Journal of Physics* 21.5 (May 2019), p. 053043. ISSN: 13672630. DOI: [10.1088/1367-2630/ab1875](https://doi.org/10.1088/1367-2630/ab1875). arXiv: [1810.10199](https://arxiv.org/abs/1810.10199). URL: <https://iopscience.iop.org/article/10.1088/1367-2630/ab1875>.
- [16] E. Kim et al. “Electric-field noise from carbon-adatom diffusion on a Au(110) surface: First-principles calculations and experiments”. In: *Physical Review A* 95 (2017), p. 033407. ISSN: 24699934. DOI: [10.1103/PhysRevA.95.033407](https://doi.org/10.1103/PhysRevA.95.033407). arXiv: [1610.01079](https://arxiv.org/abs/1610.01079).
- [17] Muir Kumph et al. “Electric-field noise above a thin dielectric layer on metal electrodes”. In: *New Journal of Physics* 18.2 (Feb. 2016). ISSN: 13672630. DOI: [10.1088/1367-2630/18/2/023020](https://doi.org/10.1088/1367-2630/18/2/023020). arXiv: [1511.00624](https://arxiv.org/abs/1511.00624).
- [18] Gebhard Littich. *Electrostatic Control and Transport of Ions on a Planar Trap for Quantum Information Processing*. Masters thesis. ETH Zürich and University of California, Berkeley, 2011.
- [19] Raymond E. March. “An Introduction to Quadrupole Ion Trap Mass Spectrometry”. In: *Journal of Mass Spectrometry* 32.4 (Apr. 1997), pp. 351–369. ISSN: 1096-9888. DOI: [10.1002/\(SICI\)1096-9888\(199704\)32:4<351::AID-JMS512>3.0.CO;2-Y](https://doi.org/10.1002/(SICI)1096-9888(199704)32:4<351::AID-JMS512>3.0.CO;2-Y).
- [20] Wolfgang Paul. “Electromagnetic traps for charged and neutral particles”. In: *Reviews of Modern Physics* 62.3 (July 1990), pp. 531–540. ISSN: 0034-6861. DOI: [10.1103/RevModPhys.62.531](https://doi.org/10.1103/RevModPhys.62.531). URL: <http://link.aps.org/doi/10.1103/RevModPhys.62.531>.
- [21] J. Chiaverini et al. “Surface-electrode architecture for ion-trap quantum information processing”. In: *Quantum Information and Computation* 5 (2005), pp. 419–439. URL: <http://dl.acm.org/citation.cfm?id=2011670.2011671>.

- [22] Yves Bellouard et al. “Fabrication of high-aspect ratio, micro-fluidic channels and tunnels using femtosecond laser pulses and chemical etching”. In: *Optics Express* 12.10 (May 2004), p. 2120. ISSN: 1094-4087. DOI: [10.1364/opex.12.002120](https://doi.org/10.1364/opex.12.002120).
- [23] Angel Barranco et al. *Perspectives on oblique angle deposition of thin films: From fundamentals to devices*. Mar. 2016. DOI: [10.1016/j.pmatsci.2015.06.003](https://doi.org/10.1016/j.pmatsci.2015.06.003).
- [24] C. Y. Chang and R. W. Vook. “The effect of surface aluminum oxide films on thermally induced hillock formation”. In: *Thin Solid Films* 228.1-2 (May 1993), pp. 205–209. ISSN: 00406090. DOI: [10.1016/0040-6090\(93\)90599-K](https://doi.org/10.1016/0040-6090(93)90599-K).
- [25] Christian Felix Roos. “Controlling the quantum state of trapped ions”. Doctoral thesis. University of Innsbruck, 2000.
- [26] Crystal Noel. “High temperature studies of electric-field noise in a surface ion trap”. PhD thesis. University of California, Berkeley, 2019. URL: http://www.physics.berkeley.edu/research/haeffner/publications/Noel%7B%5C_%7Dthesis.pdf.
- [27] D. Gorman. “Noise sensing and quantum simulation with trapped atomic ions”. PhD Thesis. University of California, Berkeley, 2018. URL: http://research.physics.berkeley.edu/haeffner/publications/dylan%7B%5C_%7Dgorman%7B%5C_%7Dthesis.pdf.
- [28] Thaned Pruttivarasin. “Spectroscopy , fundamental symmetry tests and quantum simulation with trapped ions”. PhD thesis. University of California, Berkeley, 2014, p. 141.
- [29] Michael Ramm. “Quantum Correlations and Energy Transport in Trapped Ions”. PhD thesis. University of California, Berkeley, 2014.
- [30] John C. Vickerman and Ian S. Gilmore. *Surface Analysis - The Principal Techniques: Second Edition*. John Wiley and Sons, Mar. 2009, pp. 1–666. ISBN: 9780470017630. DOI: [10.1002/9780470721582](https://doi.org/10.1002/9780470721582).
- [31] P. T. Dawson and K. K. Tzatzov. “Quantitative auger electron analysis of titanium nitrides”. In: *Surface Science* 149.1 (Jan. 1985), pp. 105–118. ISSN: 00396028. DOI: [10.1016/S0039-6028\(85\)80016-9](https://doi.org/10.1016/S0039-6028(85)80016-9).
- [32] L. I. Vergara, M. C.G. Passeggi, and J. Ferrón. “Chemical changes induced on a TiO₂ surface by electron bombardment”. In: *Thin Solid Films* 515.23 (Sept. 2007), pp. 8365–8370. ISSN: 00406090. DOI: [10.1016/j.tsf.2007.04.031](https://doi.org/10.1016/j.tsf.2007.04.031).
- [33] James F. Ziegler, M. D. Ziegler, and J. P. Biersack. “SRIM - The stopping and range of ions in matter (2010)”. In: *Nuclear Instruments and Methods in Physics Research, Section B: Beam Interactions with Materials and Atoms* 268.11-12 (June 2010), pp. 1818–1823. ISSN: 0168583X. DOI: [10.1016/j.nimb.2010.02.091](https://doi.org/10.1016/j.nimb.2010.02.091).
- [34] P. Dutta, P. Dimon, and P. M. Horn. “Energy Scales for Noise Processes in Metals”. In: *Physical Review Letters* 43.9 (Aug. 1979), pp. 646–649. ISSN: 00319007. DOI: [10.1103/PhysRevLett.43.646](https://doi.org/10.1103/PhysRevLett.43.646). arXiv: [arXiv:1011.1669v3](https://arxiv.org/abs/1011.1669v3). URL: <https://link.aps.org/doi/10.1103/PhysRevLett.43.646>.
- [35] P. Dutta and P. M. Horn. “Low-frequency fluctuations in solids: 1/f noise”. In: *Reviews of Modern Physics* 53 (1981), pp. 497–516. DOI: [10.1103/RevModPhys.53.497](https://doi.org/10.1103/RevModPhys.53.497).

- [36] J. Briggmann et al. “Irradiation-induced defects in thin aluminium films studied by 1/f noise”. In: *physica status solidi (a)* 146 (1994), p. 325. ISSN: 1521396X. DOI: [10.1002/pssa.2211460128](https://doi.org/10.1002/pssa.2211460128).
- [37] R. H. Koch, J. R. Lloyd, and J. Cronin. “1/f noise and grain-boundary diffusion in aluminum and aluminum alloys”. In: *Physical Review Letters* 55 (1985), p. 2487. ISSN: 00319007. DOI: [10.1103/PhysRevLett.55.2487](https://doi.org/10.1103/PhysRevLett.55.2487).
- [38] J. V. Barth. *Transport of adsorbates at metal surfaces: From thermal migration to hot precursors*. Tech. rep. 3. 2000, pp. 75–149. DOI: [10.1016/S0167-5729\(00\)00002-9](https://doi.org/10.1016/S0167-5729(00)00002-9). URL: <http://ipent.ep>.
- [39] Jens Weckesser, Johannes V Barth, and Klaus Kern. “Direct observation of surface diffusion of large organic molecules at metal surfaces: PVBA on Pd(110)”. In: *Journal of Chemical Physics* 110.11 (1999), pp. 5351–5354. ISSN: 00219606. DOI: [10.1063/1.478430](https://doi.org/10.1063/1.478430). URL: <https://doi.org/10.1063/1.478430>.
- [40] J C Ornelas-Lizcano and R A Guirado-López. “Adsorption of carbon monoxide on small aluminum oxide clusters: Role of the local atomic environment and charge state on the oxidation of the CO molecule”. In: *Journal of Chemical Physics* 142.12 (2015), p. 124311. ISSN: 00219606. DOI: [10.1063/1.4916320](https://doi.org/10.1063/1.4916320). URL: <https://doi.org/10.1063/1.4916320>.
- [41] Douglas J. Fox et al. “The prototype aluminum-carbon single, double, and triple bonds: Al-CH₃, Al=CH₂, and Al—CH”. In: *The Journal of Chemical Physics* 73.7 (1980), pp. 3246–3254. ISSN: 00219606. DOI: [10.1063/1.440519](https://doi.org/10.1063/1.440519).
- [42] Alexandre G. Brolo, Donald E. Irish, and Brian D. Smith. “Applications of surface enhanced Raman scattering to the study of metal-adsorbate interactions”. In: *Journal of Molecular Structure* 405.1 (Mar. 1997), pp. 29–44. ISSN: 00222860. DOI: [10.1016/S0022-2860\(96\)09426-4](https://doi.org/10.1016/S0022-2860(96)09426-4).
- [43] Kuan Yu Lin, Guang Hao Low, and Isaac L. Chuang. “Effects of electrode surface roughness on motional heating of trapped ions”. In: *Physical Review A* 94.1 (July 2016), p. 013418. ISSN: 24699934. DOI: [10.1103/PhysRevA.94.013418](https://doi.org/10.1103/PhysRevA.94.013418). arXiv: [1605.02808](https://arxiv.org/abs/1605.02808).
- [44] D. An et al. “Surface trap with dc-tunable ion-electrode distance”. In: *Review of Scientific Instruments* 89.9 (Sept. 2018), p. 093102. DOI: [10.1063/1.5046527](https://doi.org/10.1063/1.5046527). arXiv: [1807.06043](https://arxiv.org/abs/1807.06043). URL: <http://aip.scitation.org/doi/10.1063/1.5046527>.
- [45] G. E. McGuire. *Auger Electron Spectroscopy Reference Manual*. Springer US, 1979. DOI: [10.1007/978-1-4757-1702-0](https://doi.org/10.1007/978-1-4757-1702-0).
- [46] J. A. Kovacich et al. “Auger electron and x-ray photoelectron spectroscopy of sputter deposited aluminum nitride”. In: *Journal of Applied Physics* 55.8 (Apr. 1984), pp. 2935–2939. ISSN: 00218979. DOI: [10.1063/1.333335](https://doi.org/10.1063/1.333335). URL: <http://aip.scitation.org/doi/10.1063/1.333335>.
- [47] B. Timmermans et al. “Chemical effects in Auger electron spectra of aluminium”. In: *Surface and Interface Analysis* 34.1 (Aug. 2002), pp. 356–359. ISSN: 0142-2421. DOI: [10.1002/sia.1316](https://doi.org/10.1002/sia.1316). URL: <http://doi.wiley.com/10.1002/sia.1316>.

- [48] M. E. Drits, E. S. Kadaner, and L. S. Toropova. “Recrystallization of aluminum and aluminum alloy foils”. In: *Metal Science and Heat Treatment* 13.5 (May 1971), pp. 399–401. ISSN: 15738973. DOI: [10.1007/BF00652447](https://doi.org/10.1007/BF00652447).
- [49] Carl V Thompson. *Grain growth in thin films*. Tech. rep. 1990, pp. 245–68. URL: www.annualreviews.org.
- [50] J Jurusik and L Zdanowicz. “Electron microscope investigations of the growth morphology of cadmium arsenide films vacuum deposited at various substrate temperatures”. In: *Thin Solid Films* 67.2 (1980), pp. 285–292. ISSN: 00406090. DOI: [10.1016/0040-6090\(80\)90461-7](https://doi.org/10.1016/0040-6090(80)90461-7).
- [51] Hailang Qin, Peter Sutter, and Guangwen Zhou. “The Crystallization of Amorphous Aluminum Oxide Thin Films Grown on NiAl(100)”. In: *Journal of the American Ceramic Society* 97.9 (Sept. 2014). Ed. by N. Jacobson, pp. 2762–2769. ISSN: 00027820. DOI: [10.1111/jace.13036](https://doi.wiley.com/10.1111/jace.13036). URL: <http://doi.wiley.com/10.1111/jace.13036>.
- [52] Shien Ri and Masumi Saka. “Diffusion-fatigue interaction effect on hillock formation in aluminum thin films under thermal cycle testing”. In: *Materials Letters* 79 (July 2012), pp. 139–141. ISSN: 0167577X. DOI: [10.1016/j.matlet.2012.03.109](https://doi.org/10.1016/j.matlet.2012.03.109).
- [53] Yasunori Yamamura and Hiro Tawara. “Energy dependence of ion-induced sputtering yields from monatomic solids at normal incidence”. In: *Atomic Data and Nuclear Data Tables* 62.2 (Mar. 1996), pp. 149–253. ISSN: 0092640X. DOI: [10.1006/adnd.1996.0005](https://doi.org/10.1006/adnd.1996.0005).
- [54] V Timoshevskii et al. “The influence of surface roughness on electrical conductance of thin Cu films: An ab initio study”. In: (2008). DOI: [10.1063/1.2937188](https://doi.org/10.1063/1.2937188). URL: <http://jap.aip.org/jap/copyright.jsp>.
- [55] J Labaziewicz et al. “Suppression of Heating Rates in Cryogenic Surface-Electrode Ion Traps”. In: *Physical Review Letters* 100 (2008), p. 013001. DOI: [10.1103/PhysRevLett.100.013001](https://doi.org/10.1103/PhysRevLett.100.013001). URL: <http://journals.aps.org/prl/abstract/10.1103/PhysRevLett.100.013001>.
- [56] H L Marcus. *Auger Electron Spectroscopy*. Jan. 2001. DOI: [10.1016/B0-08-043152-6/00078-4](https://doi.org/10.1016/B0-08-043152-6/00078-4).
- [57] Nan Jiang. *Electron beam damage in oxides: A review*. Dec. 2015. DOI: [10.1088/0034-4885/79/1/016501](https://doi.org/10.1088/0034-4885/79/1/016501).
- [58] Gary S. Was. *Fundamentals of radiation materials science: Metals and alloys, second edition*. Berlin, Heidelberg, 2016. Chap. 2, pp. 1–1002. ISBN: 9781493934386. DOI: [10.1007/978-1-4939-3438-6](https://doi.org/10.1007/978-1-4939-3438-6).
- [59] R. F. Egerton, P. Li, and M. Malac. “Radiation damage in the TEM and SEM”. In: *Micron*. Vol. 35. 6. Aug. 2004, pp. 399–409. DOI: [10.1016/j.micron.2004.02.003](https://doi.org/10.1016/j.micron.2004.02.003).
- [60] C. G. Pantano and Theodore E. Madey. “Electron beam damage in Auger electron spectroscopy”. In: *Applications of Surface Science* 7.1-2 (Jan. 1981), pp. 115–141. ISSN: 03785963. DOI: [10.1016/0378-5963\(81\)90065-9](https://doi.org/10.1016/0378-5963(81)90065-9).

- [61] M Zharnikov et al. “Modification of alkanethiolate monolayers on Au-substrate by low energy electron irradiation: Alkyl chains and the S/Au interface”. In: *Physical Chemistry Chemical Physics* 1.13 (1999), pp. 3163–3171. ISSN: 14639076. DOI: [10.1039/a902013f](https://doi.org/10.1039/a902013f).
- [62] P Rowntree, L Parenteau, and L Sanche. *Anion Yields Produced by Low-Energy Electron Impact on Condensed Hydrocarbon Films*. Tech. rep. 1991, pp. 4902–4909. URL: <https://pubs.acs.org/sharingguidelines>.
- [63] W. F. Van Dorp and C. W. Hagen. “A critical literature review of focused electron beam induced deposition”. In: *Journal of Applied Physics* 104.8 (2008), pp. 081301–081301–42. ISSN: 00218979. DOI: [10.1063/1.2977587](https://doi.org/10.1063/1.2977587).
- [64] Cechan Tian and C R Vidal. “Cross sections of the electron impact dissociative ionization of CO, and”. In: *Journal of Physics B: Atomic, Molecular and Optical Physics* 31.4 (1998), p. 895. ISSN: 0953-4075. DOI: [10.1088/0953-4075/31/4/031](https://doi.org/10.1088/0953-4075/31/4/031).
- [65] B A Sexton and A E Hughes. *A comparison of weak molecular adsorption of organic molecules on clean copper and platinum surfaces*. Tech. rep. 1984, p. 227.
- [66] Gregory Wilson and J R Dennison. “Approximation of range in materials as a function of incident electron energy”. In: *IEEE Transactions on Plasma Science*. Vol. 40. 2 PART 1. 2012, pp. 291–297. DOI: [10.1109/TPS.2011.2176515](https://doi.org/10.1109/TPS.2011.2176515). URL: <http://ieeexplore.ieee.org..>